Novel Quantum Phase Transitions in Low-Dimensional Systems

A dissertation presented

by

Junhyun Lee

to

The Department of Physics

in partial fulfillment of the requirements

for the degree of

Doctor of Philosophy

in the subject of

Physics

Harvard University

Cambridge, Massachusetts

April 2016

Dissertation advisor   Author

Subir Sachdev   **Junhyun Lee**

Novel Quantum Phase Transitions in Low-Dimensional Systems

Abstract

We study a number of quantum phase transitions, which are exotic in their nature and separates non-trivial phases of matter. Since quantum fluctuations, which drive these phase transitions, are stronger in low-dimensions, we concentrate on low-dimensional systems. We consider two different two-dimensional systems in this thesis and study their phase transition.

First, we investigate a phase transition in graphene, one of the most famous two-dimensional systems in condensed matter. For a suspended bilayer graphene in $\nu = 0$ quantum Hall regime, the conductivity data and mean-field analysis suggests a phase transition from an antiferromagnetic (AF) state to a valence bond solid (VBS) state, when perpendicular electric field is increased. This AF to VBS phase transition is reminiscent of deconfined criticality, which is a novel phase transition that cannot be explained by Landau's theory of symmetry breaking. We show that in the strong coupling regime of bilayer graphene, the AF state is destabilized by the transverse electric field, likely resulting in a VBS state. We also consider monolayer and bilayer graphene in the large cyclotron gap limit and show that the effective action for the AF and VBS order parameters have a topological Wess-Zumino-Witten term, supporting that the phase transition observed in experiments is in the deconfined criticality class.

Second, we study the model systems of cuprate superconductor, which is effectively a two-dimensionalal system in the CuO_2 plane. The proposal that the pseudogap metal is a fractionalized Fermi liquid described by a quantum dimer model is extended using the density matrix renormalization group. Measuring the Friedel oscillations in the open boundaries reveals that the fermionic dimers have dispersion minima near $(\pi/2, \pi/2)$, which is compatible with the Fermi arcs in photoemission.

Abstract

Moreover, investigating the entanglement entropy suggests that the dimer model with low fermion density is similar to the free fermion system above the Lifshitz transition. We also study the phase transition from a metal with SU(2) spin symmetry to an AF metal. By applying the functional renormalization group to the two-band spin-fermion model, we establish the existence of a strongly coupled fixed point and calculate critical exponents of the fixed point.

Contents

Citations to Previously Published Work

Chapter 2 has been previously published as

"Deconfined criticality in bilayer graphene", Junhyun Lee and Subir Sachdev, Phys. Rev. B, **90**, 195427 (2014), `arXiv:1407.2936`.

Chapter 3 has been previously published as

"Wess-Zumino-Witten Terms in Graphene Landau Levels", Junhyun Lee and Subir Sachdev, Phys. Rev. Lett., **114**, 226801 (2015), `arXiv:1411.5684`.

Chapter 4 will be published shortly as

"Electronic quasiparticles in the quantum dimer model: density matrix renormalization group results", Junhyun Lee, Subir Sachdev, and Steven R. White, *in preparation.*

Chapter 5 has been previously published as

"Quantum criticality of reconstructing Fermi surfaces in antiferromagnetic metals", Junhyun Lee, Philipp Strack, and Subir Sachdev, Phys. Rev. B, **87**, 045104 (2013), `arXiv:1209.4644`.

Electronic preprints (shown in `typewriter font`) are available on the Internet at the following URL:

`http://arXiv.org`

Acknowledgments

It is a great honor for me to have had the help of so many people throughout my years at Harvard, and I would like to express my greatest gratitude for them. This thesis would not have been possible without their help.

First and foremost, I would like to thank my advisor, Professor Subir Sachdev. He was a caring and patient advisor, and his scientific knowledge and insight always have guided me to the right direction. I was greatly influenced by his perspective and style of physics, and it was only with his help that I was able to develop my current understandings in physics. I will always be indebted to him.

I also would like to thank my committee members, Professor Eugene Demler and Professor Jenny Hoffman. I greatly appreciate all of their advice and suggestions that they have given me, as well as many helpful courses taught by Professor Demler.

I also cannot forget to thank my fellow students in Sachdev group: Eun Gook Moon, Yejin Huh, Debanjan Chowdhury, Shubhayu Chatterjee, Wenbo Fu, Alex Thomson, Seth Whitsitt, Aavishkar Patel, and Julia Steinberg. I have greatly benefited not only from the invaluable discussions with them, but also from the sincere friendship that they have shared with me. My special thanks goes to Eun Gook and Yejin for motivating me to join this group during my first year of graduate school. Moreover, they were my friends with whom I could discuss physics in Korean, the language that I can discuss in with the least loss of information.

I have learned a lot from the many great postdocs in the condensed matter group at Harvard. Erez Berg, Liza Huijse, Matthias Punk, Philipp Strack, Brian Swingle, Janet Hung, Arijeet Pal, Andrea Allais, Andreas Eberlein, Will Witczak-Krempa, Fabian Grusdt, and Chong Wang were all talented physicists and good friends of mine. Their presence and advice were especially significant and impactful during my junior years, when there were no senior graduate students in the group. I have collaborated with Philipp on my first project, which became Chapter 5 of this thesis. It was an enjoyable and educational collaboration – and I will never forget his distinct laughter. I would also like to mention Miles Stoudenmire, who taught me the density matrix renormalization group at the Perimeter Institute. Without his help, Chapter 4 of this thesis would not have been possible.

I would like to take this opportunity to thank some of my wonderful friends that I made at Cambridge. Gilad Ben-Shach, Kartiek Agarwal, Yang He, Ying-Hsuan Lin, and Shu-Heng Shao were my great friends in the Harvard physics department. I would like to especially thank Ying for being such a wonderful roommate during the five years on Cowperthwaite. Having many Korean physics friends from Harvard and MIT – Eunmi Chae, SeungYeon Kang, Jaehoon Lee, Jee Woo Park, Changmin Lee, Soonwon Choi, Joonhee Choi, Sungjoon Hong, Jinseop Kim, and Jeongwan Haah – was a true blessing, as we shared similar backgrounds and concerns. I also appreciate my non-physics friends – Yelee An, Jeong-Mo Choi, Hyerim Hwang, In-ho Jo, Hanung Kim, Soojin Kim, Woo Min Kim, Dongwoo Lee, Yong Suk Moon, and Hyungsuk Tak – for their friendship and support as well.

I also would like to thank my friends who are not in the Boston area: Yongsoo Yang, Jay Hyun Jo, Chungyoon Lee, Hyunho Lee, Chulwon Kang, and Hyunjung Kim. Their friendship, despite the long physical distance, was always a true and firm support for me.

I would like to thank the people at Grace Vision Church, who always cared for me with God's love. I would like to especially thank Chanmi Seo for her enormous emotional and spiritual support.

Finally, I would like to give my most sincere and deepest thanks to my family: my parents Yong-Kee Lee and Hyungyoon Kim, my brother Jehyun Lee, my grandparents Sung Rho Lee and Tae Dong Jeong, and my late grandparents Eun Soo Kim and Hae Ja Jeon. Their love, encouragement, and support made possible for me to overcome all the challenging and difficult moments throughout my graduate years. This thesis is dedicated to them.

To my family

Chapter 1

Introduction

A major subject of condensed matter physics is different phases of matter and their universal properties. In many cases, we observe that two or more phases are connected by a critical point as we tune the parameters of the theory or experiment. The critical point between ground states at zero temperature, a quantum critical point, separates phases that are qualitatively distinct. Quantum fluctuations play a crucial role in these quantum phase transitions, in contrast to the classical phase transitions in finite-temperature which is mostly driven by thermal fluctuations. Understanding the nature of phase transition across this quantum critical point is essential to understanding the phases in the vicinity, and even the phases in the finite temperature region above the quantum critical point, the so-called "quantum-critical-fan" (Sachdev, 2011). The main theme of this thesis lies in the study of quantum phase transitions present in various systems in nature.

The study of phase transition has a long history and is a widely studied subject. Here, we focus on very specific subsets of phase transitions. In the first half of this thesis, we investigate the subject of "deconfined criticality" (Senthil et al., 2004a,b). Conventional second order phase transition (or continuous phase transition) is explained by the Landau-Ginzburg-Wilson paradigm of symmetry breaking (Wilson and Kogut, 1974; Landau et al., 1980). Deconfined criticality, in contrast, is a novel class of quantum phase transition, which is not described by this paradigm.

It exhibits a second order phase transition while the symmetry of one phase is not a subgroup of the other phase's symmetry, and has gapless excitation right at the critical point. We explain more on deconfined criticality later in this chapter.

In the latter half of this thesis, we consider the phase transition between a SU(2) symmetric Fermi liquid and an antiferromagnetic metal. This consists of two different processes: one is the breaking of the SU(2) spin symmetry, and the other is the Fermi surface reconstruction from a large Fermi surface of area $1 + p$ (p being the doping) to small Fermi pockets with area p. Scenarios where these two processes occur simultaneously and separately are both possible. First, we consider the case where the Fermi surface reconstructs while the SU(2) spin symmetry is retained. The intermediate state is the unconventional "fractionalized Fermi liquid" (Senthil et al., 2003) and possesses fractionalized excitations. We also investigate the direct phase transition from Fermi liquid to antiferromagnetic metal in detail. This is a more conventional scheme as the Fermi surface reconstruction immediately occurs as a result of the spin symmetry breaking.

In the context of the actual system of interest, we consider low-dimensional systems throughout this thesis – systems in two-dimension to be precise. The dimensionality of our system is relevant, since the quantum fluctuation in general gets stronger in lower dimensions. This means that the mean-field theory results, which is exact in the infinite dimension limit, becomes more and more inaccurate as we lower the dimension of our system of interest. Deviation from the expected classical behavior is beneficial to those who seek novel phases of matter. On the other hand, one-dimension is very special (Giamarchi, 2004). Interactions in one-dimension plays a quite different role, making the system to have a more collective nature. New physics such as that of Luttinger liquids dominates, which is very distinct from, for example, the physics of Fermi liquids. Therefore, loosely speaking, two-dimension is as far as we can get with large quantum fluctuations, without encountering the unique domain of one-dimensional systems. The two two-dimensional systems we are about to investigate are graphene (Chapters 2, 3) and cuprate superconductors (Chapters 4, 5). In the lattice point of view, graphene is a single layer of honeycomb lattice with carbon

atoms on each site. Cuprates are complex layered materials, but the common layer in all cuprates that is responsible for the interesting electronic structure is the CuO_2 plane, a square lattice with copper atoms on each lattice and oxygen atoms on each bond.

We will now briefly review some preliminary facts which are not included in the main text. The order of the materials follows the order of its appearance in the remainder of the thesis.

1.1 Electronic properties of graphene

The isolation of graphene, a single sheet of graphite, had a huge impact in the condensed matter and material science community (Novoselov et al., 2004). It demonstrated that a single layer of carbon can exist by itself in free space, which was believed not to be true at the time, in a rather (formally) simple method – peeling graphite with adhesive tape. Graphene has become a very popular material in part for its extraordinary mechanical and optical properties, but here we will concentrate on the unique electronic properties which also make graphene interesting (Geim and Novoselov, 2007; Castro Neto et al., 2009; Kotov et al., 2012).

The distinct electronic properties of graphene in the many-body physics context originate from its dispersion. In contrast to the quadratic dispersion near the minima of common electronic bands, electrons in undoped graphene have linear, Dirac-like dispersion near the Fermi energy. The Fermi energy lies exactly at the Dirac point, which is protected by sublattice symmetry, making undoped graphene a semimetal. Moreover, the linear dispersion leads to vanishing density of states near the Dirac points. This prevents the mechanism of screening of the long-ranged Coulomb interaction, making the system qualitatively different from Coulomb-screened Fermi liquids.

Adding another layer of honeycomb lattice of carbons to graphene, i.e., making it a *bilayer* graphene, changes the dispersion of electrons somewhat drastically. The semimetal behavior persists in bilayer graphene; however the dispersions at the Fermi
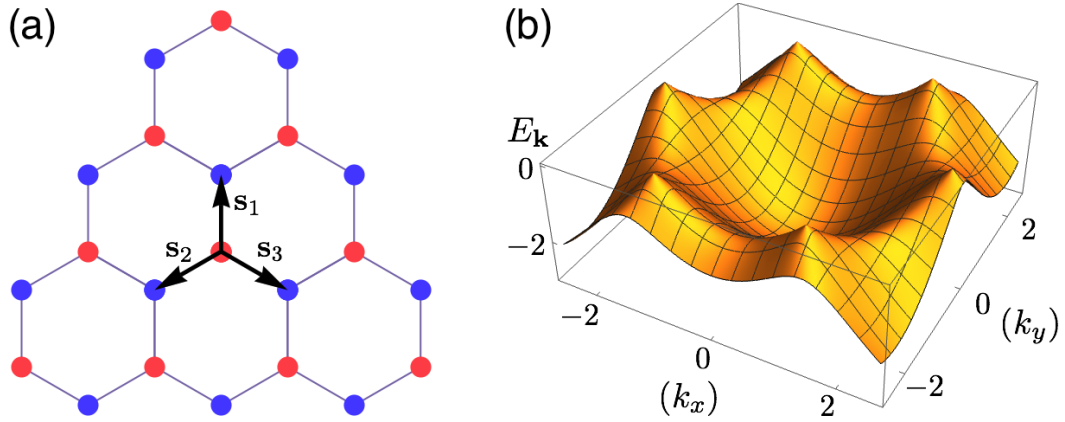
Figure 1.1: (a) The honeycomb lattice depicting monolayer graphene. The red and blue dots correspond to different sublattices. (b) The dispersion of monolayer graphene, showing only the low energy band. High energy band will be the inversion to the $E_{\mathbf{k}} = 0$ plane. At half-filling (undoped graphene) the low energy band is completely filled and high energy band is completely empty. Note the Dirac points are at $\mathbf{K}_{\pm} = \pm(\frac{4\pi}{3\sqrt{3}},\ 0)$.

points meet quadratically, and not linearly. The quadratic dispersion also leads to a somewhat enhanced screening compared to monolayer graphene. Detailed derivation of the dispersion of monolayer and bilayer graphene will follow.

The structure of graphene is a single layer honeycomb lattice of carbon atoms (Fig. 1.1(a)). Each bond of this honeycomb lattice is a σ bond, which is a covalent bond between the sp^2 hybridized orbitals of carbons. The remaining p orbital is perpendicular to the plane of graphene, and this serves as the itinerant electron of the system. This p orbital half-fills the π band, and therefore we consider one particle per site in undoped graphene.

These facts are well represented in the following tight-binding model.

$$H = -t \sum_{\mathbf{r} \in \Lambda_A} \sum_{i=1}^{3} a_{\mathbf{r}}^{\dagger}\, b_{\mathbf{r}+\mathbf{s}_i} + \text{h.c.} \tag{1.1}$$

Here, Λ_A and Λ_B are the sublattices of the honeycomb lattice, and $\mathbf{s}_i$'s are the vectors connecting nearest neighbors from Λ_A. In our coordinate system (Fig. 1.1(a)), we

define $\mathbf{s}_1 = (0,1)$, $\mathbf{s}_2 = (\frac{\sqrt{3}}{2}, -\frac{1}{2})$, and $\mathbf{s}_3 = (-\frac{\sqrt{3}}{2}, -\frac{1}{2})$ (We set the nearest neighbor spacing as 1). $a_{\mathbf{r}}^\dagger$ ($a_{\mathbf{r}}$) and $b_{\mathbf{r}}^\dagger$ ($b_{\mathbf{r}}$) are the fermion creation (annihilation) operators acting on Λ_A and Λ_B, respectively.

The energy spectrum of this Hamiltonian is shown in Fig. 1.1(b). It consist of two distinct Dirac points, $\mathbf{K}_\pm = \pm(\frac{4\pi}{3\sqrt{3}},\ 0)$, and the dispersion is linear at the Dirac points. We can linearize the spectrum around the Dirac points, $\mathbf{k} = \mathbf{K}_\pm + \mathbf{p}$, and this gives the expected linear dispersion of low-energy electrons.

$$\epsilon_{\mathbf{p}} = \pm |\mathbf{p}| \tag{1.2}$$

Now we turn to the dispersion of bilayer graphene. Distinguished by the stacking structure, bilayer graphene exists in *AA*- and *AB*-stacked form. In this thesis, we concentrate on the more common *AB*-stacked (or Bernal-stacked) form, where only half of the carbon atoms are on top of each other. The tight-binding Hamiltonian for the *AB*-stacked bilayer graphene is,

$$H = -t \sum_{\mathbf{r}\in\Lambda_A} \sum_{i=1}^{3} a_{\mathbf{r}}^\dagger\, b_{\mathbf{r}+\mathbf{s}_i} - t \sum_{\mathbf{r}\in\Lambda_C} \sum_{i=1}^{3} c_{\mathbf{r}}^\dagger\, d_{\mathbf{r}+\mathbf{s}_i} - t_\perp \sum_{\mathbf{r}\in\Lambda_A} a_{\mathbf{r}}^\dagger d_{\mathbf{r}} + \text{h.c.}. \tag{1.3}$$

Λ_C and Λ_D are the two sublattices in the additional layer, and $c^\dagger(c)$, $d^\dagger(d)$ are the fermion creation (annihilation) operators acting on the sublattices. $t_\perp$ is the tight binding hopping parameter between the layers which we assume is real. Note that Λ_A and Λ_D are the same in the plane of graphene.

After the same procedure as in the monolayer graphene, we obtain the low-energy dispersion near the $\mathbf{K}_\pm$ points. The new dispersion has four bands and now is quadratic instead of being linear in the monolayer case.

$$\begin{aligned}
\epsilon_{\mathbf{p}} &= \frac{1}{2}(\pm t_\perp \pm \sqrt{4|\mathbf{p}|^2 + t_\perp^2}) \\
&= \begin{cases} \pm \frac{|\mathbf{p}|^2}{t_\perp^2} + \mathcal{O}(\mathbf{p}^3) \\ \pm \left(t_\perp + \frac{|\mathbf{p}|^2}{t_\perp^2} \right) + \mathcal{O}(\mathbf{p}^3) \end{cases}
\end{aligned} \tag{1.4}$$

Note that in the first line of the above equation, two $\pm$'s can have all four combinations. There are two quadratic touching bands and two high-energy bands with a gap of order $\sim t_\perp$.
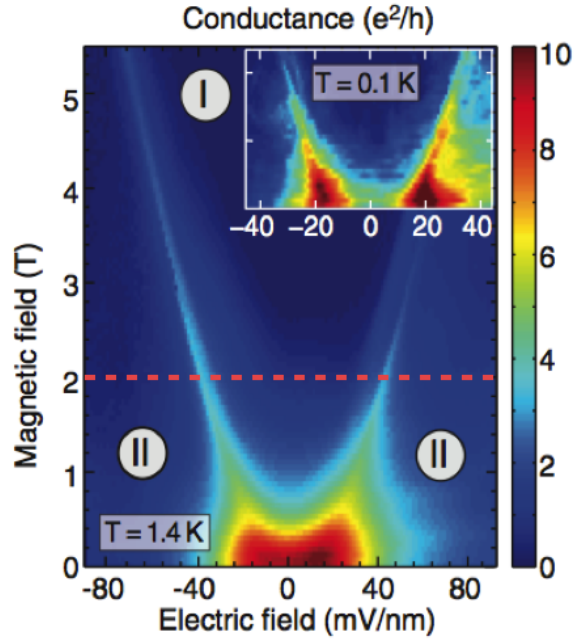
Figure 1.2: (Weitz et al., 2010) Conductivity data for suspended AB stacked bilayer graphene. Magnetic and electric fields are both perpendicular to the plane of graphene. The dashed line is added to the original figure and indicates our domain of interest.

One interesting result of the dispersions calculated above is the anomalous integer quantum Hall effect seen in monolayer and bilayer graphene. Graphene systems in the quantum Hall regime and the symmetry breaking of the SU(4) spin-valley symmetry has been extensively investigated (Zhang et al., 2005; Novoselov et al., 2006; Nomura and MacDonald, 2006; Bolotin et al., 2009; Weitz et al., 2010; Feldman et al., 2012). The experimental result which will be the key motivation for Chapters 2 and 3 is also from graphene in quantum Hall regime. Fig. 1.2 is the conductivity measurement data in suspended bilayer graphene with both perpendicular magnetic and electric fields (Weitz et al., 2010). One can see along the constant B-field line (depicted in red dashed line), there exists an insulator-to-insulator phase transition. This phase transition will be of the main focus of Chapters 2 and 3.

Finally, it is worth mentioning that graphene physics started a new field of two-

dimensional materials. Boron nitride, a cousin of graphene with the same honeycomb lattice but with boron and nitrogen in the two sublattices, has been extensively studied after the advent of graphene, as well as transition-metal dichalcogenide monolayers, which are single layer semiconductors. Moreover, the field is evolving into the research of so-called "Van der Waals heterostructures," which provides a very rich arena of stacked two-dimensional materials (Geim and Grigorieva, 2013).

1.2 Deconfined criticality

Deconfined criticality is a critical theory of second order phase transition which is out of the Landau-Ginzburg-Wilson paradigm (Senthil et al., 2004a,b). One classic example of this phenomenon is the Néel to valence bond solid (VBS) transition in square lattice. Néel phase breaks the SU(2) spin symmetry and VBS phase breaks the translation symmetry. The symmetry of the two phases, together with their order parameters, have very distinct structures. Therefore, the Landau's theory of symmetry breaking will suggest one of the following scenarios: (i) the phase transition is first order; (ii) there are two second order phase transition, with coexistence region in the middle; (iii) a single second order phase transition takes place with fine-tuned parameters. However, deconfined criticality suggests a direct continuous phase transition without any fine-tuning of parameters. At the deconfined critical point, the theory has fractionalized excitations, as well as a gapless 'photon' excitation. There is no direct experimental signature of deconfined criticality yet, but numerical evidences have been reported (Sandvik, 2007; Block et al., 2013).

The field theory of the Néel to VBS deconfined criticality is described in a CP^1 model. We write the Néel order parameter $\vec{N}$ in the CP^1 parameterization,

$$\vec{N} = z_\alpha^* \vec{\sigma}_{\alpha\beta} z_\beta. \tag{1.5}$$

Here, the z fields are the fractionalized spinon field, and $\vec{\sigma}$ is the spin Pauli matrices. The CP^1 parameterization has a gauge redundancy for the local phase rotation, and therefore the spinons are coupled to a compact U(1) gauge field, a_μ. The critical

theory of this spinon field coupled to the gauge field is written as a CP^1 model:

$$\mathcal{L}_z = \sum_{\alpha}^{2} |(\partial_\mu - ia_\mu)z_\alpha|^2 + s|z|^2 + u(|z|^2)^2 + \kappa(\epsilon_{\mu\nu\lambda}\partial_\nu a_\lambda)^2. \tag{1.6}$$

One conceptual route in describing deconfined criticality is through topological defects (Levin and Senthil, 2004). Let us again consider the example of Néel to VBS transition in a square lattice. As we approach the critical point starting from the deep VBS phase, topological defects of the VBS emerge. The topological defects of VBS are vortices of the Z_4 order parameter. An interesting observation is that one cannot construct a featureless vortex of the VBS order parameter. Whenever one creates a VBS vortex, there must be a site at the core which is not part of any singlet bond (Fig. 1.3(a)). This site with the 'dangling spin,' is an inevitable feature of the VBS vortex. This is geometrically due to the elongated geometry of the valance bonds; the order parameter effectively resides on the bond of the lattice, and not the site. In contrast, if the system has the Z_4 order on every site rather than on the bond; it is possible to have a featureless vortex of the Z_4 order parameter (Fig. 1.3(b)). We have seen that VBS vortices have spin-$\frac{1}{2}$ in square lattice. Now as we move very close to the critical point, these vortices proliferate throughout the system as VBS order diminishes, and the vortices will condense at the critical point. However, the vortices have spin quantum number, and the condensation of vortices results in the symmetry breaking of the SU(2) spin symmetry. This is why Néel order naturally arises as VBS order disappears, without any fine-tuning.

Therefore, as we write a field theory describing the phase transition between the VBS and Néel phase, it is not sufficient only to include the order parameters of the two phases in the theory. Their defects, VBS vortices and spin skyrmions, should also be included in the field theory. Moreover, it should take into account the intricate interplay between one phase and the other phase's defect, and vice versa. This is achieved by the Wess-Zumino-Witten (WZW) term in the case of the O(5) non-linear sigma model where the O(5) field consists of the two VBS order parameters and three Néel order parameters. The existence and implications of this WZW term are discussed in detail in Chapter 3.
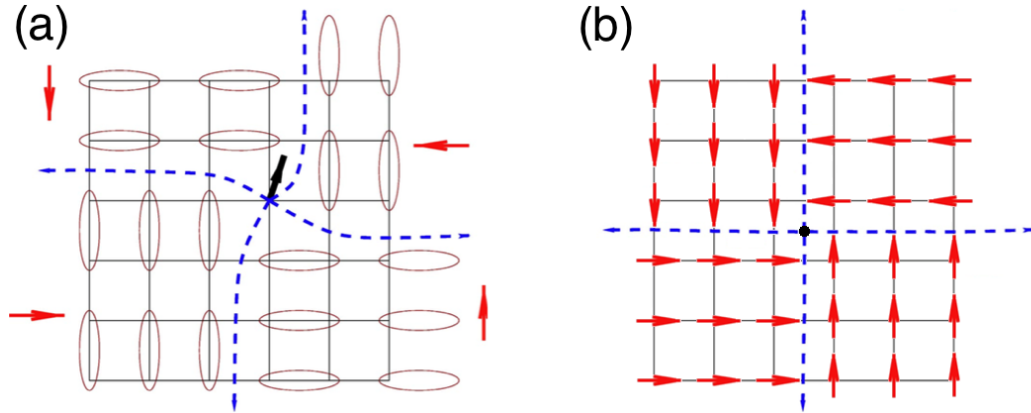
Figure 1.3: (a) VBS vortex in a square lattice, figure from Levin and Senthil (2004). The red arrows are the Z_4 order parameter and the blue dashed lines are the domain boundaries. Note that there is a free-site at the core of the vortex. (b) Vortex of the Z_4 order parameter at each site. In this case, the vortex is featureless.

1.3 Numerical methods in strongly correlated systems

There are many numerical methods which are widely used in strongly correlated systems. While we study a number of model systems hoping it contains the important physics of the much more complex real world, it is often true that we are not even able to solve the models analytically. For example, even for the Hubbard model, which was studied extensively for more than 50 years, analytical solutions exist only for the limit of $t/U \ll 1$ or $t/U \gg 1$ (t is the hopping parameter and U is the on-site interaction). Of course, many analytical methods are developed to investigate the intermediate region $t/U \sim 1$, but these have a rather limited scope. Numerical methods may provide "computational experiments" to certain models where analytical approach is out of reach. Although the method itself usually cannot explain the fundamental reasoning behind the result, it provides useful guidance and insights on constructing microscopic theories.

A number of numerical methods stem from the Wilsonian renormalization group (RG), each of which implements its own efficient approximation schemes. We will

encounter the density matrix renormalization group (DMRG) in Chapter 4, and the functional renormalization group (fRG) in Chapter 5.

1.3.1 Density matrix renormalization group

DMRG is a numerical method which is invented to effectively calculate the ground state of a strongly correlated system in one-dimension. In the core of its algorithm, we use the empirical knowledge that entanglements in many-body Hamiltonian ground states are relatively small (White, 1992; Schollwöck, 2005, 2011). The renormalization group in the name DMRG is in the sense of real space RG. However, an alternative perspective of DMRG as a matrix product state (MPS) calculation is very useful and can be generalized to other MPS methods such as projected entangled pair states (PEPS) or multi-scale entanglement renormalization ansatz (MERA).

DMRG is an intrinsically one-dimensional method which is extremely powerful. Its first result of $S = 1$ antiferromagnetic Heisenberg chain in White and Huse (1993) was surprisingly accurate, considering the computing power 20 years ago. However, the limitation of DMRG also comes from its one-dimensional nature. For its applications to two-dimensions, one needs to define a one-dimensional path covering the system, and the calculation is not as effective as in one-dimension. Two-dimensional calculations are mostly done in cylinder geometry. The amount of computation scales linearly as we increase the system size in the cylinder direction, but scales exponentially in increasing circumference direction. Therefore, the circumference dimension is the limiting factor in studying two-dimensional systems, and finite-size scaling is needed for quantities for thermodynamic limit. Except for systems with very low entanglement, computing the DMRG in the torus geometry is computationally very costly. One can instead implement the infinite system DMRG, which performs DMRG in an effectively infinite cylinder.

DMRG also has much advantage when studying entanglement entropies of a system (Laflorencie et al., 2006; Eisert et al., 2010; Jiang et al., 2012; Rodney et al., 2013). Thanks to the MPS form of the DMRG wavefunction, the calculation of entanglement entropy (and more generally the n-th Rényi entropy) is relatively straightforward.

We will use DMRG extensively in Chapter 4 to obtain the density profile of the ground state and study the entanglement entropy of the system.

1.3.2 Functional renormalization group

fRG is a collection of methods which systematically approximates the Wilsonian RG process (Salmhofer et al., 2004; Kopietz et al., 2010; Metzner et al., 2012). In the center of fRG is the "exact flow equation", also known as the "Wetterich equation," which is as follows,

$$\frac{d}{d\Lambda}\Gamma_R^\Lambda[\chi, \bar{\chi}] = \frac{1}{2}\text{Str}\left\{\dot{R}^\Lambda\left[\Gamma_R^{(2)\Lambda}[\chi, \bar{\chi}] + R^\Lambda\right]^{-1}\right\}. \tag{1.7}$$

Here, χ are the fields of the theory; it can be fermions, bosons, or a composite of both. Γ is the cutoff dependent effective action and it interpolates smoothly between the bare action and the fully effective action – when the cutoff scale (Λ) is at UV, Γ is the bare action, and when Λ is at IR (~ 0), Γ becomes the effective action. The (2) in the superscript means it is a second derivative in the fields, and Str is a supertrace which is same as the normal trace but includes a (-1) factor in the fermionic sector. R is a cutoff which regulates the IR divergence. Among a number of different cutoff schemes, we will be using an additive Litim cutoff. Litim cutoff has several advantages including the fact that it distorts the bare green's function less, and it is continuous, which is a benefit computation-wise. A detailed expression for the Litim cutoff will be in the main text. This exact flow equation is *exact* in the sense that this equation can be obtained by writing down the functional integration form of the cutoff dependent effective action, and differentiating it with the cutoff scale.

The exact flow equation has a neat compact form, but it cannot be solved without approximation. We have a number of approximation schemes to proceed. The first is the vertex expansion. This procedure expands the effective action in powers of the field. As a result, we will get one flow equation for all field combinations and they will compose an infinite hierarchy. Since it is impossible to solve the infinite sets of equations, we truncate this hierarchy at some point. Although we have eliminated

infinite numbers of flow equations, the remaining equations are still very complicated. This is because self-energy and vertex functions have momentum and frequency dependence. The second approximation, derivative expansion, can be used to simplify the each flow equations. Derivative expansion is expanding the self-energy and vertex functions in powers of momenta and frequency, and keeping the most relevant terms which are the lowest powers in the expansion. This gives a minimal and efficient scheme for obtaining critical exponents. Another popular alternative is to use a momenta or frequency grid, and solving order of thousands of coupled flow equations (Halboth and Metzner, 2000; Zanchi and Schulz, 2000; Honerkamp and Salmhofer, 2001).

One great advantage of fRG is that it is capable of considering every possible instability in equal footing. Moreover, since the approximation scheme is very systematic, one can control the approximation relatively easily. The method of fRG will be the central method of computation in Chapter 5.

1.4 Organization of the thesis

Starting from the next chapter, we will present a detailed study on novel quantum phase transitions in graphene and cuprates, building upon the materials from this chapter. The remainder of the thesis is organized as follows.

In Chapter 2 we propose that bilayer graphene can provide an experimental realization of deconfined criticality. Current experiments indicate the presence of Néel order in the presence of a moderate magnetic field. The Néel order can be destabilized by application of a transverse electric field. The resulting electric field induced state is likely to have valence bond solid order, and the transition can acquire the emergent fractionalized and gauge excitations of deconfined criticality.

In Chapter 3 we consider the interplay between the antiferromagnetic and Kekulé valence bond solid orderings in the zero energy Landau levels of neutral monolayer and bilayer graphene. We establish the presence of Wess-Zumino-Witten terms between these orders: this implies that their quantum fluctuations are described by

the deconfined critical theories of quantum spin systems. We present implications for experiments, including the possible presence of excitonic superfluidity in bilayer graphene.

In Chapter 4 we study a recently proposed quantum dimer model for the pseudo-gap metal state of the cuprates. The model contains bosonic dimers, representing a spin-singlet valence bond between a pair of electrons, and fermionic dimers, representing a quasiparticle with spin-$1/2$ and charge $+e$. By density matrix renormalization group calculations on a long but finite cylinder, we obtain the ground state density distribution of the fermionic dimers for a number of different total densities. From the Friedel oscillations at open boundaries, we deduce that the Fermi surface consists of small hole pockets near $(\pi/2, \pi/2)$, and this feature persists up to doping density $1/16$. We also compute the entanglement entropy and find that it closely matches the sum of the entanglement entropies of a critical boson and a low density of free fermions. Our results support the existence of a fractionalized Fermi liquid (FL*) in this model.

In Chapter 5 we present a functional renormalization group analysis of a quantum critical point in two-dimensional metals involving Fermi surface reconstruction due to the onset of spin-density wave order. Its critical theory is controlled by a fixed point in which the order parameter and fermionic quasiparticles are strongly coupled and acquire spectral functions with a common dynamic critical exponent. We obtain results for critical exponents and for the variation in the quasiparticle spectral weight around the Fermi surface. Our analysis is implemented on a two-band variant of the spin-fermion model which will allow comparison with sign-problem-free quantum Monte Carlo simulations.

Chapter 2

Deconfined criticality in bilayer graphene

2.1 Introduction

Undoped graphene, in both its monolayer and bilayer forms, is nominally a semi-metal. However, upon application of a moderate magnetic field, it turns into an insulator (Checkelsky et al., 2009) (in the quantum Hall terminology, this state has filling fraction $\nu = 0$). Evidence has been accumulating from recent experiments (Weitz et al., 2010; Freitag et al., 2012; Velasco et al., 2012; Young et al., 2012; Maher et al., 2013; Freitag et al., 2013; Young et al., 2014) that the insulator has symmetry breaking due to the appearance of antiferromagnetic long-range order. Because of the applied magnetic field, the antiferromagnetic order is expected to lie in the plane orthogonal to the magnetic field, along with a ferromagnetic "canting" of the spins along the direction of the magnetic field: this state is therefore referred to as a canted antiferromagnet (CAF). For the case of bilayer graphene, experiments (Weitz et al., 2010; Freitag et al., 2012; Velasco et al., 2012; Maher et al., 2013; Freitag et al., 2013) have also induced what appears to be a quantum phase transition out of the CAF state. This is done by applying an electric field transverse to the layers, leading to states with layer polarization of electric charge, but presumably without
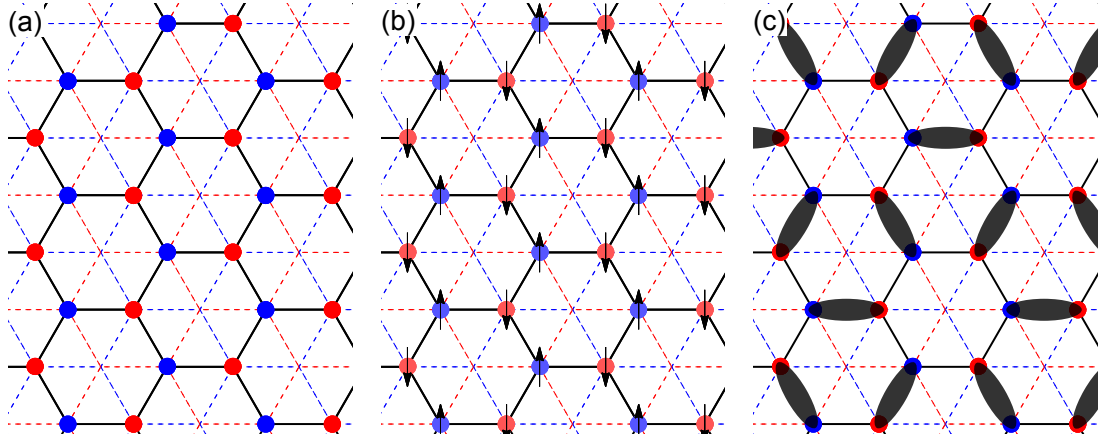
Figure 2.1: (a) Top view of AB stacked bilayer graphene. Λ_a and Λ_b are the sublattices of layer A of graphene, which is the dashed red line in the figure; the sites of Λ_b are colored blue, and Λ_c and Λ_d are the sublattices of layer B, which is the dashed blue line; the sites of Λ_c are colored red. The sites of Λ_a and Λ_d are present at the same r in the plane of graphene. Λ_b and Λ_c also makes a honeycomb lattice, which is depicted as the thick black line. This is the effective honeycomb lattice where the Néel and VBS order reside. (b) Néel order in the effective honeycomb lattice. (c) One of the three VBS states in the effective lattice. The black oval depicts the singlet bonds. Note that 1/3 of the hexagons in the VBS state have no valence bonds, and so this state can also be viewed as having "plaquette" order on these hexagons.

antiferromagnetic order.

Theoretically, the CAF is expected to be stable in bilayer graphene over a range of microscopic parameters (Nandkishore and Levitov, 2010; Cvetkovic et al., 2012; Zhang et al., 2012). Studying the instability of the CAF in a Hartree-Fock analysis, Kharitonov (Kharitonov, 2012a,b,c,d) proposed phase diagrams that apply to the experimental configurations: he found that upon application of an electric field, the CAF state undergoes a quantum phase transition into a state with partial-layer-polarization (PLP) and a distinct broken symmetry: the PLP state preserves spin rotation invariance, but breaks lattice symmetries in the Kekulé pattern (see Fig. 2.1(c)). The insulating CAF and PLP states, and the transition between them, will be the focus of our present study. There is no direct experimental evidence yet for the Kekulé broken symmetry in the PLP state, but we hope this will be the focus of future

experiments.

From the perspective of symmetry, we are therefore investigating the quantum phase transition between two insulating states in an electronic model that has spin rotation symmetry and the space group symmetries of the honeycomb lattice. One insulator breaks spin rotation symmetry by the appearance of antiferromagnetic long-range order in the two-sublattice pattern shown in Fig. 2.1(b): we will henceforth refer to this insulator as the Néel state. The second insulator breaks the space group symmetry alone in the Kekulé pattern of Fig. 2.1(c). A direct quantum phase transition between two insulators with precisely the same symmetries was first discussed some time ago in Read and Sachdev (1990) in the very different context of correlated electron models inspired by the cuprate high-temperature superconductors. In these models, the Kekulé state is referred to as a valence bond solid (VBS), as the space group symmetry is broken by singlet valence bonds between spins on the sites of the honeycomb lattice; we include the "plaquette" resonating state within the class of VBS states, and it breaks the honeycomb lattice symmetry in the same pattern.

More recently, the Néel-VBS transition has been identified (Senthil et al., 2004a,b) as a likely candidate for "deconfined criticality." In this theory, the low-energy excitations in the vicinity of the transition are described by neutral excitations carrying spin $S = 1/2$ ("spinons") coupled to each other by the "photon" of an emergent U(1) gauge field. The quantum transition itself is either second order or weakly first order; in either case, there is evidence for the presence of the emergent gauge excitations (Sandvik, 2007; Block et al., 2013).

In the present chapter, we will apply a strong coupling perspective to models on the bilayer honeycomb lattice linked to the physics of bilayer graphene. Our analysis therefore complements that of Kharitonov, who perturbatively examined the effect of interactions after projecting to the lowest Landau level. We also note other theoretical studies by Roy and collaborators (Roy, 2013, 2014; Roy et al., 2014), which do not project to the lowest Landau level. Our perspective is more suited to addressing the nature of quantum fluctuations near the quantum phase transition, and for describing the possible emergence of exotic varieties of fractionalization. We will discuss some

of the experimental consequences of this new perspective in Chapter 2.8.

We will introduce our lattice model on the bilayer honeycomb lattice in Chapter 2.2. We assume that the strongest coupling in the model is the on-site Hubbard repulsion U, and perform a traditional $1/U$ expansion to obtain an effective spin model on the same lattice. In Chapter 2.3, we examine this spin model in a spin-wave expansion, and determine regimes where the Néel order is suppressed. An alternative effective spin model, related to those examined in recent numerical work, is studied in Chapter 2.4. We study the geometric phases between the Néel and VBS orders in Chapters 2.5 and 2.6, and comment on the structure of vortices in the VBS order in Chapter 2.7.

2.2 The strong coupling model

We start our analysis from the extended Hubbard model for AB stacked bilayer graphene in the strong coupling limit. A top view of AB stacked bilayer graphene is shown in Fig. 2.1(a). In our coordinate system, we set the lattice constant to 1 and define $\boldsymbol{s}_1 = (1, 0)$, $\boldsymbol{s}_2 = (-1/2, \sqrt{3}/2)$, and $\boldsymbol{s}_3 = (-1/2, -\sqrt{3}/2)$:

$$
\begin{aligned}
H = &- t_\parallel \sum_{\boldsymbol{r} \in \Lambda_a} \sum_{i=1}^3 c_{\boldsymbol{r}}^{(a)\dagger} c_{\boldsymbol{r}+\boldsymbol{s}_i}^{(b)} - t_\parallel \sum_{\boldsymbol{r} \in \Lambda_d} \sum_{i=1}^3 c_{\boldsymbol{r}}^{(d)\dagger} c_{\boldsymbol{r}-\boldsymbol{s}_i}^{(c)} - t_\perp \sum_{\boldsymbol{r} \in \Lambda_a} c_{\boldsymbol{r}}^{(a)\dagger} c_{\boldsymbol{r}}^{(d)} \\
&+ \text{h.c.} + U \sum_{\alpha=a,b,c,d} \sum_{\boldsymbol{r} \in \Lambda_\alpha} \frac{n_{\boldsymbol{r}}^{(\alpha)}(n_{\boldsymbol{r}}^{(\alpha)} - 1)}{2} \\
&+ V_\parallel \sum_{\boldsymbol{r} \in \Lambda_a} \sum_{i=1}^3 n_{\boldsymbol{r}}^{(a)} n_{\boldsymbol{r}+\boldsymbol{s}_i}^{(b)} + V_\parallel \sum_{\boldsymbol{r} \in \Lambda_d} \sum_{i=1}^3 n_{\boldsymbol{r}}^{(d)} n_{\boldsymbol{r}-\boldsymbol{s}_i}^{(c)} + V_\perp \sum_{\boldsymbol{r} \in \Lambda_a} n_{\boldsymbol{r}}^{(a)} n_{\boldsymbol{r}}^{(d)} \\
&+ E \left(-\sum_{\boldsymbol{r} \in \Lambda_a} n_{\boldsymbol{r}}^{(a)} - \sum_{\boldsymbol{r} \in \Lambda_b} n_{\boldsymbol{r}}^{(b)} + \sum_{\boldsymbol{r} \in \Lambda_c} n_{\boldsymbol{r}}^{(c)} + \sum_{\boldsymbol{r} \in \Lambda_d} n_{\boldsymbol{r}}^{(d)} \right)
\end{aligned}
\tag{2.1}
$$

Here $c^\dagger$ (c) is the fermion creation (annihilation) operator and $n = c^\dagger c$ is the number operator. $t_\parallel$ and $V_\parallel$ are the tight-binding hopping parameter and the nearest-neighbor interaction within the plane, $t_\perp$ and $V_\perp$ are those between the planes, and U is the on-site interaction. We label each layer of graphene as A and B: layer A consists of

sublattices Λ_a and Λ_b, and layer B consists of sublattices Λ_c and Λ_d. Only one of the sublattices in each layer has common in-plane coordinate in AB stacked bilayer graphene, and we set those to be Λ_a and Λ_d. Elsewhere in the literature, the site labels a, b, c, and d are often referred to as $A1$, $B1$, $A2$, and $B2$, respectively, meaning sublattice $A(B)$ or layer $1(2)$. However, we find it more convenient to use the compact notation a, b, c, d. Hopping and interaction between the layers only occurs between these sublattices. We also include an electric field transverse to the plane of graphene, pointing from layer A to layer B. The electric field is minimally coupled to the density of the fermions with coupling E. We assume that E is also smaller than U, and so both layers will be half-filled at leading order in $1/U$, and the effective Hamiltonian can be expressed only in terms of spin operators on the sites. The subleading $1/U$ corrections will induce terms in the effective Hamiltonian, but also induce a polarization in the layer density when computed in terms of the bare electron operators.

Our Hamiltonian does not explicitly include the influence of an applied magnetic field. Such a field will modify H in two ways, via a Peierls phase factor on the hopping terms $t_{\parallel,\perp}$, and a Zeeman coupling. In the context of our strong coupling expansion, the influence of the Peierls phases will only be to modify the coefficients of ring-exchange terms in the effective spin Hamiltonian. However, such ring-exchange terms only appear at sixth order in $t_\parallel$, and this is higher order than our present analysis; so we can safely drop the Peierls phases. The Zeeman term commutes with all other terms in H, and so does not modify the analysis below, and can be included as needed in the final effective Hamiltonian.

From this Hamiltonian, we work on the strong coupling limit, where $t_\parallel, t_\perp \ll U, V$, and perform the t/U expansion up to $\mathcal{O}(t^4/U^3)$ order. In this expansion we assume both $t_\parallel$ and $t_\perp$ are much smaller than U, although this is not well satisfied in the experiment (also, there is a significant difference in the values of the hopping parameters from Zhang et al. (2008), $t_\parallel \sim 3.0$ eV, $t_\perp \sim 0.40$ eV). There are numerous works on the t/U expansion of the Hubbard model in various lattices, including the classic work of MacDonald et al. (1988) and Takahashi (1977) in square lattice. Extra

care is needed while dealing the similar procedure with the above model since we have included nearest neighbor interaction and the lattice structure is more complicated.

First, we organize the Hamiltonian in Eq. (2.1) as $H = H_U + H_t$, where H_U is the interaction term and H_t is the kinetic term. We consider H_t as the perturbation and rearrange it by the change of interaction energy through the hopping process,

$$H_t = \sum_\lambda \left[T_\lambda + T_{-\lambda} \right]. \tag{2.2}$$

T_λ is the sum of all hopping terms that increases the interaction energy by λU. For notational convenience, we restrict λ to be positive and collect the decreasing energy processes to $T_{-\lambda}$ with an explicit negative sign.

By systematically performing the unitary transformation, we may obtain the effective Hamiltonian $H^{(n)}$, which contains terms up to the order of t^{n+1}/U^n for arbitrary n (MacDonald et al., 1988; Takahashi, 1977). We present the result of $H^{(3)}$ for the system in the ground-state manifold at half-filling without long derivation:

$$\begin{aligned}
H_{GS,HF}^{(3)} = &-\frac{1}{U} \sum_\lambda \frac{1}{\lambda} T_{-\lambda} T_\lambda \\
&+ \frac{1}{2U^3} \sum_{\lambda_1,\lambda_2} \frac{1}{\lambda_1 \lambda_2} \left(\frac{1}{\lambda_1} + \frac{1}{\lambda_2} \right) T_{-\lambda_1} T_{\lambda_1} T_{-\lambda_2} T_{\lambda_2} \\
&- \frac{1}{U^3} \sum_{\substack{\lambda_1+\lambda_2=\lambda_3+\lambda_4 \\ \lambda_1 \neq \lambda_3}} \frac{1}{\lambda_1 \lambda_4 (\lambda_1 - \lambda_3)} T_{-\lambda_1} T_{\lambda_3} T_{-\lambda_2} T_{\lambda_4} \\
&- \frac{1}{U^3} \sum_{\lambda_1+\lambda_2=\lambda_3+\lambda_4} \frac{1}{\lambda_1 \lambda_4 (\lambda_1 + \lambda_2)} T_{-\lambda_1} T_{-\lambda_2} T_{\lambda_3} T_{\lambda_4}. \tag{2.3}
\end{aligned}$$

The above expression is a general result for a Hubbard-type Hamiltonian and will hold for any bipartite lattice regardless of the dimension.

Applying Eq. (2.3) to our specific case of bilayer graphene, we obtain a spin

Hamiltonian that contains every term up to the order of t^4/U^3,

$$
\begin{aligned}
H &= J_\parallel \sum_{\boldsymbol{r}\in\Lambda_a} \sum_{i=1}^{3} \vec{S}_{\boldsymbol{r}}^{(a)} \cdot \vec{S}_{\boldsymbol{r}+\boldsymbol{s}_i}^{(b)} + J_\parallel \sum_{\boldsymbol{r}\in\Lambda_d} \sum_{i=1}^{3} \vec{S}_{\boldsymbol{r}}^{(d)} \cdot \vec{S}_{\boldsymbol{r}-\boldsymbol{s}_i}^{(c)} \\
&+ J_\perp \sum_{\boldsymbol{r}\in\Lambda_a} \vec{S}_{\boldsymbol{r}}^{(a)} \cdot \vec{S}_{\boldsymbol{r}}^{(d)} + J_2 \sum_{\alpha=a,b,c,d} \sum_{\boldsymbol{r}\in\Lambda_\alpha} \sum_{i=1}^{3} \vec{S}_{\boldsymbol{r}}^{(\alpha)} \cdot \vec{S}_{\boldsymbol{r}+\boldsymbol{t}_i}^{(\alpha)} \\
&+ J_\times \sum_{\boldsymbol{r}\in\Lambda_a} \sum_{i=1}^{3} \vec{S}_{\boldsymbol{r}}^{(a)} \cdot \vec{S}_{\boldsymbol{r}-\boldsymbol{s}_i}^{(c)} + J_\times \sum_{\boldsymbol{r}\in\Lambda_d} \sum_{i=1}^{3} \vec{S}_{\boldsymbol{r}}^{(d)} \cdot \vec{S}_{\boldsymbol{r}+\boldsymbol{s}_i}^{(b)},
\end{aligned}
\tag{2.4}
$$

with the exchange couplings as,

$$
\begin{aligned}
J_\parallel &= \frac{4\, t_\parallel^2}{U - V_\parallel - \left(\frac{V_\perp^2}{U-V_\parallel}\right)}, \qquad J_\perp = \frac{4\, t_\perp^2}{U - V_\perp - \left(\frac{E^2}{U-V_\perp}\right)}, \\
J_2 &= \frac{4\, t_\parallel^4}{(U-V_\parallel)^2 - V_\perp^2} \left(\frac{2(U-V_\parallel)\left((U-V_\parallel)^2 + V_\perp^2\right)}{\left((U-V_\parallel)^2 - V_\perp^2\right)^2} - \frac{1}{U} \right),
\end{aligned}
\tag{2.5}
$$

and,

$$
\begin{aligned}
J_\times =& \frac{4\, t_\parallel^2 t_\perp^2}{\left((U-V_\parallel^2)^2 - V_\perp^2\right)^2 \left((U-V_\perp)^2 - E^2\right)^2 \left((U+V_\perp)^2 - E^2\right)} \times \\
& \left\{ (U-V_\perp)^2(U+V_\perp) \left[(U^2 + V_\perp U - V_\parallel V_\perp)(U-V_\parallel)^2 - V_\perp^2(U^2 - (4V_\parallel - V_\perp)U \right.\right. \\
& \left. + (2V_\parallel - V_\perp)V_\parallel) \right] - E^2 \left[2U^5 - (4V_\parallel + 5V_\perp)U^4 + (2V_\parallel^2 + 13V_\parallel V_\perp + 8V_\perp^2)U^3 \right. \\
& - V_\perp(V_\parallel + V_\perp)(11V_\parallel + 2V_\perp)U^2 + V_\perp(V_\parallel + V_\perp)(3V_\parallel - V_\perp)(V_\parallel + 2V_\perp)U \\
& \left.\left. - V_\perp^2(V_\parallel^3 + 3V_\parallel^2 V_\perp - V_\parallel V_\perp^2 + V_\perp^3) \right] + E^4(U-V_\perp)[(U-V_\parallel)^2 + V_\perp^2] \right\}.
\end{aligned}
\tag{2.6}
$$

We have additionally defined $\boldsymbol{t}_1 = \boldsymbol{s}_2 - \boldsymbol{s}_3$, $\boldsymbol{t}_2 = \boldsymbol{s}_3 - \boldsymbol{s}_1$, and $\boldsymbol{t}_3 = \boldsymbol{s}_1 - \boldsymbol{s}_2$. Without the electric field, the lattice symmetry guarantees the $J_\times$ coupling in $\vec{S}_{\boldsymbol{r}}^{(a)} \cdot \vec{S}_{\boldsymbol{r}-\boldsymbol{s}_i}^{(c)}$ and $\vec{S}_{\boldsymbol{r}}^{(d)} \cdot \vec{S}_{\boldsymbol{r}+\boldsymbol{s}_i}^{(b)}$ to be the same. However, when the field is turned on, the layer symmetry breaks and the two $J_\times$ values become different. Here, we take the average value for simplicity. This will not change the qualitative behavior unless E is very large. Different exchange couplings defined in Eq. (2.4) are shown schematically in Fig. 2.2. We work in the parameter range where all four exchange couplings
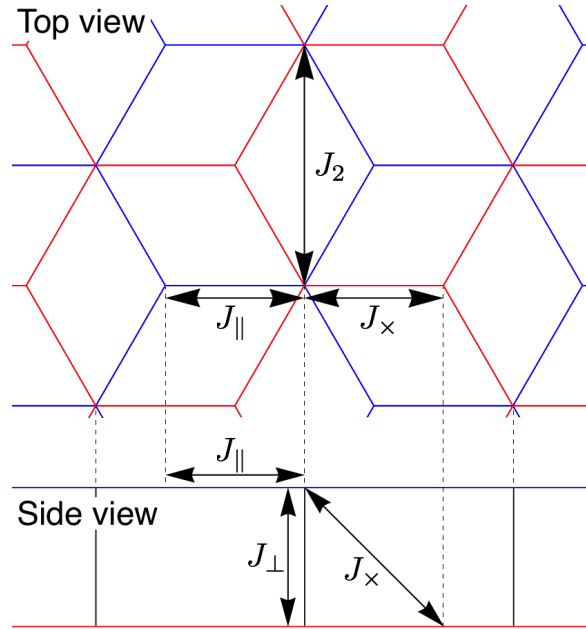
Figure 2.2: Top and side views of the AB stacked bilayer graphene. Exchange couplings $J_\parallel$, $J_\perp$, J_2, and $J_\times$ are shown in the figure. The top view can be considered the same as in Fig. 2.1(a), without the effective honeycomb lattice depicted in thick black line. Layers A and B are the red and blue lattices as in Fig. 2.1. In the side view, the black lines depict the lattice sites connected by the $t_\perp$ hopping parameter in Eq. (2.1). The dashed lines are guide to the eye showing that the horizontal coordinates are the same for the two views. As we can see from the figure, $J_\parallel$ is between nearest neighbors within one layer, $J_\perp$ is between nearest neighbors of different layers, J_2 is between next nearest neighbors within one layer, and $J_\times$ is between next nearest neighbors of different layers.

are antiferromagnetic. This can be made compatible with the experimental data of hopping parameters (Zhang et al., 2008). Moreover, in most of the parameter regime where $J_\parallel$ and $J_\perp$ are antiferromagnetic, we find J_2 and $J_\times$ to be positive as well. Therefore, we have enough parameter space to explore with this model and do not have to fine-tune the parameters.

2.3   Spin-wave expansion

Previous studies of the bilayer antiferromagnet have focused on the square lattice
(Hida, 1990; Sandvik et al., 1995; Chubukov and Morr, 1995; Millis and Monien, 1996;
Wang et al., 2006) where the sites are stacked directly on top of each other. In these
models, as the interlayer coupling is increased, there is eventually a transition from
the Néel state to a "trivial" paramagnet in which the ground state is approximately
the product of interlayer valence bonds between superposed spins. However, here we
are considering a staggered stacking, in which no such trivial one-to-one identifica-
tion of spins between the two layers is possible. Any pairing of spins must break a
lattice symmetry, and this is a simple argument for the appearance of a VBS state.
Nevertheless, it is useful to apply the spin-wave expansion used for the square lattice
(Hida, 1990; Chubukov and Morr, 1995), and study how the intra- and inter-layer
couplings modify the staggered magnetization. This will help us determine the pa-
rameter regime over which the Néel order decreases, and a possible VBS state can
appear. However, a description of the transition to, and structure of, the VBS state
is beyond the regime of applicability of the spin-wave expansion.

Among the four exchange couplings listed in Eqs. (2.5) and (2.6), only $J_\perp$ and $J_\times$
depend on the electric field strength, E. The electric field breaks the layer symmetry,
so it is reasonable that E is only included in the exchange coupling between different
layers. We start from the Néel phase and calculate the staggered magnetization of
the bilayer graphene as a function of either $J_\perp$, $J_\times$, or E. Since our starting point is
an SU(2) symmetry broken state, we use the Holstein-Primakoff representation.

Starting from the effective spin Hamiltonian derived in Eq. (2.4), we perform
the $1/S$ expansion (where S is the magnitude of the spin, and we are interested
in $S = 1/2$) about the antiferromagnetically ordered state by expressing the spin

operators in terms of bosons, a, b, c, d:

$$S_z^{(a)} = S - a^\dagger a, \qquad S_+^{(a)} = \sqrt{2S}(1 - a^\dagger a/(2S))^{1/2}a,$$
$$S_z^{(b)} = -S + b^\dagger b, \qquad S_+^{(b)} = \sqrt{2S}b^\dagger(1 - b^\dagger b/(2S))^{1/2},$$
$$S_z^{(c)} = S - c^\dagger c, \qquad S_+^{(c)} = \sqrt{2S}(1 - c^\dagger c/(2S))^{1/2}c,$$
$$S_z^{(d)} = -S + d^\dagger d, \qquad S_+^{(d)} = \sqrt{2S}d^\dagger(1 - d^\dagger d/(2S))^{1/2}. \tag{2.7}$$

Then, to the needed order, the Hamiltonian is,

$$
\begin{aligned}
H = {}& J_\parallel \sum_{\boldsymbol{r}\in\Lambda_a} \sum_{i=1}^{3} \left(-S^2 + S(a_{\boldsymbol{r}}^\dagger a_{\boldsymbol{r}} + b_{\boldsymbol{r}+\boldsymbol{s}_i}^\dagger b_{\boldsymbol{r}+\boldsymbol{s}_i} + a_{\boldsymbol{r}}^\dagger b_{\boldsymbol{r}+\boldsymbol{s}_i}^\dagger + a_{\boldsymbol{r}} b_{\boldsymbol{r}+\boldsymbol{s}_i}) \right) \\
& + J_\parallel \sum_{\boldsymbol{r}\in\Lambda_d} \sum_{i=1}^{3} \left(-S^2 + S(d_{\boldsymbol{r}}^\dagger d_{\boldsymbol{r}} + c_{\boldsymbol{r}-\boldsymbol{s}_i}^\dagger c_{\boldsymbol{r}-\boldsymbol{s}_i} + d_{\boldsymbol{r}}^\dagger c_{\boldsymbol{r}-\boldsymbol{s}_i}^\dagger + d_{\boldsymbol{r}} c_{\boldsymbol{r}-\boldsymbol{s}_i}) \right) \\
& + J_\perp \sum_{\boldsymbol{r}\in\Lambda_a} \left(-S^2 + S(a_{\boldsymbol{r}}^\dagger a_{\boldsymbol{r}} + d_{\boldsymbol{r}}^\dagger d_{\boldsymbol{r}} + a_{\boldsymbol{r}}^\dagger d_{\boldsymbol{r}}^\dagger + a_{\boldsymbol{r}} d_{\boldsymbol{r}}) \right) \\
& + J_2 \sum_{\boldsymbol{r}\in\Lambda_a} \sum_{i=1}^{3} \left(S^2 + S(-a_{\boldsymbol{r}}^\dagger a_{\boldsymbol{r}} - a_{\boldsymbol{r}+\boldsymbol{t}_i}^\dagger a_{\boldsymbol{r}+\boldsymbol{t}_i} + a_{\boldsymbol{r}}^\dagger a_{\boldsymbol{r}+\boldsymbol{t}_i} + a_{\boldsymbol{r}+\boldsymbol{t}_i}^\dagger a_{\boldsymbol{r}}) \right) \\
& + J_2 \sum_{\boldsymbol{r}\in\Lambda_b} \sum_{i=1}^{3} \left(S^2 + S(-b_{\boldsymbol{r}}^\dagger b_{\boldsymbol{r}} - b_{\boldsymbol{r}+\boldsymbol{t}_i}^\dagger b_{\boldsymbol{r}+\boldsymbol{t}_i} + b_{\boldsymbol{r}}^\dagger b_{\boldsymbol{r}+\boldsymbol{t}_i} + b_{\boldsymbol{r}+\boldsymbol{t}_i}^\dagger b_{\boldsymbol{r}}) \right) \\
& + J_2 \sum_{\boldsymbol{r}\in\Lambda_c} \sum_{i=1}^{3} \left(S^2 + S(-c_{\boldsymbol{r}}^\dagger c_{\boldsymbol{r}} - c_{\boldsymbol{r}+\boldsymbol{t}_i}^\dagger c_{\boldsymbol{r}+\boldsymbol{t}_i} + c_{\boldsymbol{r}}^\dagger c_{\boldsymbol{r}+\boldsymbol{t}_i} + c_{\boldsymbol{r}+\boldsymbol{t}_i}^\dagger c_{\boldsymbol{r}}) \right) \\
& + J_2 \sum_{\boldsymbol{r}\in\Lambda_d} \sum_{i=1}^{3} \left(S^2 + S(-d_{\boldsymbol{r}}^\dagger d_{\boldsymbol{r}} - d_{\boldsymbol{r}+\boldsymbol{t}_i}^\dagger d_{\boldsymbol{r}+\boldsymbol{t}_i} + d_{\boldsymbol{r}}^\dagger d_{\boldsymbol{r}+\boldsymbol{t}_i} + d_{\boldsymbol{r}+\boldsymbol{t}_i}^\dagger d_{\boldsymbol{r}}) \right) \\
& + J_\times \sum_{\boldsymbol{r}\in\Lambda_a} \sum_{i=1}^{3} \left(S^2 + S(-a_{\boldsymbol{r}}^\dagger a_{\boldsymbol{r}} - c_{\boldsymbol{r}-\boldsymbol{s}_i}^\dagger c_{\boldsymbol{r}-\boldsymbol{s}_i} + a_{\boldsymbol{r}}^\dagger c_{\boldsymbol{r}-\boldsymbol{s}_i} + c_{\boldsymbol{r}-\boldsymbol{s}_i}^\dagger a_{\boldsymbol{r}}) \right) \\
& + J_\times \sum_{\boldsymbol{r}\in\Lambda_d} \sum_{i=1}^{3} \left(S^2 + S(-d_{\boldsymbol{r}}^\dagger d_{\boldsymbol{r}} - b_{\boldsymbol{r}+\boldsymbol{s}_i}^\dagger b_{\boldsymbol{r}+\boldsymbol{s}_i} + d_{\boldsymbol{r}}^\dagger b_{\boldsymbol{r}+\boldsymbol{s}_i} + b_{\boldsymbol{r}+\boldsymbol{s}_i}^\dagger d_{\boldsymbol{r}}) \right).
\end{aligned}
\tag{2.8}
$$

We write this in momentum space as,

$$H = -3NS(S+1)(2J_\parallel + J_\perp/3 - 4J_2 - 2J_\times) + S\sum_{\boldsymbol{k}} \Psi_{\boldsymbol{k}}^\dagger M(\boldsymbol{k})\Psi_k, \tag{2.9}$$

where N is the number of sites in Λ_a, $\Psi_{\boldsymbol{k}}$ is the boson spinor $\Psi_{\boldsymbol{k}} = (a_{\boldsymbol{k}}, c_{\boldsymbol{k}}, b^{\dagger}_{-\boldsymbol{k}}, d^{\dagger}_{-\boldsymbol{k}})$, and

$$
M(\boldsymbol{k}) = \begin{pmatrix}
\tilde{J}(\boldsymbol{k}) + J_{\perp} & J_{\times}\gamma(-\boldsymbol{k}) & J_{\parallel}\gamma(\boldsymbol{k}) & J_{\perp} \\
J_{\times}\gamma(\boldsymbol{k}) & \tilde{J}(\boldsymbol{k}) & 0 & J_{\parallel}\gamma(\boldsymbol{k}) \\
J_{\parallel}\gamma(-\boldsymbol{k}) & 0 & \tilde{J}(\boldsymbol{k}) & J_{\times}\gamma(-\boldsymbol{k}) \\
J_{\perp} & J_{\parallel}\gamma(-\boldsymbol{k}) & J_{\times}\gamma(\boldsymbol{k}) & \tilde{J}(\boldsymbol{k}) + J_{\perp}
\end{pmatrix},
$$

with

$$
\begin{aligned}
\tilde{J}(\boldsymbol{k}) &= J_{\parallel} + J_2\Gamma(\boldsymbol{k}) - 3J_{\times}, \\
\gamma(\boldsymbol{k}) &= \sum_{i=1}^{3} e^{i\boldsymbol{k}\cdot\boldsymbol{s}_i}, \\
\Gamma(\boldsymbol{k}) &= -6 + 2\sum_{i=1}^{3} \cos\left(\boldsymbol{k}\cdot\boldsymbol{t}_i\right).
\end{aligned}
$$

The Hamiltonian can be diagonalized by a bosonic version of the Bogoliubov transformation (which is not a unitary transformation) as described in Sachdev (1992).

Now the staggered magnetization of the bilayer graphene can be obtained from the diagonalized Hamiltonian. The expression for the magnetization is very complicated with all four exchange couplings, and hard to write down in a closed form. Therefore we present numerical values for a selected set of parameters. Fig. 2.3 shows the calculated magnetization as a function of $J_{\perp}$ and $J_{\times}$ for parameters $J_{\parallel}/U = 0.089$, $J_2/U = 0.0095$, $J_{\times}/U = 0.0018$, and $J_{\perp}/U = 0.028$ (unless one is the variable for the graph). These correspond to $t_{\parallel}/U = 0.1$, $t_{\perp}/U = 0.07$, $V_{\parallel}/U = 0.4$, and $V_{\perp}/U = 0.3$ for the parameters in the extended Hubbard model. Since the sublattices $\Lambda_a(\Lambda_d)$ and $\Lambda_b(\Lambda_c)$ are not symmetric in AB-stacked bilayer graphene, they will in general have different magnetization, and therefore are plotted separately (for example, sites in $\Lambda_a(\Lambda_d)$ has coordination number of 4, whereas the sites in $\Lambda_b(\Lambda_c)$ has 3). As depicted in Fig. 2.1, the Néel and VBS states of interest reside in Λ_b and Λ_c. We are therefore more interested in the magnetization of Λ_b than Λ_a.

We observe that the magnetization in each sublattice decreases as $J_{\times}$ increases. This is reasonable in the sense that antiferromagnetic $J_{\times}$ increases frustration of the
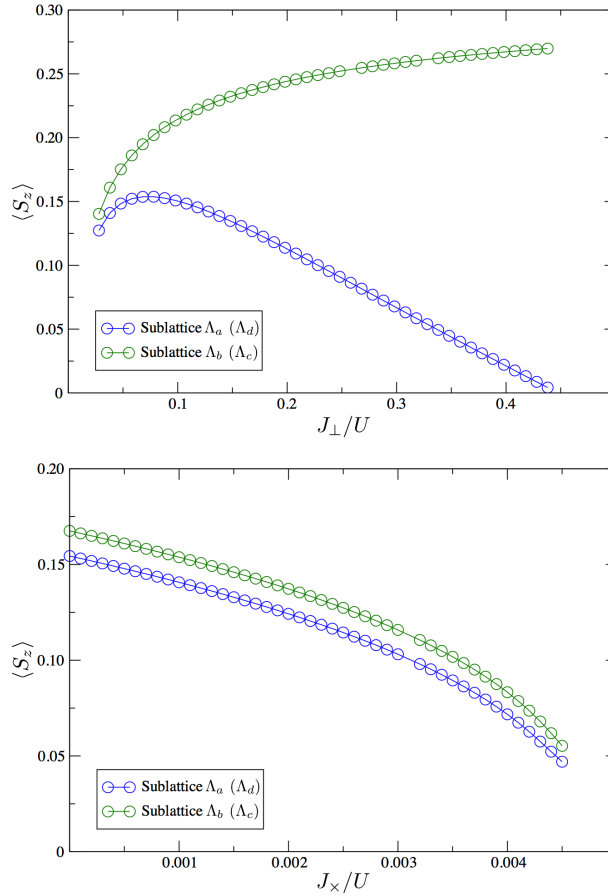
Figure 2.3: Magnetization of each sublattice in bilayer graphene as a function of $J_\perp$ (left) and $J_\times$ (right). We used $J_\parallel/U = 0.089$, $J_2/U = 0.0095$ for both plots, $J_\times/U = 0.0018$ for the left plot, and $J_\perp/U = 0.028$ for the right plot.

Néel phase. However, when $J_\perp$ increases, the magnetization of Λ_b increases while that of Λ_a decreases. This is mainly because $J_\times$ frustrates all four sublattices, but $J_\perp$ only gives frustration to Λ_a and Λ_d. That is, the Néel phase in Λ_b and Λ_c is not directly effected by $J_\perp$. We will explore again, in the next section, the influence of $J_\perp$ to Λ_b and Λ_c in the subleading order in a perturbation theory in large $J_\perp$. The result is an antiferromagnetic coupling between spins in Λ_b and Λ_c, and a ferromagnetic coupling between spins within Λ_b or Λ_c. This suggests a "layer-polarized antiferromagnet" state where, for example, every spin in Λ_b is polarized up, and every spin on Λ_c is

polarized down. So the increased magnetization of Λ_b can be explained in this manner. This is not the scenario we expect in the Néel to VBS phase transition, because the Néel order is becoming stronger with an increase of $J_\perp$. However, there will not be a case where $J_\perp$ increases alone because $J_\times$ coupling will also increase as we increase the electric field. This $J_\times$ gives frustration to the layer-polarized order, which will result in the decrease of the staggered magnetization. Note that, in any case, the magnetization is smaller for Λ_a than Λ_b, which contradicts our usual intuition that a larger coordination number agrees better with the mean-field result. However, this result is in accordance with Lang et al. (2012), where they find the same behavior by quantum Monte Carlo simulation for a Heisenberg model with only $J_\parallel$ and $J_\perp$ couplings, but in a wide range of $J_\perp$.

To obtain the staggered magnetization for more realistic states, including the ones in experiments, we need to consider the change of $J_\perp$ and $J_\times$ in a consistent manner. This is done by tuning a single parameter E, the coupling of electric field. Using the expressions in Eqs. (2.5) and (2.6), we can find the magnetizations for each sublattice as a function of E. As for the previous results, we only show numerical results for selected parameters. Fig. 2.4 shows the result for the same parameters as in Fig. 2.3, $t_\parallel/U = 0.1$, $t_\perp/U = 0.07$, $V_\parallel/U = 0.4$, and $V_\perp/U = 0.3$. We observe the magnetization of Λ_a decrease drastically from $E \sim 0.50U$ and that of Λ_b starts to decrease from $E \sim 0.55U$, although we cannot see a significant decrease in Λ_b before the Holstein-Primakoff theory breaks down. However, from the two plots in Fig. 2.3 where the magnetization of Λ_b saturates as increasing $J_\perp$ and vanishes as increasing $J_\times$, we can argue that when both $J_\perp$, $J_\times$ are increasing the magnetization will decrease eventually, and Fig. 2.4 is showing the onset of the decrease. This result shows explicitly how the Néel order decreases as the electric field increases.

2.4 J_1-J_2 **model**

The fact that the magnetization of Λ_a and Λ_d decreases faster than that of Λ_b and Λ_c in the previous section can be taken as evidence that, in the phase transition we
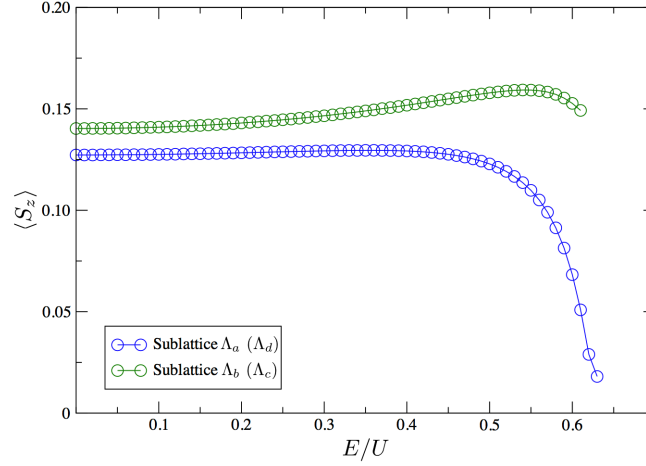
Figure 2.4: Magnetization as a function of electric field coupling, E. Parameters used are $t_\parallel/U = 0.1$, $t_\perp/U = 0.07$, $V_\parallel/U = 0.4$, and $V_\perp/U = 0.3$. According to Eqs. (2.5) and (2.6), these parameters match the exchange coupling values used in Fig. 2.3.

are concerned with, it is sufficient to consider sublattices Λ_b and Λ_c in the effective theory, *i.e.*, the effective single layer honeycomb depicted in Fig. 2.1. The spins in Λ_a and Λ_d will form singlets, while Λ_b and Λ_c still remain in the Néel phase and remain the important degrees of freedom.

So now we want to directly study an effective model for only the sites in sublattices Λ_b and Λ_c. Following again the strong coupling limit, the resulting theory will also become a spin model. We write the J_1-J_2 spin model for the effective honeycomb lattice. That is,

$$
H = J_1 \sum_{i=1}^{3} \sum_{\boldsymbol{r} \in \Lambda_b} \vec{S}_{\boldsymbol{r}}^{(b)} \cdot \vec{S}_{\boldsymbol{r}+\boldsymbol{s}_i}^{(c)}
$$
$$
+ J_2 \sum_{i=1}^{3} \left[\sum_{\boldsymbol{r} \in \Lambda_b} \vec{S}_{\boldsymbol{r}}^{(b)} \cdot \vec{S}_{\boldsymbol{r}+\boldsymbol{t}_i}^{(b)} + \sum_{\boldsymbol{r} \in \Lambda_c} \vec{S}_{\boldsymbol{r}}^{(c)} \cdot \vec{S}_{\boldsymbol{r}+\boldsymbol{t}_i}^{(c)} \right]. \tag{2.10}
$$

The J_2 coupling is t^4/U^3 order in the perturbation in Sec. 2.2, and is calculated in Eq. (2.5). However, from the lattice structure in Fig. 2.1, one can see that J_1 is in t^6/U^5 order in the same perturbation theory. Calculating perturbation in two extra orders is a straightforward but tedious task, so we seek an alternative way to compute J_1. We do this by assuming $J_\perp \gg J_\parallel$, and perform the perturbation expansion in

27

$J_\parallel/J_\perp$. Admittedly, because $t_\parallel$ is actually significantly smaller than $t_\perp$ in graphene, this perturbation expansion is rather far from the experimental situation; however, the regime $J_\parallel \gg J_\perp$ offers a tractable limit for studying the phase transition using existing results so seems worthwhile to explore. In the opposite limit of $J_\perp \ll J_\parallel$, qualitatively, the magnetization of Λ_a and Λ_b will be the same although they may be small. Therefore our assumption of $J_\perp \gg J_\parallel$ will be true in regions where $\langle S_z^{(b)} \rangle \gg \langle S_z^{(a)} \rangle$. In Fig. 2.4, this is the case when $E/U > 0.55$. This means that the large $J_\perp$ limit is more valid near the phase transition, and thus suits our purpose of studying the vicinity of the transition point.

The $J_\parallel/J_\perp$ expansion has two contributions to the effective honeycomb lattice in the order of $J_\parallel^2/J_\perp$, one to the J_1 term and the other to the J_2 term. The contributions from the $J_\parallel/J_\perp$ expansion follows from the effective Hamiltonian method (Cohen-Tannoudji et al., 1992),

$$J_1 = \frac{J_\parallel^2}{J_\perp} = \frac{4\,t_\parallel^4}{t_\perp^2} \frac{U - V_\perp - \left(\frac{E^2}{U-V_\perp}\right)}{\left(U - V_\parallel - \left(\frac{V_\perp^2}{U-V_\parallel}\right)\right)^2},$$

$$J_2 = -\frac{J_\parallel^2}{2J_\perp} = -\frac{2\,t_\parallel^4}{t_\perp^2} \frac{U - V_\perp - \left(\frac{E^2}{U-V_\perp}\right)}{\left(U - V_\parallel - \left(\frac{V_\perp^2}{U-V_\parallel}\right)\right)^2}. \tag{2.11}$$

From our assumption that $J_\parallel$ and $J_\perp$ are antiferromagnetic, it follows that the contribution to J_1 is antiferromagnetic and J_2 is ferromagnetic. For a complete description for the $J_1 - J_2$ model in the effective honeycomb lattice up to the desired order, we need to add the J_2 contributions from the t/U expansion and $J_\parallel/J_\perp$ expansion. The

final $J_1 - J_2$ model will be Eq. (2.10) with exchange couplings of

$$J_1 = \frac{4\ t_\parallel^4}{t_\perp^2}\frac{U - V_\perp - \left(\frac{E^2}{U-V_\perp}\right)}{\left(U - V_\parallel - \left(\frac{V_\perp^2}{U-V_\parallel}\right)\right)^2},$$

$$J_2 = \frac{4\ t_\parallel^4}{(U-V_\parallel)^2 - V_\perp^2}\left(\frac{2(U-V_\parallel)\left((U-V_\parallel)^2 + V_\perp^2\right)}{\left((U-V_\parallel)^2 - V_\perp^2\right)^2} - \frac{1}{U}\right)$$

$$- \frac{2\ t_\parallel^4}{t_\perp^2}\frac{U - V_\perp - \left(\frac{E^2}{U-V_\perp}\right)}{\left(U - V_\parallel - \left(\frac{V_\perp^2}{U-V_\parallel}\right)\right)^2}. \tag{2.12}$$

The ground state of the above J_1-J_2 model can only be solved numerically. However, qualitative behaviors can be studied from the E dependence of J_1 and J_2. Directly from Eq. (2.12), one can see that J_1 decreases and J_2 increases as E increases. Since the first term of J_2 in Eq. (2.12) is positive, we always have a window of E where both J_1 and J_2 are positive. Inside that window, the ratio of J_2/J_1 will increase as E increases, until J_1 decreases to 0. We know that for $J_2/J_1 \ll 1$ the ground state will be a Néel state, including when $J_2 < 0$, where J_2 supports the Néel state. However, a positive J_2 starts to frustrate the Néel phase as J_2/J_1 increases. This will eventually destroy the Néel state at a critical value of J_2/J_1, and a phase transition will occur.

Numerically, the J_1-J_2 model in a honeycomb lattice has recently been investigated via a variety of methods (Clark et al., 2011; Albuquerque et al., 2011; Ganesh et al., 2013; Zhu et al., 2013; Gong et al., 2013), and related models have been studied in Pujari et al. (2013) and Lang et al. (2013). These studies all find a transition out of the Néel state to a Kekulé VBS state (or the closely related plaquette state, which has the same pattern on symmetry breaking on the honeycomb lattice). Ganesh et al. (2013), Zhu et al. (2013), and Gong et al. (2013) tune J_2/J_1, and find evidence for an apparent second-order phase transition from Néel state at small J_2/J_1 to VBS state at larger J_2/J_1, where the critical value $J_2/J_1 \sim 0.22$—0.26. The studies can be therefore considered as the numerical analysis of our J_1-J_2 model in the window of E where $J_1, \ J_2 > 0$. Since the critical value of J_2/J_1 in the DMRG study can be always reached in our model through a certain value of E, we may argue that the same phase transition from Néel to VBS happens in the bilayer graphene system as

well, when tuning the electric field. So the J_1-J_2 model in the effective honeycomb lattice not only supports the Néel to VBS phase transition in the bilayer graphene, but also provides indirect evidence that the transition is in the deconfined category.

2.5 Geometric phases

Our analysis so far has examined the potential instability of the Néel phase to a "quantum disordered" phase, which preserves spin rotation invariance. General arguments were made in Read and Sachdev (1990) that any such phase in a model with the symmetry of the honeycomb lattice must have VBS order: these arguments relied on Berry phases of "hedgehog" tunneling events in the Néel order. In Fu et al. (2011) (see also Yao and Lee (2010)), these arguments were recast in terms of geometric phases associated with skyrmion textures, which led to a coupling in the action between the temporal derivative of the VBS order and the skyrmion density in the Néel order. This section will obtain a similar term for the case of the bilayer antiferromagnet. This term will be obtained in a weak coupling model, and we will comment on the relationship to the strong coupling results at the end of the present section.

Since we already know the ground states around the critical point are Néel and VBS states, we write a weak coupling Hamiltonian and later include interaction effects and the electric field as a Néel and VBS mean-field order parameter. The weak coupling Hamiltonian in a bilayer honeycomb lattice is merely a tight-binding model. Using the parameters and operators defined as in Sec. 2.2, this is

$$
H_{\mathrm{w}} = - t_\parallel \sum_{\boldsymbol{r} \in \Lambda_a} \sum_{i=1}^{3} c_{\boldsymbol{r}}^{(a)\dagger} c_{\boldsymbol{r}+\boldsymbol{s}_i}^{(b)} - t_\parallel \sum_{\boldsymbol{r} \in \Lambda_d} \sum_{i=1}^{3} c_{\boldsymbol{r}}^{(d)\dagger} c_{\boldsymbol{r}-\boldsymbol{s}_i}^{(c)}
$$
$$
- t_\perp \sum_{\boldsymbol{r} \in \Lambda_a} c_{\boldsymbol{r}}^{(a)\dagger} c_{\boldsymbol{r}}^{(d)} - t_2 \sum_{\boldsymbol{r} \in \Lambda_b} \sum_{i=1}^{3} c_{\boldsymbol{r}}^{(b)\dagger} c_{\boldsymbol{r}+\boldsymbol{s}_i}^{(c)} + \mathrm{h.c.}. \tag{2.13}
$$

One extra term is added to Eq. (2.1), which is the t_2 term describing the direct hopping between sublattice Λ_b and sublattice Λ_c. Although t_2 is very small compared to $t_\parallel$ and $t_\perp$ in realistic systems as we ignored in the previous calculations, we keep the

t_2 term in the current section to use it as a parameter interpolating between bilayer and monolayer graphene (McCann and Fal'ko, 2006).

The band structure of this Hamiltonian consists of four bands where two of them quadratically touch at the two K points, which we label them as $K_\pm = \pm(0, \frac{4\pi}{3\sqrt{3}})$. At half-filling, the Fermi level is right at the touching points, and the low-energy physics is govern by the $K_\pm$ points of the quadratically touching bands. Also at the $K_\pm$ points, the band gap between the quadratically touching bands and the remaining bands is $t_\perp$. Therefore, by considering energies much smaller than $t_\perp$ near the $K_\pm$ points, we write a low-energy effective theory,

$$H_{\rm w}^{\rm eff} = \sum_{\bf p} \Psi^\dagger({\bf p}) \left[\frac{v^2}{t_\perp} \left(\left(p_x^2 - p_y^2\right) s_x + (2p_x p_y)\, \rho_z s_y \right) + v_2 \left(p_x s_y + p_y \rho_z s_x\right) \right] \Psi({\bf p}),$$

(2.14)

where $v = 3t_\parallel/2$ and $v_2 = 3t_2/2$. Here, p_x and p_y are the momentum components measured from the $K_\pm$ points, and ρ and s are the Pauli matrices in valley and layer space, respectively. Only sublattices Λ_b and Λ_c remain in the effective theory, and $\Psi({\bf p})$ is a four-component spinor with each component from two sublattices and two $K_\pm$ points. Λ_b and Λ_c also form a honeycomb lattice and we again see that the effective low-energy theory of a bilayer honeycomb lattice lives in a single honeycomb lattice.

Now, we impose that the system is in the Néel phase. In the ordered state, we may choose the Néel order parameter to be in z-direction, and we can simply add $H_{N_z} = m\sigma_z s_z$ to the effective Hamiltonian, where σ are the spin Pauli matrices. The Néel order opens up a gap of size $2m$ at the $K_\pm$ points. $H_0 = H_{\rm w}^{\rm eff} + H_{N_z}$ is the final effective Hamiltonian for the system in the Néel phase and will serve as the unperturbed Hamiltonian.

As the system approaches the critical point, the Néel order and VBS order fluctuations become larger. Therefore, as in Fu et al. (2011), both fluctuations should be taken into account for a proper study of the system near the critical point. We treat these two as a perturbation. Let us write the fluctuating Néel order parameter as $\vec{m} = m(n_x, n_y, 1)$ and the complex VBS order parameter as $V = V_x + iV_y$. The

Hamiltonian of n_x, n_y is $H_{N_{xy}} = m s_z (n_x \sigma_x + n_y \sigma_y)$. Recalling that the Kekulé type of bond order can be written as a modulation on the tight binding hopping parameter, (Hou et al., 2007, 2010)

$$H_V = -\sum_{\boldsymbol{r} \in \Lambda_b} \sum_{i=1}^{3} \delta t_{\boldsymbol{r},i} \, c_{\boldsymbol{r}}^{(b)\dagger} c_{\boldsymbol{r}+\boldsymbol{s}_i}^{(c)} + \text{h.c.}, \tag{2.15}$$

$$\delta t_{\boldsymbol{r},i} = V \, \mathrm{e}^{\mathrm{i}\mathbf{K}_+ \cdot \boldsymbol{s}_i} \mathrm{e}^{\mathrm{i}(\mathbf{K}_+ - \mathbf{K}_-)\cdot \boldsymbol{r}}/3 + \text{c.c.},$$

we find $H_V = -s_x (V_x \rho_x - V_y \rho_y)$ as the Hamiltonian for the VBS order parameter. So the perturbation H_1 is $H_1 = H_{N_{xy}} + H_V$ and now we can write the full Hamiltonian,

$$
\begin{aligned}
H =& H_0 + H_1 \\
=& \left(\frac{v^2}{t_\perp} \left(\left(p_x^2 - p_y^2 \right) s_x + (2 p_x p_y) \rho_z s_y \right) + v_2 \left(p_x s_y + p_y \rho_z s_x \right) + m \sigma_z s_z \right) \\
& + \left(m \left(n_x \sigma_x + n_y \sigma_y \right) s_z - \left(V_x \rho_x - V_y \rho_y \right) s_x \right).
\end{aligned}
\tag{2.16}
$$

Note that the terms proportional to the antiferromagnetic order, m, anti-commute with all the terms in Eq. (2.14), indicating they will open up a gap in the electronic spectrum. On the other hand, the terms proportional to the VBS order anti-commute only with the v_2 term, but not with the $v^2/t_\perp$ term, indicating that VBS order alone does not open a gap in the purely quadratic-band-touching spectrum.

Writing in a specific basis, $\Psi^\dagger(\boldsymbol{p}) = (c_{\boldsymbol{p}+}^{(b)\dagger}, c_{\boldsymbol{p}-}^{(b)\dagger}, c_{\boldsymbol{p}+}^{(c)\dagger}, c_{\boldsymbol{p}-}^{(c)\dagger})$, where $\pm$ corresponds to the $K_\pm$ points the momentum is measured from

$$
H =
\begin{pmatrix}
\vec{m} \cdot \vec{\sigma} & 0 & -\frac{v^2}{t_\perp}\pi^2 + v_2 \pi^\dagger & -V_x - \mathrm{i}V_y \\
0 & \vec{m} \cdot \vec{\sigma} & -V_x + \mathrm{i}V_y & -\frac{v^2}{t_\perp}\pi^{\dagger 2} - v_2 \pi \\
-\frac{v^2}{t_\perp}\pi^{\dagger 2} + v_2 \pi & -V_x - \mathrm{i}V_y & -\vec{m} \cdot \vec{\sigma} & 0 \\
-V_x + \mathrm{i}V_y & -\frac{v^2}{t_\perp}\pi^2 - v_2 \pi^\dagger & 0 & -\vec{m} \cdot \vec{\sigma}
\end{pmatrix}.
\tag{2.17}
$$

Here, $\pi = \mathrm{i}p_x + p_y$ is defined for notational convenience. Now, it is more apparent that $v_2 = 0$ gives the Hamiltonian for bilayer graphene and $v = 0$ gives that of the monolayer graphene with opposite chirality. Therefore, we may tune v_2/v to interpolate between monolayer and bilayer graphene.

Note that the electric field E in Eq. (2.1) is not included in this final form of the Hamiltonian. However, it is encoded in the order parameters as we have seen in the previous sections how electric field tunes the Néel to VBS transition. The electric field has other effects as well, as changing the energy gap of the VBS phase for example, but this will have only quantitative effects in the calculation. The result of the calculation with explicit electric field will be presented in the following section.

From Eq. (2.16), we integrate out the fermions to get an effective theory for the fluctuating order parameters. The coupling between the Néel and VBS order parameters appears at fourth order of one-loop expansion. For notational simplicity, we follow Fu et al. (2011) and combine the four real order parameters to a multi-component bosonic field, $\mathcal{A}^\mu(x, y, \tau) = (V_x/m, V_y/m, n_x, n_y)$. $\mu = 0, 1, 2, 3$ label the different fields in $\mathcal{A}^\mu$ and are not Lorentz indices. In momentum space, the four point couplings between the bosonic fields are,

$$S_1 = \sum_{\mu,\nu,\lambda,\delta} \int \prod_{i=1}^{3} dp_i K_{p_1 p_2 p_3}^{\mu\nu\lambda;\delta} \mathcal{A}^\mu(p_1) \mathcal{A}^\nu(p_2) \mathcal{A}^\lambda(p_3)$$
$$\times \mathcal{A}^\delta(-p_1 - p_2 - p_3). \tag{2.18}$$

Among this bosonic coupling, we are most interested in the topological term,

$$S_{\text{top}} = \mathrm{i} \int dx dy d\tau \left(K j_\tau^N j_\tau^V + K' j_x^N j_x^V + K' j_y^N j_y^V \right), \tag{2.19}$$

which is the coupling term between the skyrmion current j_α^N and VBS current j_β^V:

$$j_\alpha^N \equiv \epsilon_{\alpha\beta\gamma} \epsilon_{abc} n^a \partial_\beta n^b \partial_\gamma n^c,$$
$$j_\beta^V \equiv V_x \partial_\beta V_y - V_y \partial_\beta V_x. \tag{2.20}$$

This topological term is of interest to us because it provides an argument that the system is in VBS phase in the disordered side; as mentioned in the beginning of this section, this is analogous to arguments in Read and Sachdev (1990) and Fu et al. (2011).

As explained in detail in Fu et al. (2011), we can extract the couplings K and K'

from $K_{p_1 p_2 p_3}^{\mu\nu\lambda;\delta}$ in Eq. (2.18). The final expression for K is as follows:

$$
\begin{aligned}
8K = {}& K_{\tau xy}^{234;1} + K_{\tau yx}^{243;1} + K_{xy\tau}^{342;1} + K_{x\tau y}^{324;1} + K_{y\tau x}^{423;1} + K_{yx\tau}^{432;1} \\
& - \left(K_{\tau xy}^{243;1} + K_{\tau yx}^{234;1} + K_{xy\tau}^{432;1} + K_{x\tau y}^{423;1} + K_{y\tau x}^{324;1} + K_{yx\tau}^{342;1} \right) \\
& - \left(K_{\tau xy}^{134;2} + K_{\tau yx}^{143;2} + K_{xy\tau}^{341;2} + K_{x\tau y}^{314;2} + K_{y\tau x}^{413;2} + K_{yx\tau}^{431;2} \right) \\
& + K_{\tau xy}^{143;2} + K_{\tau yx}^{134;2} + K_{xy\tau}^{431;2} + K_{x\tau y}^{413;2} + K_{y\tau x}^{314;2} + K_{yx\tau}^{341;2},
\end{aligned}
\tag{2.21}
$$

where K' can also be written in a similar way. Here, $K_{\alpha\beta\gamma}^{\mu\nu\lambda;\delta}$ are defined as the coefficient of the term linear in $p_1 p_2 p_3$:

$$
K_{p_1 p_2 p_3}^{\mu\nu\lambda;\delta} = \cdots + K_{\alpha\beta\gamma}^{\mu\nu\lambda;\delta} p_1^\alpha p_2^\beta p_3^\gamma + \cdots .
\tag{2.22}
$$

The lowest order contribution to S_1 arises from the one-loop expansion, when we integrate out the fermion loop. Therefore, the calculation of $K_{\alpha\beta\gamma}^{\mu\nu\lambda;\delta}$ eventually boils down to calculating box diagrams, as in Fig. 2.5. Note that in Eq. (2.16), the vertex functions between bosonic fields and fermions have no momentum dependence and therefore the p_1^α, p_2^β, p_3^γ dependence comes from the propagator.

After evaluating a number of diagrams and substituting $K_{\alpha\beta\gamma}^{\mu\nu\lambda;\delta}$'s to Eq. (2.21) and its K' analog, we obtain the topological couplings K and K' of the system. First, we consider the bilayer limit of $v_2/v = 0$. The integral expressions for K and K' are,

$$
\begin{aligned}
K = {}& \frac{1}{8\pi^3} \int dk_0 dk_x dk_y \frac{8m^5 t_\perp^6 v^4 \left(k_x^2 + k_y^2 \right)}{\left((k_0^2 + m^2) t_\perp^2 + (k_x^2 + k_y^2)^2 v^4 \right)^4}, \\
K' = {}& \frac{1}{8\pi^3} \int dk_0 dk_x dk_y \frac{4m^5 t_\perp^6 v^4 \left(3(k_x^2 - k_y^2)(k_0^2 + m^2) t_\perp^2 - (k_x^2 + k_y^2)^2 (13 k_x^2 + 3 k_y^2) v^4 \right)}{\left((k_0^2 + m^2) t_\perp^2 + (k_x^2 + k_y^2)^2 v^4 \right)^5} \\
= {}& \frac{1}{8\pi^3} \int dk_0 dk_x dk_y \frac{4m^5 t_\perp^6 v^4 \left(3(-k_x^2 + k_y^2)(k_0^2 + m^2) t_\perp^2 - (k_x^2 + k_y^2)^2 (3 k_x^2 + 13 k_y^2) v^4 \right)}{\left((k_0^2 + m^2) t_\perp^2 + (k_x^2 + k_y^2)^2 v^4 \right)^5}.
\end{aligned}
\tag{2.23}
$$

The first expression for K' is the coupling of $j_x^N j_x^V$ and the second is of $j_y^N j_y^V$. They map to each other by the transformation $k_x \leftrightarrow k_y$, which gives the same value when integrated on a region which has $k_x \leftrightarrow k_y$ symmetry as well. We can obtain the K and K' of the effective theory by integrating k_x and k_y in the whole space (Abanov
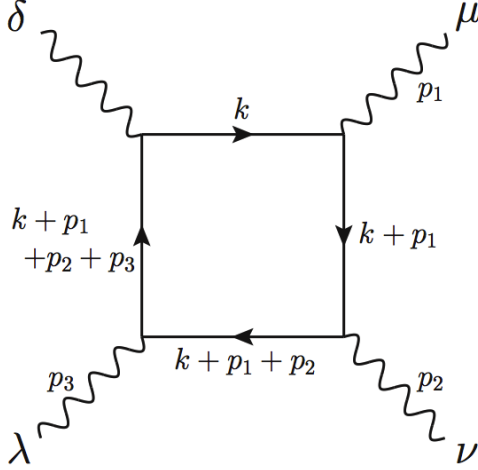
Figure 2.5: The box diagram needed for the calculation of K and K'. The $p_1^\alpha p_2^\beta p_3^\gamma$ coefficient of this box diagram gives $K^{\mu\nu\lambda;\delta}_{\alpha\beta\gamma}$, which K, K' consist of. The exact relation between K and $K^{\mu\nu\lambda;\delta}_{\alpha\beta\gamma}$ is given in Eq. (2.21). Note that every momentum dependence comes from the propagator.

and Wiegmann, 2000). In zero temperature, performing the k_0, k_x, and k_y integral gives $K = -1/16\pi$ and $K' = 1/16\pi$. This is a quantized value that does not depend on microscopic parameters m, $t_\perp$, or v.

Next, we consider the monolayer limit of $v_2/v \gg 1$. This can be integrated analytically and gives $K = K' = 3/32\pi$. They are quantized as well as in the bilayer limit, and the values are consistent with the result from Senthil and Fisher (2006). We also compute K and K' as a function of v_2/v and observe how it changes in the intermediate regime of monolayer and bilayer. The result in Fig. 2.6 shows the aforementioned limiting values of $K = K' = 3/32\pi$ for monolayer and $K = -K' = -1/16\pi$ for bilayer, and a continuous interpolation in-between. K and K' of the intermediate regime does not remain quantized, and thus depends on the parameters of the theory. Through a number of numerical calculations, we observe that the intermediate values at a given v_2/v depend on a single parameter $m/t_\perp$. Starting from the bilayer ($v_2/v = 0$), the convergence to the single layer limit occurs more
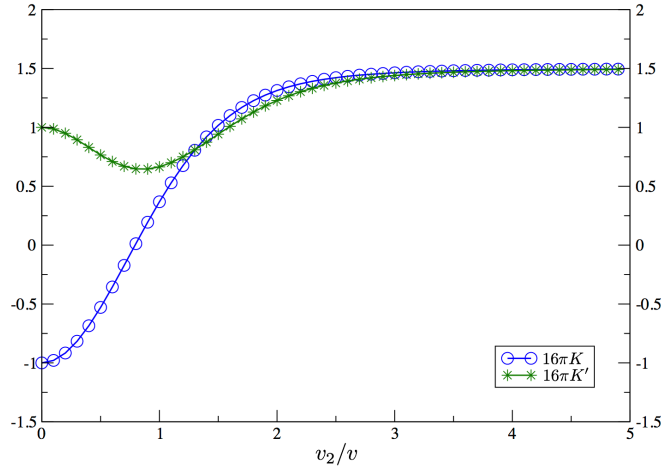
Figure 2.6: The topological couplings K and K' as a function of v_2/v. We assume $t_\parallel = t_\perp = m$, and the y-axis is in the unit of $1/16\pi$. In the bilayer limit of $v_2/v = 0$, the couplings are $K = -1/16\pi$ and $K' = 1/16\pi$. Both K and K' approaches $3/32\pi$ in the monolayer limit of $v_2/v \gg 0$.

rapidly for smaller values of $m/t_\perp$.

The presence of these non-zero terms supports the proposal that the general structure of the coupling between the Néel and VBS orders is the same as that in the single layer honeycomb lattice. But the values of the geometric phases differ in the weak coupling theory, although we expect them to coincide in the strong coupling theory (by the arguments of Read and Sachdev (1990)). This difference suggests that the weak coupling analysis points to a first-order Néel-VBS transition, while deconfined criticality is preferred at strong coupling.

2.6 Geometric phases in electric field

We revisit the geometric phase calculation in Sec. 2.5 including the electric field to the Hamiltonian. As in Eq. (2.26), electric field couples to the layer space as an

extra $-Es_z$ term. The modified Hamiltonian is,

$$H = \left(\frac{v^2}{t_\perp} \left(\left(p_x^2 - p_y^2 \right) s_x + \left(2 p_x p_y \right) \rho_z s_y \right) + v_2 \left(p_x s_y + p_y \rho_z s_x \right) \right.$$

$$\left. + m \sigma_z s_z \right) + \left(m \left(n_x \sigma_x + n_y \sigma_y \right) s_z - \left(V_x \rho_x - V_y \rho_y \right) s_x \right) - E s_z. \tag{2.24}$$

The details of the calculation are the same as in Sec. 2.5, where the only difference comes from the new Hamiltonian. The couplings K and K' as a function of v_2/v in the presence of electric fields $E = 0.3m$ and $E = 0.4m$ are shown in Fig. 2.7(a), together with the $E = 0$ case already in Fig. 2.6.

K and K' in electric field both show qualitatively similar behavior to the zero-electric-field situation. However, one should notice that the quantitative values are different not only in the intermediate region, but also at the $v_2/v = 0$ and $v_2/v \gg 0$ limits, where we found that the values at $E = 0$ were quantized. The reason for this deviation is that the coupling matrices of the Néel order parameter $(\sigma_i s_z)$ and of the electric field (s_z) commute, and as a result, the Néel state and the electric field induce gapped states that can mix with each other. Although they have similar dispersion in the weak coupling theory, the two states have very different topological features. For example, the gapped state by electric field does not have topological defects as skyrmions, whose geometric phase leads to nonzero K and K' coupling terms. Explicit calculation also confirms $K = K' = 0$ when there is only electric field and no Néel order parameter in the theory.

We also calculate K and K' in the bilayer $(v_2/v = 0)$ and monolayer $(v_2/v \gg 1)$ limits for various values of E. In Fig. 2.7(b), we see that K' of the bilayer limit increases as electric field increases up to $E/m = 1$. $E = m$ is the fine tuned value of E where the energy gap vanishes. Both K and K' diverge at this gapless point. Also, the ratios of K and K' can be written in a simple formula. Let us write $K(v_2/v)$ and $K'(v_2/v)$ as a function of v_2/v for notational convenience. First, the $K(0)$ and $K'(0)$ are related as,

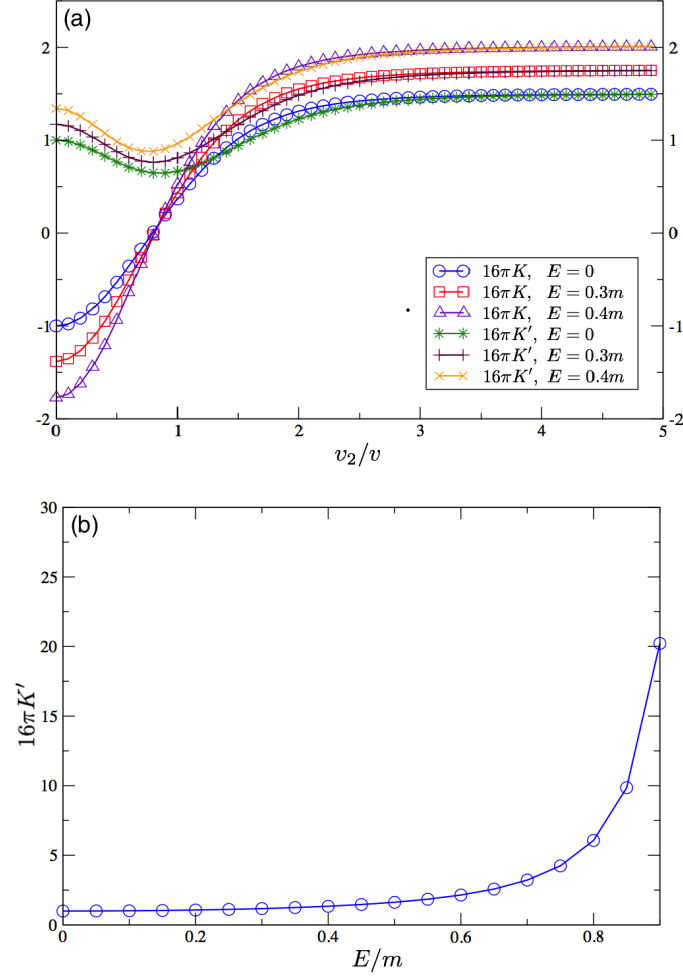$$\frac{K(0)}{K'(0)} = -1 - 2 \left(\frac{E}{m} \right)^2, \tag{2.25}$$

Figure 2.7: (a) A plot of K and K' with different values of electric field, as a function of v_2/v. We assume $t_\parallel = t_\perp = m$ and thus the graph with $E = 0$ is identical to Fig. 2.6. With the nonzero electric field values, the graph shows similar behavior but differences in the exact values. (b) The value of K' in the bilayer limit ($v_2/v = 0$) as we increase the electric field. The value monotonically increases as we increase the electric field. The gap closes at $E = m$ and K', K diverges at this point.

when $E < m$. This gives the correct limiting value for the $E = 0$ case, where $K(0) = -K'(0) = -1/16\pi$. Also, as one can check roughly in Fig. 2.7(a), $K(\infty) = K'(\infty) = 1.5K'(0)$ strictly holds as in the $E = 0$ limit.

2.7 Zero mode in VBS vortex

Another approach to the theory of deconfined criticality is via the structure of vortices in the VBS order parameter. Levin and Senthil (2004) presented general arguments that each such vortex must carry spin $S = 1/2$. In some case, this fact is already apparent by the presence of zero modes in a weak coupling theory of the VBS state: this is the case in monolayer graphene (Hou et al., 2007, 2010). We present a corresponding computation for the bilayer case, and do not find such zero modes. We view this as a feature of the weak coupling approach, rather than the inapplicability of the general strong coupling arguments of Read and Sachdev (1990).

We start in the deep VBS phase and may ignore the Néel order for now. Therefore we adapt the Hamiltonian (2.16) with $m = 0$. In this section we return to $t_2 = 0$, and set the Fermi velocity $v = 3t_{\parallel}/2$ equal to one. VBS order parameter, $V(\boldsymbol{r}) = V_x(\boldsymbol{r}) + iV_y(\boldsymbol{r})$, now has a nonzero expectation value, and let us allow it to fluctuate over space. We will assume the fluctuation is in a much longer length scale than the lattice constant, which is set to 1, so we can treat the order parameter as a constant during Fourier transform. Moreover, we include the electric field explicitly as this will open up an energy gap of the system. The Hamiltonian in the VBS phase is,

$$
\begin{aligned}
H = & \frac{1}{t_{\perp}} \left(p_x^2 - p_y^2 \right) s_x + \frac{1}{t_{\perp}} \left(2p_x p_y \right) \rho_z s_y \\
& - \left(V_x(\boldsymbol{r}) \rho_x - V_y(\boldsymbol{r}) \rho_y \right) s_x - E s_z,
\end{aligned}
\tag{2.26}
$$

where ρ and s are the Pauli matrices in valley and layer space, respectively. Note that in the bilayer graphene, the Kekulé VBS order does not open up a gap but create nodal lines which form a circle in the Brillouin zone. The nodal line is protected by the layer symmetry of the system. Discussing zero modes in a gapless system is meaningless, however, the transition is at a nonzero electric field. Electric field

couples differently with the density of the electrons in different layers and breaks the layer symmetry. This opens up a gap at the nodal line and it is now legitimate to discuss zero modes of the system.

As in Sec. 2.5, choosing a specific basis, $\Psi^\dagger(\boldsymbol{p}) = (c_{\boldsymbol{p}+}^{(b)\dagger}, c_{\boldsymbol{p}-}^{(b)\dagger}, c_{\boldsymbol{p}+}^{(c)\dagger}, c_{\boldsymbol{p}-}^{(c)\dagger})$, we can represent the Hamiltonian as a 4×4 matrix:

$$
H = \begin{pmatrix}
-E & 0 & -\frac{1}{t_\perp}\pi^2 & -V(\boldsymbol{r}) \\
0 & -E & -\overline{V}(\boldsymbol{r}) & -\frac{1}{t_\perp}\pi^{\dagger 2} \\
-\frac{1}{t_\perp}\pi^{\dagger 2} & -V(\boldsymbol{r}) & E & 0 \\
-\overline{V}(\boldsymbol{r}) & -\frac{1}{t_\perp}\pi^2 & 0 & E
\end{pmatrix}.
\tag{2.27}
$$

Changing to the real basis, $\Psi^\dagger(\boldsymbol{r}) = (u_b^\dagger(\boldsymbol{r}), v_b^\dagger(\boldsymbol{r}), u_c^\dagger(\boldsymbol{r}), v_c^\dagger(\boldsymbol{r}))$, where for example, $u_b(\boldsymbol{r}) = \frac{1}{\sqrt{N}}\sum_{\boldsymbol{p}} e^{i\boldsymbol{p}\cdot\boldsymbol{r}} b_{\boldsymbol{p}+}$ and $v_b(\boldsymbol{r}) = \frac{1}{\sqrt{N}}\sum_{\boldsymbol{p}} e^{i\boldsymbol{p}\cdot\boldsymbol{r}} b_{\boldsymbol{p}-}$,

$$
H = -\frac{1}{t_\perp} \begin{pmatrix}
E & 0 & 4\partial_z^2 & V(\boldsymbol{r}) \\
0 & E & \overline{V}(\boldsymbol{r}) & 4\partial_{\bar{z}}^2 \\
4\partial_{\bar{z}}^2 & V(\boldsymbol{r}) & -E & 0 \\
\overline{V}(\boldsymbol{r}) & 4\partial_z^2 & 0 & -E
\end{pmatrix}.
\tag{2.28}
$$

Here, we included $t_\perp$ into the definition of $V(\boldsymbol{r})$ and E for notational convenience and used a complex coordinate $z = x + iy$ for $2\partial_z = e^{-i\theta}(\partial_r - \frac{i}{r}\partial_\theta)$.

Now we assume that the VBS order parameter contains a vortex, $V(\boldsymbol{r}) = V_0(r)e^{i\theta}$. Jackiw and Rossi (1981) provides an analytical method of obtaining the zero modes when the fermions are Dirac-like. They count the number of zero modes by matching the two asymptotic behaviors of the solutions of $H\Psi(\boldsymbol{r}) = 0$. The quadratic dispersion of fermions can be easily implemented into this scheme, however, including the electric field ruins the argument and we cannot follow the same step. Alternatively, we have solved the problem numerically. We consider a bilayer honeycomb lattice with 3600 sites with the corresponding lattice Hamiltonian (2.26), and introduce a vortex at the center of the lattice. Open boundary condition is imposed to deal with the vortex without including any Dirac strings. Introducing a vortex and anti-vortex pair will also resolve the issue, but it will also effectively decrease

the system size. With the open boundary condition, we turn on a small potential at the boundary to eliminate zero-energy states arising from boundary effects. We then numerically diagonalize the system and search for zero-energy eigenvalues. We also check the eigenfunctions of the states while moving the vortex center around to confirm whether the wavefunctions are actually localized at the vortex. The result clearly showed no zero modes in the presence of a vortex. As we noted earlier, we believe this result is a feature of the weak coupling method, and that the needed zero mode will appear in the strong coupling limit as argued in Levin and Senthil (2004).

We also mention previous reports about zero modes in vortices of bilayer graphene (Moon, 2012; Lu and Herbut, 2012). In these works, the authors claim there are two zero modes for a single vortex of valley ferromagnet order. Note that this order breaks time reversal symmetry and is different from the Kekulé VBS phase we have considered above. In the notation of Eq. (2.26), the valley ferromagnet order will be written as $(V_x\rho_y + V_y\rho_x)s_y$, which anti-commutes with the kinetic energy terms. Lu and Herbut (2012) concentrates in regions near the vortex and uses the method of Jackiw and Rossi (1981) in momentum space. However, this is potentially danger-ous because, as mentioned before, the number of zero modes is determined by the matching of the asymptotic behavior of near-vortex and far-vortex regions. Indeed, without the matching procedure, and only looking in the near-vortex region one can find an infinite number of zero modes. However, by numerically diagonalizing the lattice Hamiltonian as above, we indeed find two zero modes for their system with valley ferromagnet order.

2.8   Conclusions

This chapter has examined the strong coupling limit of an extended Hubbard model appropriate for undoped bilayer graphene. The results of our analyses are that the application of a transverse electric field does indeed destabilize the Néel insulator, and that resulting "quantum disordered" state is likely to have VBS order, which breaks the space group symmetry of the lattice. These results are in accord with

the weak coupling analysis (Kharitonov, 2012b), and our strong coupling arguments indicate that the Néel-VBS quantum phase transition in bilayer graphene can be in the deconfined universality class (Senthil et al., 2004a,b).

On the experimental side, there is now good evidence for the Néel state in bilayer graphene (Maher et al., 2013; Freitag et al., 2013), and also for a quantum transition out of this state upon application of a transverse electric field (Weitz et al., 2010; Freitag et al., 2012; Velasco et al., 2012). It would be of great interest to devise experiments to measure the translational symmetry breaking associated with the VBS order. The transition to the VBS state should exhibit quantum-critical scaling, and this may be detected by a careful study of the temperature dependence of the influence of the transverse electric field on conductance across the transition, and looking for a "quantum-critical fan" (Sachdev and Keimer, 2011) in the electric-field/temperature plane.

For experimental applications, the fundamental new idea that a "deconfined-critical" perspective brings is that the transition out of the Néel state occurs as a consequence of condensation of low-energy skyrmions in the Néel order (Senthil et al., 2004a,b); so such low-energy skyrmions should be present in bilayer graphene near the transition. In the presence of ferromagnetic order, a crucial feature of skyrmions in the quantum Hall regime is that they carry electric charge (Lee and Kane, 1990; Sondhi et al., 1993). In the present bilayer case, each layer has intra-layer ferromagnetism in the Néel state, with opposite orientation in the two layers, and so we can expect that the layers carry opposite charges in the presence of a skyrmion. With the application of an electric field, the layer-exchange symmetry is broken, and then a skyrmion current will carry a net electrical current. It is notable that the experiments show enhanced conductivity in the region of the transition, (Weitz et al., 2010) and this could be explained by the presence of low-energy skyrmions in the deconfined-critical theory. In our present strong-coupling analysis, the orbital magnetic field effects have been suppressed, and so we have not accounted for the electrical nature of the skyrmions: an extension of our analysis to include the physics of Landau levels is required, and is being undertaken. On the experimental side, the opposite layers

charges carried by the skyrmion could be studied by driving currents in opposite directions in the two layers. Also, optical experiments can detect the spin-chirality fluctuations (Lee and Nagaosa, 1992) linked to the collective gauge excitations of deconfined criticality; however, it will be necessary for the light to couple selectively to one layer (*i.e.*, one sublattice of the antiferromagnet).

Chapter 3

Wess-Zumino-Witten terms in graphene Landau levels

3.1 Introduction

A number of recent experimental (Weitz et al., 2010; Freitag et al., 2012; Velasco et al., 2012; Young et al., 2012; Maher et al., 2013; Freitag et al., 2013; Young et al., 2014) and theoretical (Herbut, 2007; Jung and MacDonald, 2009; Nandkishore and Levitov, 2010; Cvetkovic et al., 2012; Zhang et al., 2012; Kharitonov, 2012a,b,c,d; Lee and Sachdev, 2014; Wu et al., 2014; Dhochak et al., 2015) works have focused on the presence of antiferromagnetism in neutral monolayer and bilayer graphene in an applied magnetic field. It has also been argued that a nonmagnetic state with lattice symmetry breaking in the Kekulé valence bond solid (VBS) pattern (see Fig. 3.1) is proximate to the antiferromagnetic (AF) state (Kharitonov, 2012a,b; Lee and Sachdev, 2014; Wu et al., 2014). Bilayer graphene offers a particularly attractive area for studying the interplay between the AF and VBS order because it may be possible to tune between them by applying a transverse electric field (Weitz et al., 2010; Kharitonov, 2012b; Lee and Sachdev, 2014).

The presence of the competing AF and VBS orders sets up the possibility (Lee and Sachdev, 2014) of novel quantum criticality between these orders, similar to

that found in insulating quantum spin models (Read and Sachdev, 1990; Senthil et al., 2004a,b; Clark et al., 2011; Albuquerque et al., 2011; Ganesh et al., 2013; Zhu et al., 2013; Block et al., 2013; Gong et al., 2013; Pujari et al., 2013; Lang et al., 2013). However, these quantum spin models apply in the limit of very large on-site Coulomb repulsion between the electrons, and this is not the appropriate parameter regime for graphene. Here we examine a complementary limit of large magnetic field and moderate interactions, so that it is permissible to project onto an effective Hamiltonian acting only on the zero energy Landau levels. Such a limit has been widely used with considerable success in describing the properties of graphene. (Note, however, that we are still in the regime where the cyclotron gap is still smaller than the tight-binding hopping parameters, with magnetic fields smaller than 10 T.) Our main new result is that the Landau level projected effective action for the AF and VBS orders has a topological Wess-Zumino-Witten (WZW) term (Wess and Zumino, 1971; Witten, 1983; Abanov and Wiegmann, 2000) for both the monolayer and bilayer cases.

The WZW term has a quantized coefficient, and it computes a Berry phase linking together spatial and temporal textures in the AF and VBS orders. It can be viewed as a higher dimensional generalization of the Berry phase of a single spin S degree of freedom, which is equal to S times the area enclosed by the spin worldline on the unit sphere. Similarly, the WZW term here measures the area on the surface of the sphere in the five-dimensional AF and VBS order parameter space. The presence of this term implies (Tanaka and Hu, 2005; Senthil and Fisher, 2006; Grover and Senthil, 2008) that the field theories of deconfined criticality (Senthil et al., 2004a,b) apply to graphene. Such theories describe the quantum phase transition not in the conventional Landau terms of fluctuating order parameters, but using fractionalized degrees of freedom coupled to emergent gauge fields. We will also discuss experimental implications of these results.
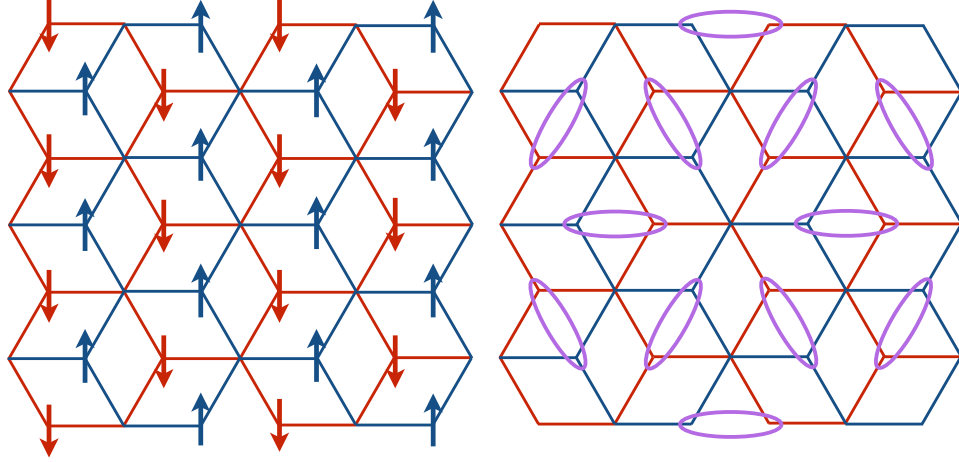
Figure 3.1: AF (left) and Kekulé VBS states of bilayer graphene. The blue (red) lines indicate the honeycomb lattice of the top (bottom) layer. The ellipses in the VBS state denote the links between the top and bottom layers which are equivalently distorted with respect to the parent lattice.

3.2   Model and results

We begin by directly stating the Hamiltonian of the low energy graphene bands (see, *e.g.*, Kharitonov (2012d), Lee and Sachdev (2014) for details)

$$H = v \begin{pmatrix} 0 & a^q \\ a^{\dagger q} & 0 \end{pmatrix}, \tag{3.1}$$

where v is a Fermi velocity, $a = p_x - ip_y - (e/c)(A_x - iA_y)$ with (p_x, p_y) the electron momentum, (A_x, A_y) is the vector potential of the applied magnetic field, the matrix acts on the graphene sublattice index, and $q = 1$ for monolayer graphene, while $q = 2$ for the bilayer case. For bilayers, the sublattice index coincides with the layer index. For both monolayers and bilayers, there is an additional twofold valley degeneracy, along with the usual twofold spin degeneracy (in the absence of a Zeeman coupling).

The a, $a^\dagger$ obey commutation relations proportional to those of the ladder operators of a harmonic oscillator, and so it is easy to diagonalize H. In this manner we obtain q zero energy Landau levels, which are spanned by the orthonormal eigenfunctions $\psi_\ell(\boldsymbol{r})$, where $\ell = 1, \ldots, qN_\Phi$, with N_Φ the number of flux quanta. So we write the

electron annihilation field operator projected to the zero energy Landau levels as

$$\Psi(\boldsymbol{r}) = \sum_{\ell=1}^{qN_\Phi} \psi_\ell(\boldsymbol{r}) c_\ell, \tag{3.2}$$

where c_ℓ is canonical fermion annihilation operator. In the zero energy Landau levels, the valley, sublattice, and layer indices all coincide; henceforth we will refer to this as a valley index, and it can take two values. The fermion operators also carry a spin index with two possible values, and we do not explicitly display the spin or valley indices.

We now introduce Pauli matrices $\sigma^{x,y,z}$ which acts on the spin space, and a second set $\rho^{x,y,z}$ which act on the valley space (here we follow the conventions of Lee and Sachdev (2014)). In terms of these matrices, the three-component AF order is measured by $(\rho^z \sigma^x, \rho^z \sigma^y, \rho^z \sigma^z)$ while the two-component VBS order parameter is (ρ^x, ρ^y).

It is convenient to write the above matrices as

$$\Gamma_1 = \rho^z \sigma^x \ , \ \Gamma_2 = \rho^z \sigma^y \ , \ \Gamma_3 = \rho^z \sigma^z \ , \ \Gamma_4 = \rho^x \ , \ \Gamma_5 = \rho^y$$

and to notice that the 5 Γ_a matrices anticommute and square to unity; indeed these are the 5 Dirac gamma matrices. Their 10 products $i\Gamma_a\Gamma_b$ ($a \neq b$) realize the Lie algebra of SO(5), and the 15 matrices Γ_a and $i\Gamma_a\Gamma_b$ realize the Lie algebra of SU(4).

Next, we introduce a five-component unit vector $n_a(\boldsymbol{r}, \tau)$, where $\boldsymbol{r} = (x, y)$ are the spatial coordinates and τ is imaginary time, representing the combined spacetime fluctuations of the AF and VBS orders. Then the imaginary time Lagrangian of the electrons projected to the zero energy Landau levels is

$$\mathcal{L} = \sum_{\ell=1}^{qN_\Phi} c_\ell^\dagger \frac{\partial c_\ell}{\partial \tau} - \lambda \int d^2\boldsymbol{r} \, n_a(\boldsymbol{r}, \tau) \, \Psi^\dagger(\boldsymbol{r}, \tau) \Gamma_a \Psi(\boldsymbol{r}, \tau) \,, \tag{3.3}$$

where λ is the coupling of the electrons to the AF and VBS orders, and there is an implicit sum of a over five values, and also over the spin and valley indices. The λ term arises from a decoupling of the electron-electron interactions specified in Kharitonov (2012a), Lee and Sachdev (2014), and Wu et al. (2014).

Now we can state our primary result. We integrate over the the the c_ℓ electrons in $\mathcal{L}$ and obtain an effective action for unit vector $n_a(\boldsymbol{r}, \tau)$. Apart from the usual terms of the O(5) nonlinear sigma model considered in Wu et al. (2014) (and anisotropies due to the Zeeman coupling, electron-electron interactions, and a possible transverse electric field for bilayers), the effective action has a topological WZW term at level q,

$$
\begin{aligned}
\mathcal{S}_{\text{WZW}} &= 2\pi i q \, W[n_a], &\text{(3.4)}\\
W[n_a] &= \frac{3}{8\pi^2} \int_0^1 du \int d^2\boldsymbol{r} d\tau \epsilon_{abcde} n_a \partial_x n_b \partial_y n_c \partial_\tau n_d \partial_u n_e.
\end{aligned}
$$

Here we have introduced the extra coordinate u, and $n_a(\boldsymbol{r}, \tau, u)$ is any function which smoothly extrapolates from the physical $n_a(\boldsymbol{r}, \tau)$ at $u = 1$ to a fixed value (say) $n_a = (1, 0, 0, 0, 0)$ at $u = 0$. The choice of the extrapolation can only change $W[n_a]$ by integers, and so $e^{2\pi i q W}$ is well defined.

In the case of graphene in zero magnetic field and weak interactions, the same WZW term between the Néel and VBS orders is also present (Fu et al., 2011). However, for the experimentally important case of bilayer graphene, there is no such WZW term for the AF and VBS orders at zero field and weak interactions (Moon, 2012; Lee and Sachdev, 2014) (although, E.-G. Moon has noted such a term for the quantum spin Hall order (Moon, 2012)); so, in this case the zero energy Landau level projection is crucial for obtaining the topological coupling.

Such a WZW term has a strong impact in the interplay between the order parameters. As we will review below, it topologically links AF order to defects of the VBS order, and vice versa.

3.3 Derivation

We provide two derivations of Eq. (3.4).

First, pick any three of the five n_a components, say $a = u, v, w$, and set the other two to zero. Then we have unit 3-vector field $\vec{N} = (n_u, n_v, n_w)$. Now consider a static Skyrmion texture in $\vec{N}(\boldsymbol{r})$. Then by a computation parallel to that in Section III.B of Moon et al. (1995) (and its generalization to $q = 2$ (Abanin et al., 2009)), the

Skyrmion acquires a "charge." In the present situation the charge is measured by $i\Gamma_u\Gamma_v\Gamma_w$ and its spatial density is

$$\left\langle \Psi^\dagger(\boldsymbol{r})\, i\Gamma_u\Gamma_v\Gamma_w \Psi(\boldsymbol{r})\right\rangle = \frac{q}{2\pi}\vec{N}\cdot(\partial_x\vec{N}\times\partial_y\vec{N}), \tag{3.5}$$

where the angular brackets represent the expectation value over the occupied states in the zero energy Landau level perturbed by the texture in $\vec{N}$ as in $\mathcal{L}$. (A similar relationship has been noted in monolayer graphene in zero magnetic field from Herbut et al. (2012); however, no such relationship applies to bilayer graphene in zero field.) A detailed derivation of Eq. (3.5) is provided in the next paragraph. Now consider a VBS vortex, *i.e.*, a 2π vortex in (n_4, n_5) applied to $\mathcal{L}$. For a two-component order, the core of the vortex has a singularity, but this can be relieved by orienting n_a in a third direction, say $(\pm 1, 0, 0, 0, 0)$. Now the VBS vortex is equivalent to a half-Skyrmion in $\vec{N} = (n_1, n_4, n_5)$, and after integrating Eq. (3.5) over all space, this vortex has $\langle \sigma^x \rangle = \pm q$. Similarly, vortex cores in the directions $(0, \pm 1, 0, 0, 0)$ and $(0, 0, \pm 1, 0, 0)$ yield $\langle \sigma^y \rangle = \pm q$ and $\langle \sigma^z \rangle = \pm q$. So we reach the important conclusion that the VBS vortex has total spin $S = q/2$, and has an associated $(q+1)$-fold degeneracy. For $q = 1$, note that this is precisely the situation considered in Levin and Senthil (2004) for quantum spin models (see also Hou et al. (2010)). Alternatively, we can examine the fate of $\mathcal{S}_{\mathrm{WZW}}$ in the presence of such VBS vortices: following a computation by Grover and Senthil (Grover and Senthil, 2008), we find that the WZW term reduces to the quantum Berry phase of a single spin with $S = q/2$. From this we conclude that Eq. (3.5) implies Eq. (3.4).

Now we give a detailed derivation of Eq. (3.5). We work in Landau gauge and separate the quantum number l in Eq. (3.2) into n and X, where n is the Landau level index and X is the center of the magnetic oscillator. Recall for monolayer graphene $(q = 1)$ n is 0, and for bilayer graphene $(q = 2)$ n is over 0 and 1. There are N_Φ of X labels, so the total number of states in the zero energy Landau level is qN_Φ.

The spatial wavefunction $\psi_{n,X}(\boldsymbol{r})$ in Eq. (3.2) is:

$$\psi_{n,X}(\boldsymbol{r}) = e^{iXy}\varphi_{n,X}(x), \tag{3.6}$$

where $\varphi_{n,X}(x)$ are the n-th harmonic oscillator eigenfunction:

$$\varphi_{0,X}(x) = \frac{1}{\pi^{1/4}} e^{-(x-X)^2/2},$$

$$\varphi_{1,X}(x) = \frac{\sqrt{2}(x-X)}{\pi^{1/4}} e^{-(x-X)^2/2}. \tag{3.7}$$

Note that we work in the unit where the magnetic length $l_B = 1$. We also set the volume of the system as 1 to avoid volume factors in Fourier transform.

Now we can write the Hamiltonian in $c_{n,X}$ basis.

$$
\begin{aligned}
H &= -\lambda \int d^2\boldsymbol{r}\ n_a(\boldsymbol{r})\Psi^\dagger(\boldsymbol{r})\Gamma_a\Psi(\boldsymbol{r}) \\
&= -\lambda \int d^2\boldsymbol{r}\, d^2\boldsymbol{q}\ e^{-i\boldsymbol{q}\cdot\boldsymbol{r}} n_a(-\boldsymbol{q}) \sum_{n,X,n',X'} c^\dagger_{n,X}\varphi_{n,X}(x)e^{-iXy}\,\Gamma_a\, e^{iX'y}\varphi_{n',X'}(x)c_{n',X'} \\
&= -\lambda \int d^2\boldsymbol{q}\ n_a(-\boldsymbol{q}) \sum_{n,n',X} e^{-iq_x X}c^\dagger_{n,X-q_y/2}\,\Gamma_a\, c_{n',X+q_y/2}F_{n,n'}(\boldsymbol{q}) \tag{3.8}
\end{aligned}
$$

The form factors $F_{n,n'}(\boldsymbol{q})$ are calculated as,

$$
\begin{aligned}
F_{00}(\boldsymbol{q}) &= e^{-q^2/4}, \\
F_{01}(\boldsymbol{q}) &= \frac{(-iq_x - q_y)}{\sqrt{2}}e^{-q^2/4}, \\
F_{10}(\boldsymbol{q}) &= \frac{(-iq_x + q_y)}{\sqrt{2}}e^{-q^2/4}, \\
F_{11}(\boldsymbol{q}) &= (1 - q^2/2)e^{-q^2/4}. \tag{3.9}
\end{aligned}
$$

The difference in Eq. (3.8) between $q = 1$ and $q = 2$ case comes from the summation limit of n and n'.

Let us define the operator $\mathcal{O}_a(\boldsymbol{q})$ to be the last part of Eq. (3.8),

$$\mathcal{O}_a(\boldsymbol{q}) = \sum_{n,n',X} e^{-iq_x X}c^\dagger_{n,X-q_y/2}\,\Gamma_a\, c_{n',X+q_y/2}F_{n,n'}(\boldsymbol{q}). \tag{3.10}$$

We can calculate the commutator of two $\mathcal{O}_a$ operators to the lowest order in momen-

tum. In this derivation, we concentrate on the case of bilayer graphene, $q = 2$.

$$
\begin{aligned}
&[\mathcal{O}_a(\boldsymbol{q}), \mathcal{O}_b(\boldsymbol{k})] \\
&= \sum_{n,n',m,Z} e^{-i(q_x+k_x)Z} e^{i(q_x k_y - q_y k_x)/2} F_{nm}(\boldsymbol{q}) F_{mn'}(\boldsymbol{k}) c^\dagger_{n,Z-(q_y+k_y)/2} \Gamma_a \Gamma_b\, c_{n',Z+(q_y+k_y)/2} \\
&\quad - (\boldsymbol{q} \leftrightarrow \boldsymbol{k}, a \leftrightarrow b) \\
&= \sum_Z e^{-i(q_x+k_x)Z} c^\dagger_{1,Z-(q_y+k_y)/2} \left(\frac{\Gamma_a \Gamma_b + \Gamma_b \Gamma_a}{2} \right) c_{1,Z+(q_y+k_y)/2} \\
&\quad \times \left(2i(k_y q_x - k_x q_y) + \mathcal{O}(\boldsymbol{q}, \boldsymbol{k})^2 \right) \\
&\quad + \sum_{n,Z} e^{-i(q_x+k_x)Z} c^\dagger_{n,Z-(q_y+k_y)/2} \left(\frac{\Gamma_a \Gamma_b - \Gamma_b \Gamma_a}{2} \right) c_{n,Z+(q_y+k_y)/2} \times (2 + \mathcal{O}(\boldsymbol{q}, \boldsymbol{k}))
\end{aligned}
\tag{3.11}
$$

For the 3-vector field $\vec{N}(\boldsymbol{r})$ defined previously, we assume $n_w \to 1$ as $\boldsymbol{r} \to \infty$, i.e., $\vec{N}(\boldsymbol{r} \to \infty) = (0, 0, 1) \equiv \vec{N}_0$. This choice is arbitrary and may be rotated by any $SO(3)$ transformation. If we denote $|GS\rangle$ to be the ground state with $\vec{N}(\boldsymbol{r}) = \vec{N}_0$, the expectation value of $\Psi^\dagger(\boldsymbol{r}) \Gamma_w \Psi(\boldsymbol{r})$ will be,

$$
\langle GS | \Psi^\dagger(\boldsymbol{r}) \Gamma_w \Psi(\boldsymbol{r}) | GS \rangle = \frac{4}{2\pi}.
\tag{3.12}
$$

We impose a Skyrmion texture to the ground state by rotating the spinors by an operator $\mathcal{O}$,

$$
\begin{aligned}
\mathcal{O} &= \sum_{\boldsymbol{r}} \vec{\Omega}(\boldsymbol{r}) \cdot \left(\Psi^\dagger(\boldsymbol{r}) \frac{\vec{\Gamma}}{2} \Psi(\boldsymbol{r}) \right) \\
&= \sum_{\boldsymbol{q}} \frac{\vec{\Omega}(-\boldsymbol{q})}{2} \vec{\mathcal{O}}_N(\boldsymbol{q}),
\end{aligned}
\tag{3.13}
$$

where $\vec{\Omega}(\boldsymbol{r}) = \vec{N}_0 \times \vec{N}(\boldsymbol{r})$, $\vec{\Gamma} = (\Gamma_u, \Gamma_v, \Gamma_w)$, and $\vec{\mathcal{O}}_N = (\mathcal{O}_u, \mathcal{O}_v, \mathcal{O}_w)$. The Skyrmion state is now $e^{-i\mathcal{O}} |GS\rangle$. Let us also define the Fourier transform of the operator $\Psi^\dagger(\boldsymbol{r}) i \Gamma_u \Gamma_v \Gamma_w \Psi(\boldsymbol{r})$ to be $\mathcal{O}_\Gamma(\boldsymbol{k})$.

Now we follow the derivation from Moon et al. (1995).

$$
\begin{aligned}
\langle \mathcal{O}_\Gamma(\boldsymbol{k}) \rangle &= \langle GS | e^{i\mathcal{O}} \mathcal{O}_\Gamma(\boldsymbol{k}) e^{-i\mathcal{O}} | GS \rangle - \langle GS | \mathcal{O}_\Gamma(\boldsymbol{k}) | GS \rangle \\
&= i \langle GS | [\mathcal{O}, \mathcal{O}_\Gamma(\boldsymbol{k})] | GS \rangle - \frac{1}{2} \langle GS | [\mathcal{O}, [\mathcal{O}, \mathcal{O}_\Gamma(\boldsymbol{k})]] | GS \rangle + \cdots
\end{aligned}
\tag{3.14}
$$

The first term vanishes and we ignore the higher order terms in $\mathcal{O}$ since we consider a smooth texture. The derivation boils down to calculating the ground state expectation value of $[\mathcal{O}, [\mathcal{O}, \mathcal{O}_\Gamma(\boldsymbol{k})]]$.

First, we compute $[\mathcal{O}, \mathcal{O}_\Gamma(\boldsymbol{k})]$ using Eq. (3.11).

$$
\begin{aligned}
[\mathcal{O}, \mathcal{O}_\Gamma(\boldsymbol{k})] &= \sum_{\boldsymbol{q}} \frac{\Omega_a(-\boldsymbol{q})}{2} [\mathcal{O}_N^a(\boldsymbol{q}), \mathcal{O}_\Gamma(\boldsymbol{k})] \\
&= \sum_{\boldsymbol{q}} \frac{\Omega_a(-\boldsymbol{q})}{2} \left(-k_y q_x + k_x q_y\right) \epsilon_{acd} \\
&\quad \times \sum_{Z} e^{-i(q_x+k_x)Z} c_{1,Z-(q_y+k_y)/2}^\dagger \Gamma_c \Gamma_d\, c_{1,Z+(q_y+k_y)/2}.
\end{aligned}
\tag{3.15}
$$

$a = u, v, w$ is the vector index and repeated indices are summed implicitly. Since $[\Gamma_a, \Gamma_u \Gamma_v \Gamma_w] = 0$ for all a, we considered only the symmetric term in Eq. (3.11). The anti-symmetric tensor is ordered as $\epsilon_{uvw} = 1$.

Now we calculate $[\mathcal{O}, [\mathcal{O}, \mathcal{O}_\Gamma(\boldsymbol{k})]]$.

$$
\begin{aligned}
[\mathcal{O}, [\mathcal{O}, \mathcal{O}_\Gamma(\boldsymbol{k})]] &= \sum_{\boldsymbol{p}} \frac{\Omega_b(-\boldsymbol{p})}{2} \left[\mathcal{O}_N^b(\boldsymbol{p}), [\mathcal{O}, \mathcal{O}_\Gamma(\boldsymbol{k})]\right] \\
&= \sum_{\boldsymbol{p},\boldsymbol{q}} \frac{\Omega_a(-\boldsymbol{q})\Omega_b(-\boldsymbol{p})}{4} \left(-k_y q_x + k_x q_y\right) \epsilon_{acd} \\
&\quad \times \Bigg[\sum_{n,n',X} e^{-ip_x X} c_{n,X-p_y/2}^\dagger \Gamma_b\, c_{n',X+p_y/2} F_{n,n'}(\boldsymbol{p}), \\
&\qquad\qquad \sum_{Z} e^{-i(q_x+k_x)Z} c_{1,Z-(q_y+k_y)/2}^\dagger \Gamma_c \Gamma_d\, c_{1,Z+(q_y+k_y)/2} \Bigg]
\end{aligned}
\tag{3.16}
$$

We have assumed the ground state is uniform, $\vec{N}(\boldsymbol{r}) = \vec{N}_0$. Therefore, the expectation value of the above expression is nonzero only when $-\boldsymbol{p} = \boldsymbol{q} + \boldsymbol{k}$. When this condition is satisfied, the last commutator simplifies to $\sum_Z c_{1,Z}^\dagger [\Gamma_b, \Gamma_c \Gamma_d] c_{1,Z}$, to the lowest order of

momentum. Also using $\epsilon_{acd}[\Gamma_b, \Gamma_c\Gamma_d] = 4\epsilon_{abc}\Gamma_c$, we obtain the expression for $\langle\mathcal{O}_\Gamma(\boldsymbol{k})\rangle$.

$$
\begin{aligned}
\langle\mathcal{O}_\Gamma(\boldsymbol{k})\rangle &= \sum_{\boldsymbol{q}} \epsilon_{abc}\,(k_y q_x - k_x q_y)\,\frac{\Omega_a(-\boldsymbol{q})\Omega_b(\boldsymbol{q}+\boldsymbol{k})}{2}\sum_Z \langle GS|c_{1,Z}^\dagger\,\Gamma_c\,c_{1,Z}|GS\rangle \\
&= \sum_{\boldsymbol{q}} \epsilon_{ab}\,(k_y q_x - k_x q_y)\,\frac{\Omega_a(-\boldsymbol{q})\Omega_b(\boldsymbol{q}+\boldsymbol{k})}{2}\sum_Z \langle GS|c_{1,Z}^\dagger\,\Gamma_w\,c_{1,Z}|GS\rangle \\
&= \frac{1}{2\pi}\sum_{\boldsymbol{q}} \epsilon_{ab}\,(k_y q_x - k_x q_y)\,\Omega_a(-\boldsymbol{q})\Omega_b(\boldsymbol{q}+\boldsymbol{k}) \\
&= \frac{1}{2\pi}\sum_{\boldsymbol{q}} \epsilon_{ab}\,(-i\boldsymbol{q}\Omega_a(-\boldsymbol{q})) \times (i(\boldsymbol{k}+\boldsymbol{q})\Omega_b(\boldsymbol{q}+\boldsymbol{k})) \cdot \hat{z} \qquad (3.17)
\end{aligned}
$$

The second equality make use of the expectation value being nonzero only when $\Gamma_c = \Gamma_w$ in the defined ground state. The new anti-symmetric tensor has indicies $a, b = u, v$, and $\epsilon_{uv} = 1$. Note that the expectation value is half of Eq. (3.12) since only $n = 1$ contributes in the above equation. We obtain the final result by Fourier transforming back to real space.

$$
\begin{aligned}
\langle\Psi^\dagger(\boldsymbol{r})i\Gamma_u\Gamma_v\Gamma_w\Psi(\boldsymbol{r})\rangle &= \frac{1}{2\pi}\epsilon_{ab}\,(\nabla\Omega_a(\boldsymbol{r}) \times \nabla\Omega_b(\boldsymbol{r})) \cdot \hat{z} \\
&= \frac{2}{2\pi}\vec{N} \cdot \left(\partial_x\vec{N} \times \partial_y\vec{N}\right) \qquad (3.18)
\end{aligned}
$$

This is Eq. (3.5) for $q = 2$. The simpler $q = 1$ case follows from the exactly same procedure.

For a second derivation of the WZW term from Eq. (3.3), we examine a diagrammatic expansion of $\mathcal{L}$. Consider a situation where n_a is polarized near, say, $(0, 0, 0, 0, 1)$. Then, we can write $n_a = (\pi_1, \pi_2, \pi_3, \pi_4, 1)$ where $|\pi_i| \ll 1$ for $i = 1, \ldots, 4$. Then to zeroth order in the π_i, the c_ℓ operators in $\mathcal{L}$ have the Green's function

$$
G = (i\omega + \lambda\Gamma_5)^{-1} \qquad (3.19)
$$

where ω is the frequency of the electron propagator. We now proceed to integrate out the electrons, and derive an effective action for the π_i. At fourth order in the π_i, we consider the box diagram in Fig. 3.2; this can be evaluated by methods similar to those Sec. 2.5, but with the G above, and the vertices contributing the factors implied by Eq. (3.3).
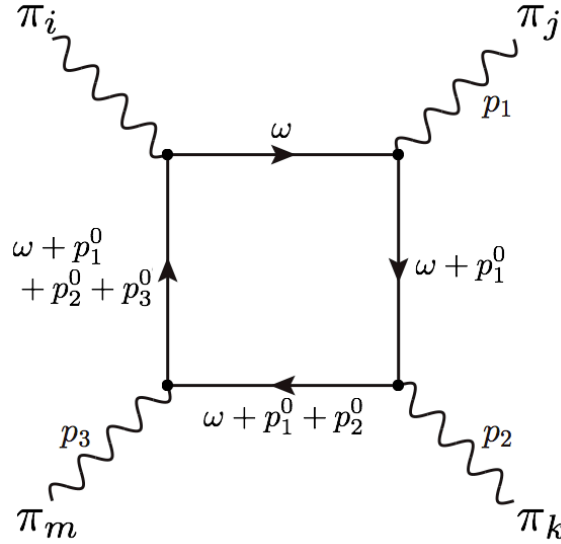
Figure 3.2: Box diagram leading to $\mathcal{S}_\pi$. The full lines are the Green's function in Eq. (3.19) at the labeled frequencies, and the vertices are the λ term in Eq. (3.3).

Substituting $n_a = (\pi_1, \pi_2, \pi_3, \pi_4, 1)$ to Eq. (3.8) we get the Hamiltonian,

$$H = H_0 + H_\pi$$

$$= -\lambda \sum_{n,X} c_{n,X}^\dagger \Gamma_5 c_{n,X} - \lambda \sum_{i=1}^{4} \int d^2\boldsymbol{q}\, \pi_i(-\boldsymbol{q}) \sum_{n,n',X} e^{-iq_x X} c_{n,X-q_y/2}^\dagger \Gamma_i\, c_{n',X+q_y/2} F_{n,n'}(\boldsymbol{q}).$$

$$(3.20)$$

From the above equation, we integrate out the fermions to get an effective theory for the fluctuating order parameters. The coupling between the order parameters appear at fourth order of one-loop expansion. In momentum space, the four point coupling between the order parameter fields are,

$$S_1 = \int \prod_{\alpha=1}^{3} d\boldsymbol{p}_\alpha K_{\boldsymbol{p}_1\boldsymbol{p}_2\boldsymbol{p}_3}^{jkm;i} \pi_j(\boldsymbol{p}_1)\pi_k(\boldsymbol{p}_2)\pi_m(\boldsymbol{p}_3)\pi_i(-\boldsymbol{p}_1-\boldsymbol{p}_2-\boldsymbol{p}_3). \qquad (3.21)$$

Among these terms, we are most interested in the topological term,

$$S_\pi = iK \int d^2\boldsymbol{r} d\tau \epsilon_{ijkm}\pi_i\partial_x\pi_j\partial_y\pi_k\partial_\tau\pi_m. \qquad (3.22)$$

To extract the coefficient K from S_1 we expand $K^{jkm;i}_{\boldsymbol{p_1 p_2 p_3}}$ in powers of momenta and frequency, and consider the terms linear in $p_1 p_2 p_3$:

$$K^{jkm;i}_{\boldsymbol{p_1 p_2 p_3}} = \cdots + K^{jkm;i}_{\alpha\beta\gamma} p_1^\alpha p_2^\beta p_3^\gamma + \cdots . \tag{3.23}$$

Here, α, β, γ are spacetime indices τ, x, y. In real space, these terms correspond to the derivative expansion.

$$S_1 = \cdots + i \sum_{i,j,k,m=1}^{4} K^{jkm;i}_{\alpha\beta\gamma} \int d^2\boldsymbol{r} d\tau \, \pi_i \partial_\alpha \pi_j \partial_\beta \pi_k \partial_\gamma \pi_m + \cdots . \tag{3.24}$$

Comparing Eq. (3.22) with Eq. (3.24), we obtain the expression for K in terms of $K^{jkm;i}_{\alpha\beta\gamma}$'s.

$$24K = \epsilon_{\alpha\beta\gamma} \epsilon_{ijkm} K^{jkm;i}_{\alpha\beta\gamma}. \tag{3.25}$$

Note the summation of repeated indices are implicit, and thus the right-hand side of the above equation consists of 144 terms.

Now we only need to calculate $K^{jkm;i}_{\alpha\beta\gamma}$ to obtain K. This can be done by calculating the box diagrams in Fig. 3.2. The kinetic energy of fermions are quenched, and the propagators are momentum independent. Therefore, the momentum dependence comes from the vertices and frequency dependence comes from the propagator.

Recalling Eq. (3.20), the inverse Green's function is written as $G^{-1} = -i\omega + H_0$, where ω is the Matsubara frequency of the fermions. The effective action of order π^4 in perturbation theory, which is of our interest according to Eq. (3.24), is:

$$\mathcal{S}[\pi^4] = \frac{1}{4} \text{tr} \left(G H_\pi G H_\pi G H_\pi G H_\pi \right). \tag{3.26}$$

Considering the momentum flow in Fig. 3.2, we obtain the expression for $K^{jkm;i}_{\alpha\beta\gamma}$.

$$K^{jkm;i}_{\alpha\beta\gamma} = \frac{1}{4} \left(\partial_{p_1^\alpha} \partial_{p_2^\beta} \partial_{p_3^\gamma} \text{tr} \left(G(k) H^j_\pi(p_1) G(k+p_1) H^k_\pi(p_2) G(k+p_1+p_2) \right. \right.$$
$$\left. \left. \times H^m_\pi(p_3) G(k+p_1+p_2+p_3) H^i_\pi(-p_1-p_2-p_3) \right) \right) \Big|_{p_1=p_2=p_3=0} . \tag{3.27}$$

We used a shorthand notation H^a_π for $H^a_\pi = H_\pi(\pi_{i=a} = 1, \pi_{i\neq a} = 0)$.

We get the value of K by calculating Eq. (3.27). In zero temperature, the frequency integral can be done analytically,

$$
\begin{aligned}
K &= \frac{1}{2\pi} \int d\omega \sum_{X} \frac{2q\lambda^5}{(\omega^2 + \lambda^2)^3} \\
&= \sum_{X} \frac{3q}{8} \\
&= \frac{3q}{16\pi}.
\end{aligned}
\tag{3.28}
$$

The individual diagram is independent of X, merely reflecting momentum conservation. Therefore the X summation is just multiplying N_Φ, which equals (sample area)/(2π). This yields the following contribution to the action:

$$
\mathcal{S}_\pi = \frac{i3q}{16\pi} \int d^2\boldsymbol{r}\, d\tau\, \epsilon_{ijkm} \pi_i \partial_x \pi_j \partial_y \pi_k \partial_\tau \pi_m \,.
\tag{3.29}
$$

It can be checked that Eq. (3.4) reduces to $\mathcal{S}_\pi$ for $n_a = (\pi_1, \pi_2, \pi_3, \pi_4, 1)$, and so $\mathcal{S}_{\text{WZW}}$ is the explicitly SO(5) invariant form of $\mathcal{S}_\pi$.

3.4   Theoretical consequences

We now turn to a discussion of the theoretical consequences of the WZW term for the vicinity of the AF-VBS transition. For $q = 1$, it has been demonstrated in Levin and Senthil (2004), Grover and Senthil (2008), Senthil and Fisher (2006) that the O(5) nonlinear sigma model with O(3)×O(2) anisotropy and a level 1 WZW term is equivalent to the CP^1 model in 2+1 dimensions. This is the same model appearing in the AF-VBS transition of SU(2) quantum spin models (Senthil et al., 2004a,b), and is a relativistic field theory with a U(1) gauge field and a two-component complex scalar z_α. In terms of these fields, the AF order is $z_\alpha^* \sigma_{\alpha\beta}^s z_\beta$, with $s = x, y, z$; so the vector AF order has been "fractionalized" into spinons z_α. Alternatively, we can also view the z_α quanta as representing the vortices or antivortices in the VBS order (Levin and Senthil, 2004) which, as we have just seen, carry spin $S = 1/2$.

Presently, the experimentally accessible case of the AF-VBS transition is in bilayer graphene, so we focus now on the $q = 2$ case. With a level 2 WZW term, the VBS

vortices carry spin $S = 1$, and therefore we need complex scalar fields with three components: we write these as Z_s, with $s = x, y, z$. The field theory of the Z_s quanta is now the CP^2 model with anisotropic quartic terms; such a field theory was considered in Grover and Senthil (2007) in a different context:

$$\mathcal{L}_{cp} = |(\partial_\mu - iA_\mu)Z_s|^2 + g|Z_s|^2 + u_1(|Z_s|^2)^2 + u_2(Z_s^2)(Z_t^{*2}).$$

Here μ is a spacetime index, A_μ is the emergent U(1) gauge field, g is the coupling which tunes the AF to VBS transition, and $u_{1,2}$ are quartic couplings. In terms of the degrees of freedom in $\mathcal{L}_{cp}$, the three-component AF order parameter is now $i\epsilon_{stu}Z_t^* Z_u$, while the complex VBS order $\langle \rho^x + i\rho^y \rangle \sim e^{i\theta}$ is the monopole operator in the U(1) gauge field (Read and Sachdev, 1990; Senthil et al., 2004b).

For both the CP^1 and CP^2 models mentioned above, both first and second order transitions are possible between the AF and VBS states. A recent numerical study (Wu et al., 2014) on a single layer model indicates a first order transition for the parameters studied.

3.5 Experimental implications

Finally, we turn to experimental consequences for bilayer graphene. The defining characteristic of deconfined criticality is the presence of a gapless "photon" excitation of an emergent U(1) gauge field (Senthil et al., 2004a). This is associated with the A_μ above, and can also be interpreted as a "spin-wave" excitation involving fluctuations of the angle θ. Our definition of θ shows that it is the angular phase associated with off-diagonal-long-range order (ODLRO) in valley space. The valley anisotropy terms in graphene are very small (Kharitonov, 2012a; Wu et al., 2014), because it is suppressed by powers of the lattice spacing to the magnetic length; so we expect a nearly gapless θ spin-wave mode to be present (and most of the remarks below to also apply) even in the case of a first-order transition.

Now recall the fact, noted earlier, that in the zero energy Landau levels the valley index coincides with the layer index of bilayer graphene (and also the sublattice

index). So ODLRO in valley space is accompanied by ODLRO in the layer space; *i.e.*, θ is also the angular phase of interlayer excitonic superfluidity. Signatures of excitonic superfluidity have been observed in quantum Hall states in GaAs bilayers (Eisenstein, 2014). However, in the GaAs bilayers there is negligible tunneling of electrons between the layers, and this crucial to the emergence of a U(1) symmetry which is broken by the excitonic condensate. So it might seem surprising that a similar superfluidity can be present in graphene bilayers, in the presence of very strong tunneling between the layers. The resolution is the identification of the layer and valley indices in the zero energy Landau levels of bilayer graphene: in the absence of intervalley scattering by impurities, and the irrelevancy of valley anisotropy terms to be presented below, there is also an emergent interlayer U(1) symmetry in bilayer graphene.

The counterflow electrical current can be written in terms of the gauge field

$$J_{t\mu} - J_{b\mu} = \frac{4e}{2\pi}\epsilon_{\mu\nu\lambda}\partial_\nu A_\lambda \qquad (3.30)$$

where J_t and J_b are the currents in the top and bottom layers, and e is the charge of the electron. The factor of 4 is deduced from Eq. (3.5), which shows that a AF Skyrmion in (n_1, n_2, n_3) has excitonic charge density $\langle \rho^z \rangle = 4$ for $q = 2$. The counterflow conductivity can be computed from Eq. (3.30) using $\mathcal{L}_{cp}$; at the $g = g_c$ deconfined quantum critical point this implies a universal value of order, the quantum unit of conductance e^2/h.

For $g > g_c$, in the VBS state, the conductivity should be computed using an effective action for θ which includes the influence of monopoles. Now the current is

$$J_{t\mu} - J_{b\mu} = 4e\rho_s\partial_\mu\theta \qquad (3.31)$$

where ρ_s is the stiffness of the excitonic superfluidity appearing the effective Lagrangian density

$$\mathcal{L}_\theta = \frac{\rho_s}{2}(\partial_\mu\theta)^2 - y_3\cos(3\theta), \qquad (3.32)$$

with y_3 the fugacity of tripled monopoles which are allowed by the threefold rotational symmetry of the underlying honeycomb lattice (Read and Sachdev, 1990). The stiffness vanishes as $\rho_s \sim (g - g_c)^\nu$ by the Josephson relation, where ν is the correlation

length exponent. Away from the critical point, the bare value y_3^0 is proportional to the very small threefold valley anisotropy term (Kharitonov, 2012a; Wu et al., 2014); y_3 has a further suppression (Chubukov et al., 1994; Senthil et al., 2004b) from the critical fluctuations of $\mathcal{L}_{cp}$ leading to $y_3 = y_3^0(g - g_c)^{\nu\Delta}$, where Δ is the scaling dimension of the tripled monopole operator. So the effective "interlayer tunneling" term, y_3, is highly suppressed near the deconfined quantum critical point. We also note that numerical studies on square lattice antiferromagnets have provided striking evidence for the emergent U(1) symmetry due to the suppression of monopoles (Sandvik, 2007), and there is direct evidence for the suppression of monopoles on the honeycomb lattice in the work of Block et al. (2013).

In GaAs bilayers (Eisenstein, 2014), the excitonic superfluidity is most directly observed in counterflow experiments, where electric currents flow in the opposite direction in the two layers. This would be technically more difficult in bilayer graphene, given the close spacing of the layers, but experiments of this type would be ideal. In the bilayer graphene experiments of Weitz et al. (2010), there is a Zeeman coupling to the magnetic field (whose consequences have been studied earlier in Senthil et al. (2004b)), and an electric field is applied transverse to the layers. The electric field provides a small breaking of the layer-exchange symmetry. In the presence of such a symmetry breaking, there is a coupling between the counterflow and parallel current modes, and a vestige of the counterflow superfluidity would also be present in a measurement of the total current in both layers. Weitz et al. (2010) observe a phase transition out of the (presumed) AF state, signaled by the enhancement of the conductivity. We propose that this enhancement is due to the coupling to counterflow superfluidity.

Chapter 4

Electronic quasiparticles in the quantum dimer model: density matrix renormalization group results

4.1   Introduction

A recent paper (Punk et al., 2015) has proposed a simple quantum dimer model for the pseudogap metal state of the hole-doped cuprates. The objective of this model is to describe a metal with electron-like quasiparticles, carrying spin 1/2 and charge e, but with a Fermi volume which violates the Luttinger theorem for a Fermi liquid (FL). In particular, doping a density of p holes away from a half-filled insulator should yield, in Fermi liquid theory, a hole Fermi surface of size $1 + p$. And indeed, just such a Fermi surface is observed at large p (Platé et al., 2005). However, for $p \approx 0.1$, in the pseudogap metals, many physical properties are well described by a model of electron-like quasiparticles with a Fermi surface of size p (Sachdev and Chowdhury, 2016). Such a Fermi surface can be obtained in a 'fractionalized Fermi liquid' (FL*) (Senthil et al., 2003, 2004). The model of Punk et al. (2015) was designed to yield a

$$\text{(blue dimer)} = \left(\left| \uparrow \downarrow \right\rangle - \left| \downarrow \uparrow \right\rangle \right) / \sqrt{2}$$

$$\text{(green dimer)} = \left(\left| \uparrow \circ \right\rangle + \left| \circ \uparrow \right\rangle \right) / \sqrt{2}$$
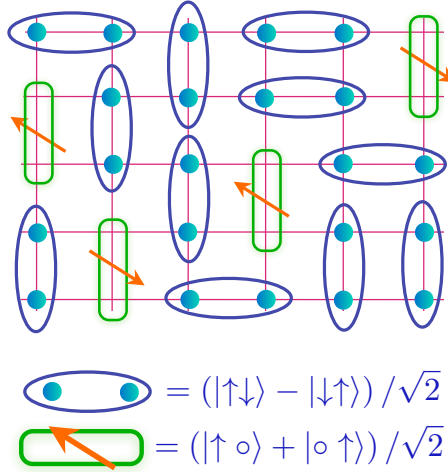
Figure 4.1: A state in the Hilbert state of the dimer model. The blue dimers are bosons representing a spin-singlet pair of electrons. The green dimers are spin $1/2$ fermions representing an electron in a bonding orbital between a pair of sites.

FL* state with a Fermi surface of size p using ingredients that are appropriate for a single-band model of cuprate physics.

This chapter will present density matrix renormalization group (DMRG) results on the dimer model. The exact diagonalization results in Punk et al. (2015) were limited to a lattice size of 8×8 and a single fermionic dimer. Here we study significantly larger systems with up to 8 fermions, and obtain results on the density distribution of the fermionic dimers and the entanglement entropy. As we shall see below, all of our results are consistent with the appearance of a FL* metal in this dimer model.

4.2   Model and DMRG Setup

The quantum dimer model of Punk et al. (2015) has bosonic dimers and spin $1/2$ fermionic dimers, which close pack a square lattice with an even number of sites: see Fig. 4.1. The bosonic sector of this model is identical to the original study of Rokhsar and Kivelson (RK) (Rokhsar and Kivelson, 1988), with potential and resonating term for dimers within a plaquette. In addition, fermionic dimers may move via hopping terms whose form will be specified below. Interaction between the fermionic dimers

can in principle be present, but are not expected to be important when the density of fermions is low; we will not include fermion-fermion in interactions here.

Now we state the Hamiltonian for this model. Let us first define the operators creating (annihilating) bosonic and fermionic dimers as $D_{ix}^\dagger (D_{ix})$ and $F_{ix\alpha}^\dagger (F_{ix\alpha})$, respectively. The extra indices i and $x(y)$ indicates the created or annihilated dimer resides on the link between $i = (i_x, i_y)$ and $i+\hat{x}(\hat{y})$, where $\hat{x} = (1,0)$ and $\hat{y} = (0,1)$ are unit vectors and $\alpha =\uparrow,\downarrow$ is spin index. Note that we set the lattice spacing as 1. In the language of the *t-J* model, D and F operators have the following correspondence to the electron creation and annihilation operators $c^\dagger$, c,

$$D_{i\eta}^\dagger \sim \frac{(-1)^i}{\sqrt{2}} \left(c_{i\uparrow}^\dagger c_{i+\hat{\eta},\downarrow}^\dagger + c_{i\downarrow}^\dagger c_{i+\hat{\eta},\uparrow}^\dagger \right),$$

$$F_{i\eta\alpha}^\dagger \sim \frac{(-1)^i}{\sqrt{2}} \left(c_{i\alpha}^\dagger + c_{i+\hat{\eta},\alpha}^\dagger \right). \tag{4.1}$$

$(-1)^i$ is due to a gauge choice which we follow from Rokhsar and Kivelson (1988). We can observe that the quantum numbers of states $D_i^\dagger |0\rangle$ and $F_{i\alpha}^\dagger |0\rangle$ are the same as $c_{i\uparrow}^\dagger c_{i\downarrow}^\dagger |0\rangle$ and $c_{i\alpha}^\dagger |0\rangle$, setting aside the fact that the degrees of freedom of the former lives between two sites (i and $i + \hat{\eta}$) and the latter resides on each site. This fact will be useful in our DMRG setup. We can now write the Hamiltonian for the model in terms of dimer creation and annihilation operators (Punk et al., 2015),

$$H = H_{\text{RK}} + H_1$$

$$H_{\text{RK}} = \sum_i \Big[-J\, D_{ix}^\dagger D_{i+\hat{y},x}^\dagger D_{iy} D_{i+\hat{x},y} + 1 \text{ term}$$

$$+V\, D_{ix}^\dagger D_{i+\hat{y},x}^\dagger D_{ix} D_{i+\hat{y},x} + 1 \text{ term}\Big]$$

$$H_1 = \sum_{i,\alpha} \Big[-t_1\, D_{ix}^\dagger F_{i+\hat{y},x\alpha}^\dagger F_{ix\alpha} D_{i+\hat{y},x} + 3 \text{ terms}$$

$$-t_2\, D_{i+\hat{x},y}^\dagger F_{iy\alpha}^\dagger F_{ix\alpha} D_{i+\hat{y},x} + 7 \text{ terms}$$

$$-t_3\, D_{i+\hat{x}+\hat{y},x}^\dagger F_{iy\alpha}^\dagger F_{i+\hat{x}+\hat{y},x\alpha} D_{iy} + 7 \text{ terms}$$

$$-t_3\, D_{i+2\hat{y},x}^\dagger F_{iy\alpha}^\dagger F_{i+2\hat{y},x\alpha} D_{iy} + 7 \text{ terms}\Big]. \tag{4.2}$$

The terms we have not explicitly written down are connected with the previous term through a symmetry transformation of the square lattice. H_{RK} is the pure bosonic sector mentioned above; J is the coupling for the resonant term, and V is the coupling for the potential term. H_1 contains the hopping terms of the fermionic dimers; t_1, t_2, and t_3 correspond to three distinct types of hoppings.

In our DMRG calculation, we consider a lattice with geometry of a finite cylinder. The circumference of the cylinder consists of four lattice sites, and the length of the cylinder is up to 32 sites. In the second part of this chapter, we also compute entanglement entropies in 64×2 cylinder to observe one-dimensional effects. We repeat our calculation in different fermionic dimer densities, from one to 8 fermionic dimers. Note that in our lattice configuration, 8 fermionic dimers correspond to 1/16 doping in the typical cuprate phase diagram. We use two sets of parameters for the couplings in Eq. (4.2). One is the parameters which is relevant to the physical model for the cuprates in the pseudogap regime: $t_1 = -1.05J$, $t_2 = 1.95J$, and $t_3 = -0.6J$, at the RK point ($J = V$). The other is the parameter which we choose for comparison: $t_1 = t_2 = t_3 = J$, at the RK point ($J = V$). Single fermion study in Punk et al. (2015) suggests the different hopping parameters change the dispersion of the fermionic dimer: the Fermi surface consists of four hole pockets near ($\pm\pi/2$, $\pm\pi/2$) in the former parameter regime, and a single Fermi surface centered at $(0, 0)$ in the latter. We will confirm this behavior in our DMRG calculation below, while studying a multiple fermion system.

The fact that we are interested in observing the hole pockets, is closely related to the reason we chose the circumference as four lattice site for the first part of our calculation. The center of the four hole pockets are at $\vec{k} \sim (\pm\pi/2, \pm\pi/2)$, and the minimum number of sites in y-direction needed to get information about $k_y = \pm\pi/2$ is four. This is why we could not choose two sites in the circumference when our focus is in the fermion dispersion. Later when we concentrate on the one-dimensional scaling properties of the entanglement entropies, we compute the case of a cylinder of two sites along the circumference, which allows us to calculate much longer system.

Now we comment on the topological sectors of the Hamiltonian. The Hilbert

space we are considering consists of closely packed configurations of dimers. For each configuration, we can define an integer quantity

$$w_x = \sum_{i_x=1}^{N_x} (-1)^{i_x} (D^\dagger_{(i_x,i_y)y} D_{(i_x,i_y)y} + F^\dagger_{(i_x,i_y)y\alpha} F_{(i_x,i_y)y\alpha}), \qquad (4.3)$$

for any $1 \leq i_y \leq N_y$, where $N_x(N_y)$ is the number of sites in the $x(y)$ direction and the spin α implicitly summed. One can observe that every term in Eq. (4.2) preserves this quantity, so the possible configurations of the dimers spanning the Hilbert space can be divided in different sectors with different values of w_x. The integer w_x serves as the topological winding number in the x direction in our model, similar to that of the RK model on a torus (Rokhsar and Kivelson, 1988). The integer w_y can be defined in an analogous manner, but it is not meaningful since we do not have periodic boundary condition in x-direction. In principle, we would like to restrict ourselves in the zero winding number sector, $w_x = 0$. However, this is not a local constraint and thus we cannot prevent DMRG from accessing other topological sectors. Right at the RK point, $J = V$, each topological sector has a unique ground state, which is an equal superposition of all configurations (Rokhsar and Kivelson, 1988). Since the number of configurations are largest at $w_x = 0$, sectors with large absolute value of w_x have lower entanglement and will be preferred by DMRG. Therefore to force our calculation within the $w_x = 0$ sector, we tune V to be slightly smaller than J and penalize states moving away from $w_x = 0$. In all of our calculation, we have used $V = 0.9J$.

Each bond in the square lattice can have four states: occupied by a bosonic dimer, occupied by a spin up or down fermionic dimer, or empty. As mentioned previously, one useful observation is that the quantum numbers of the bonds are the same as the quantum numbers of the sites in a spin-half fermion model, with the bosonic dimer occupied state corresponding to the filled (spin up and down) state. Therefore we can map our dimer model to a fermion Hubbard model on the links, with dimer constraints. The dimer constraint is to ensure each site is part of only one dimer, and this is achieved in our DMRG as an additional potential term. We use a potential of $\sim 20J$ to penalize overlapping dimers.

All DMRG calculations in this chapter were performed with the ITensor library (`http://itensor.org/`). We kept up to ~ 6000 states to keep the truncation error per step to be $\sim 10^{-12}$. The number of states needed to be increased as we increased the fermionic dimer density.

4.3   Density Modulation

Now we show the results of the DMRG calculations where we can observe the change in dispersions with different hopping parameters, and especially the existence of a dispersion with Fermi pockets centered near $\vec{k} = (\pm\pi/2, \pm\pi/2)$. Extracting momentum information from DMRG is not trivial since it is a real-space calculation (There are more recent schemes for DMRG in mixed real and momentum space proposed in Motruk et al. (2016)). However, we may observe Friedel oscillations from the open boundaries of our system, and these will reveal information of the fermionic dimer's momentum in the cylinder direction.

First we check whether the Friedel oscillation observed in the case of a single fermionic dimer is consistent with Punk et al. (2015). Fig. 4.2 is the density profile of the fermionic dimers when a single fermionic dimer is present among bosonic dimers on a 16×4 lattice, for the two parameter sets we use. From Fig. 4.2(a), which is the parameter set expected to have hole pockets, we can observe an oscillation of the profile starting from the open boundary to the x-direction. This is especially clear when looking at the vertical dimers. The period of the oscillation is roughly two lattice sites. Since the Friedel oscillation has a wavevector of $2k_F$, this indicates that the fermionic dimer in the ground state has crystal momentum of $k_x \sim \pi/2$. This fact is consistent with the exact diagonalization study in Punk et al. (2015), which found the energy minima of the single fermion spectrum to be near $\vec{k} = (\pi/2, \pi/2)$. On the other hand, Fig. 4.2(b) does not show any prominent oscillation near the boundary. This calculation has been done with the parameters which is expected to have a single band with the dispersion minima at $\vec{k} = (0, 0)$, so the absence of Friedel oscillation is expected. We have performed the same calculation for a single fermionic dimer while
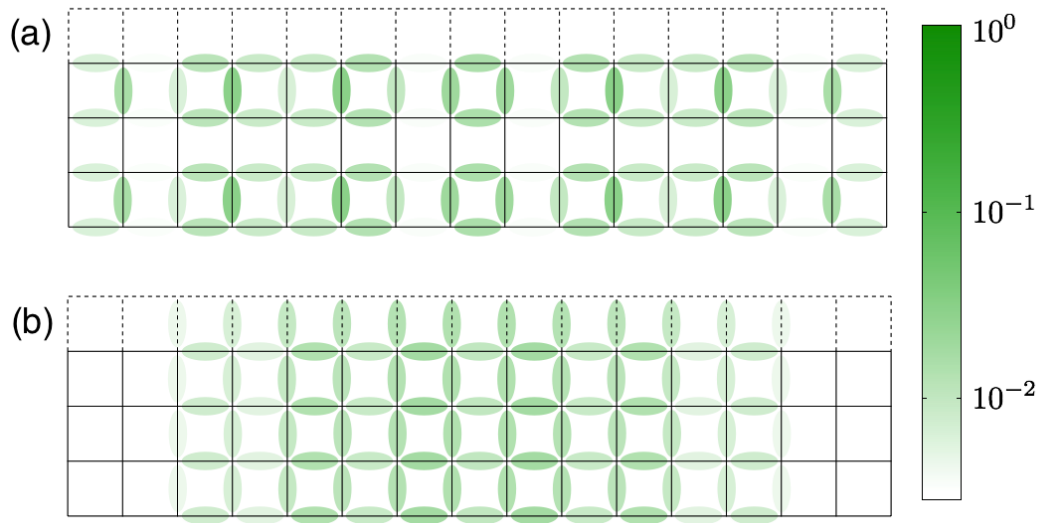
Figure 4.2: The log scale density of fermionic dimers on a 16×4 lattice. The configuration consists with a single fermionic dimer and 31 bosonic dimers. The dashed line indicates the periodic boundary condition in the y-direction; the top dashed line is identified to the bottom solid line. The hopping parameters used are (a) $t_1 = -1.05J$, $t_2 = 1.95J$, $t_3 = -0.6J$; (b) $t_1 = t_2 = t_3 = J$. In (a), one can observe the density oscillation with period of roughly two lattice sites, which corresponds to crystal momenta of $\pi/2$. Note that the Hilbert space is closely packed dimer configuration, and sites without fermionic dimers are occupied by bosonic dimers.

increasing the x-direction of lattice size, up to 32×4 lattice and observed the same behavior, in both cases with dispersion minima at $k_x = \pi/2$ (Fig. 4.2(a)) and $k_x = 0$ (Fig. 4.2(b)). A more quantitative analysis for the 32×4 lattice by Fourier transform will follow below, together with the higher density calculation.

Note that Fig. 4.2(a) seems to break the translation symmetry in y-direction. However, this is just a spontaneous symmetry breaking between the two degenerate ground states; one being Fig. 4.2(a) and the other being Fig. 4.2(a) translated by one lattice site in the y-direction. One can check this by computing the ground state multiple times and obtaining both states. The fact that Fig. 4.2(b) does not break the symmetry is also in accordance with our claim. Since the state of Fig. 4.2(b) has only one Fermi surface centered at $\vec{k} = (0, 0)$, there are no degeneracy in the ground state.

We would like to study the Friedel oscillation more quantitatively and verify whether this feature survives when we increase the number of fermionic dimers, n. We keep the lattice size as 32×4 and increase n up to 8, which corresponds to $1/16$ doping. Since the 'defects' of the system are the open boundaries, the Friedel oscillation is in the cylinder direction. From the density profile $\rho(x, y)$, we define $\rho_x(x) = \sum_y \rho(x, y)$ and perform Fourier transformation. The result is shown in Fig. 4.3. Note that we have normalized the data by $1/n$, and the magnitude 1 peak at $k_x = 0$ indicates the total density is n. Other than the $k_x = 0$ peak, we can observe that there is a peak at $k_x = 7\pi/8$ in Fig. 4.3(a), where the parameter set used is the same as Fig. 4.2(a). This peak is due to the Friedel oscillation, and indicates that $k_x = 7\pi/16$ at the Fermi level. Punk et al. (2015) showed the energy minimum is at $\vec{k} = (q, q)$ for q slightly less than $\pi/2$, and this is in good agreement with our result. Our calculation cannot resolve the value of k_y, but based on experiments and previous works one can argue the energy minimum should be either at the origin ($\vec{k} = (0,0)$) or along the diagonal ($\vec{k} = (q, q)$). Therefore, we can conclude the dispersion of the dimer model in our cylinder will have a minimum at $\vec{k} = (7\pi/16, \pi/2)$, and in the large system limit this will converge to a diagonal point $\vec{k} = (q, q)$ with $7\pi/16 \leq q \leq \pi/2$.

For Fig. 4.3(b), which used the same parameter set as Fig. 4.2(b), there is no peak
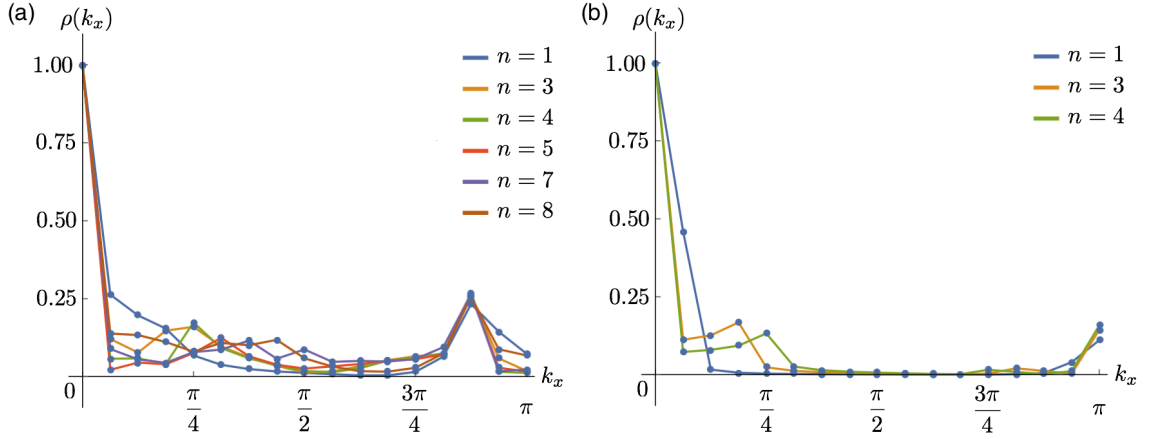
Figure 4.3: Fourier transform of the density of fermionic dimers with various total densities. n denotes the number of fermionic dimers in the system. Note that in our 32×4 lattice, $n = 8$ corresponds to $1/16$ doping. The hopping parameters used are (a) $t_1 = -1.05J$, $t_2 = 1.95J$, $t_3 = -0.6J$; (b) $t_1 = t_2 = t_3 = J$. In (a), there is a consistent peak at $7\pi/8$ which indicates the fermionic dimer with $k_x = 7\pi/16$ is at the Fermi level, which is a feature missing in (b). The central peak at 0 is due to the total density and is normalized to 1.

at $k_x = 7\pi/8$ for any n. This is in accordance with our expectation that the state has dispersion minimum at $\vec{k} = (0, 0)$, and also with the qualitative result we have seen in Fig. 4.2(b). There is a signal at $k_x = \pi$, however the origin of this signal is not the Friedel oscillation. Fig. 4.4 shows the density of the fermionic dimer as a function of x. The plotted one-dimensional density $\rho(x) = \sum_y \rho(x, y)$ is the Fourier transform of $\rho(k_x)$, which is the quantity plotted in Fig. 4.3. The x-axis of the plot is the position in the unit of lattice constant. Integer values are for the vertical bonds and half-integers are for the horizontal bonds. Looking at only the vertical bonds does not show any modulation in the density and looks very much like a particle in a box. On the other hand, the horizontal bond shows some modulation with two lattice sites. This density modulation clearly has a wavevector of π, and is the reason of the signal at $k_x = \pi$ in Fig. 4.3(b). Although the precise reason for this oscillation is unclear, we can clearly see that this modulation is present throughout the bulk and the signal at $k_x = \pi$ does not indicate Friedel oscillation from $k_F = \pi/2$: it appears to be simply a lattice commensuration effect.
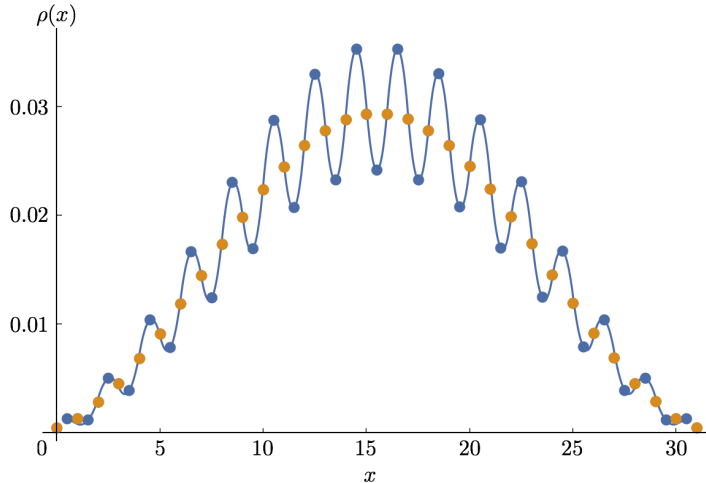
Figure 4.4: One dimensional plot for fermionic dimer density $(\rho(x) = \sum_y \rho(x,y))$ as a function of distance in x direction, when $n = 1$. The x-axis unit is the lattice constant. Vertical bonds have integer x and colored yellow; horizontal bonds have half-integer x and colored blue. Notice the modulation is only present in the horizontal dimers. The system is a 32×4 cylinder with parameters $t_1 = t_2 = t_3 = J$.

Note that we have not included the data obtained for n which $\mathrm{mod}\,(n,4) = 2$. The calculations with such n had a stronger tendency towards $w_x \neq 0$ topological sector, and we had to decrease V further to keep the state in $w_x = 0$ (For $n = 2$, we needed $V < 0.8$). This seems to be an artifact of our system which is effectively one-dimensional and can only have four values of k_y.

4.4   Entanglement entropy

We present the result for the computation of Rényi entropy to gain more information about the ground state of the dimer model. First recall the definition of the α-th Rényi entanglement entropy:

$$S_\alpha = \frac{1}{1-\alpha}\ln\left[\mathrm{Tr}\,\rho_A^\alpha\right]. \tag{4.4}$$

Here, ρ_A is the reduced density matrix of partition A, i.e. $\rho_A = \mathrm{Tr}_B\,\rho$, where $A \cup B$ is the total system. Note that α-th Rényi entropy becomes the von Neumann entropy in the $\alpha \to 1$ limit.
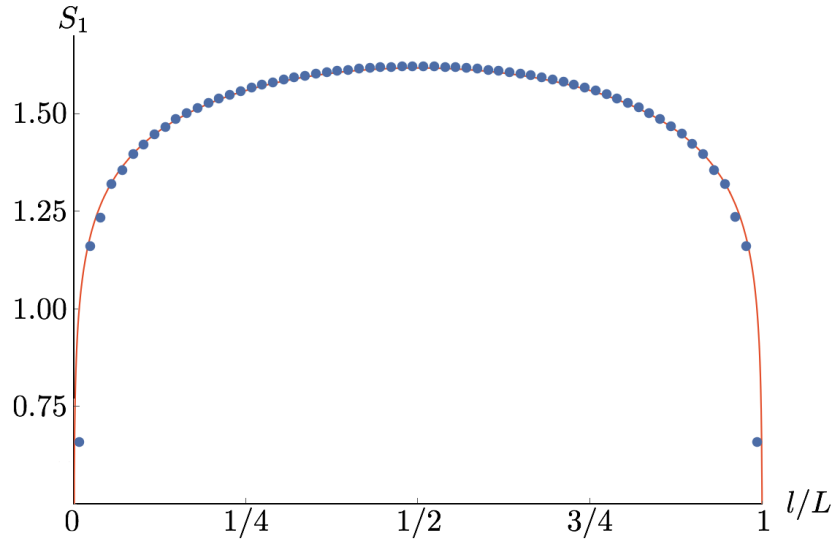
Figure 4.5: von Neumann entropy of the pure RK model, calculated on a 64×2 cylinder. The red solid line is not the interpolation of the data points, but the exact CFT result of Eq. (4.5) with $c = 1$ and $g + c'_\alpha = 1$.

In a one-dimensional gapless system, conformal field theory (CFT) has a result for the scaling of the Rényi entropy (Calabrese and Cardy, 2004; Calabrese et al., 2010):

$$S_\alpha = \frac{c}{12} \left(1 + \frac{1}{\alpha} \right) \ln \left(\frac{2L}{\pi} \sin \frac{\pi l}{L} \right) + g + c'_\alpha. \tag{4.5}$$

This is the case for a finite system of length L with open boundary condition, divided into two pieces which length of one piece is l. g is the boundary entropy (Affleck and Ludwig, 1991), and c'_α is a non-universal constant. Considering our system as quasi-1D, we can extract the central charge c, of the system from this equation. For the entanglement entropy calculation, we consider both 32×4 and 64×2 cylinder to see any scaling behavior as the system approaches to one-dimension. Moreover, now we concentrate on the parameters which gives a single Fermi surface, $t_1 = t_2 = t_3 = J$. The results for the other parameter are expected to be four copies of the presented results, in the thermodynamic limit. However, the convergence of the wavefunction was not good enough to compute the entanglement entropies.

First we show the comparison of the von Neumann entropy of the pure RK model, with $n = 0$ fermions, with the CFT result (4.5) in Fig. 4.5. An excellent fit is found
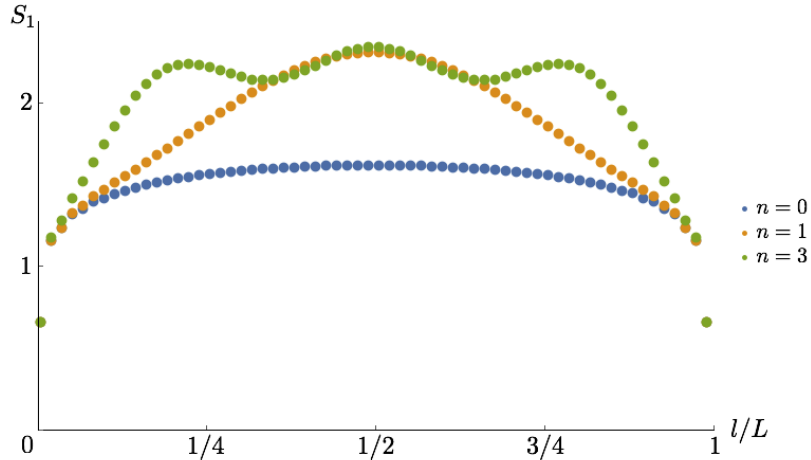
Figure 4.6: von Neumann entropy of the FL* phase with different fermionic dimer densities. The system is a 64×2 cylinder with parameters $t_1 = t_2 = t_3 = J$. L is the length of the system, and l is the length of the subsystem. In the case of $n = 0$, which is a pure bosonic dimer model near the RK point, we get a nice fit to Eq. (4.5) with central charge 1.

for $c = 1$. The fermion-free dimer model is dual to a sine-Gordon model (Fradkin and Kivelson, 1990; Read and Sachdev, 1990), and in 1+1 dimension this has a gapless phase described by a massless relativistic boson with $c = 1$. The results of Fig. 4.5 are in accord with this expectation.

Turning to the case with fermions, the von Neumann entropy with dispersion expected to have a single Fermi surface near $\vec{k} = (0,0)$ is shown in Fig. 4.6. The results are for 64×2 lattice. Data for 32×4 lattice are not shown, but are very similar to the presented data (32×4 results are included in Fig. 4.7). We also include the data from Fig. 4.5 for the case without any fermions. It is clear that these is an additional contribution from the presence of the fermions, but it cannot be accounted for by changing the central charge of the CFT. Fermions at non-zero density in an infinite system should form a Fermi surface, and in the quasi-one dimensions geometry, each Fermi point should yield an additional contribution of $c = 1/2$ of a chiral fermion. It is clear that the data in Fig. 4.6 are not of this form.

Instead, we found that an excellent understanding of Fig. 4.6 is obtained by thinking about the limit of a very low density of fermions at the bottom of a quadratically
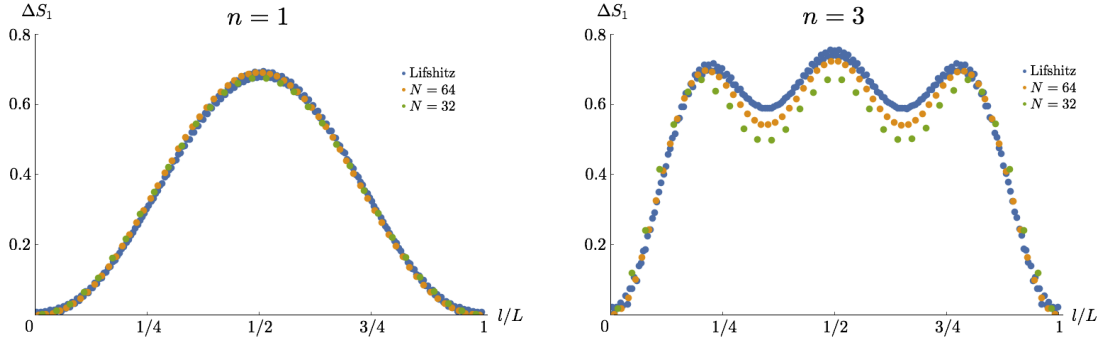
Figure 4.7: Fermion contribution to von Neumann entropy of the dimer model and the Lifshitz transition. ΔS_1 equals $S_1(n=1)-S_1(n=0)$ in the left, $S_1(n=3)-S_1(n=0)$ in the right, where n is the number of fermionic dimers. The system is 64×2 and 32×4 cylinder with parameters $t_1 = t_2 = t_3 = J$ for the dimer model, and free fermions on a 200 site chain for the Lifshitz transition. The $n=1$ and $n=3$ cases for Lifshitz transition corresponds to the number of occupied state in the new band.

dispersing band. This is the case of a "Lifshitz" transition in one dimension, when the chemical potential crosses the bottom of a band. Rodney et al. (2013), studied the entanglement entropy near such a Lifshitz transition. In their Fig. 11, they present the entanglement entropy of a half-filled free fermion system with 200 sites, as the next-nearest hopping t is tuned to go across the Lifshitz transition (The Hamiltonian used is $H = -\sum_i (c_i^\dagger c_{i+1} + t c_i^\dagger c_{i+2}) + \text{h.c.}$). Different graphs are labeled by different values of t, but basically what is changing is the number of occupied states above the Lifshitz transition. For example, when $t = 0.5$, only the large Fermi surface is occupied; when $t = 0.51$, the system has just gone through Lifshitz transition and one state is occupied from the new band; when $t = 0.52$, two states are occupied above the Lifshitz transition. The number of modulations in the entanglement entropy exactly matches the number of states filled above the Lifshitz transition.

We reproduced the data of Fig. 11 in Rodney et al. (2013) to compare with the behavior of the entanglement entropy with our own system of fermionic and bosonic dimers. Fig. 4.7 shows the fermionic contribution ΔS_1 of the entanglement entropy. This is obtained by subtracting the entanglement entropy of $n = 0$, which was shown in Fig. 4.5 to be due to a $c = 1$ boson field. To compare with the case of Lifshitz

transition, we also subtract the entanglement entropy of the system with only one large band occupied, which is $t = 0.50$ in the specific model, from the system with one (three) state(s) occupied in the new band, corresponding to $t = 0.51$ (0.53); in this case, the gapless fermions from the occupied large band contribute as a $c = 1$ field. As seen in Fig. 4.7, ΔS_1 for $n = 1$ is nearly identical to the corresponding entanglement entropy for the Lifshitz transition for free fermions with two different lattice sizes. For $n = 3$, the value of ΔS_1 decreases slightly as the length of the system decreases, but the qualitative features remain the same. Note that in these data, only the total length of the system was scaled to unity.

The above results provide strong evidence that the dimer model can be viewed as two approximately independent systems: a background $c = 1$ boson corresponding to the resonance between the dimers (both blue and green (Patel et al., 2016)), and a dilute gas (of density p) of free fermions. These are precisely the characteristics of the FL* state, which has an emergent gauge field (represented here by the $c = 1$ boson) and a Fermi surface of electron-like quasiparticles.

4.5   Outlook

The combination of our results on the density distribution and the entanglement entropy confirm the expected appearance of a FL* state in the dimer model of Punk et al. (2015). By general arguments (Senthil et al., 2004; Paramekanti and Vishwanath, 2004), the violation of the Luttinger theorem for a Fermi liquid requires that the emergent gauge fields appear in the spectrum of the theory. Our results on the entanglement entropy in a quasi-one-dimensional geometry are in accord with this requirement, showing a background $c = 1$ boson that is expected from the gauge theory of the dimer model (Fradkin and Kivelson, 1990; Read and Sachdev, 1990); the boson represents the modes associated with the "resonance" between the dimers around a plaquette. Above this gauge field background, we obtained evidence for a gas of nearly-free fermions of density p, both in the density modulations and in the entanglement entropy: in particular, the fermionic contribution to the entanglement

entropy closely matched that of a dilute gas of free fermions near the bottom of a quadratically dispersing band.

One possible direction to extend our work is to use the infinite-DMRG (iDMRG). By using iDMRG we will be able to compute correlation functions of all length scales, and can obtain momentum distribution and quasiparticle residue of Fermionic dimers. Still, our momentum resolution in k_y will be restricted by N_y.

Another approach is to use the recent proposal of DMRG in mixed real and momentum space (Motruk et al., 2016). By this method we will be able to determine k_y more directly, which can be evidence of the existence of the hole pockets. Moreover, Motruk et al. (2016) claims the computation time is reduced by more than an order of magnitude, so this may allow us to include more sites in y-direction (in this case, equivalently, more k_y points).

Chapter 5

Quantum criticality of reconstructing Fermi surfaces

5.1 Introduction

Quantum phase transitions between two Fermi liquids, one of which spontaneously breaks translational symmetry and so reconstructs its Fermi surface, have been of longstanding theoretical and experimental interest. Important new examples of experimental realizations have emerged in the past years, (Taillefer, 2010; Helm et al., 2010; Nakai et al., 2010; Doiron-Leyraud and Taillefer, 2012) and so a full theoretical understanding is of some urgency. Next to immediate relevance for a class of strongly correlated electron materials, the spin-fermion model has evolved into a minimal model for itinerant lattice electrons with strong, commensurate magnetic fluctuations that are believed to destroy the Fermi liquid behavior when tuned to the critical point. How the compressible electron liquid, without Lorentz symmetry and without particle-hole symmetry, behaves when its correlations become singular, could provide some direction in the search for new universality classes beyond, for example, the better-known Gross-Neveu model of Dirac fermions which enjoys more symmetries. However, despite several decades of theoretical work, key questions remain open especially in the important case of two spatial dimensions.

Early theories (Overhauser, 1962; Hertz, 1976; Millis, 1993; Sachdev et al., 1995; Abanov et al., 2003; Moriya, 2012) for such quantum phase transitions focused on effective models for the quantum fluctuations of the order parameter, while treating the Fermi surface reconstruction as an ancillary phenomenon. However, it has since become clear (Abanov and Chubukov, 2000, 2004) that such an approach is inadequate, and the Fermi surface excitations are primary actors in the critical theory. Metlitski and Sachdev (2010b) postulated a critical theory for Fermi surface reconstruction, in which the Fermi surface excitations and the bosonic order parameter were equally important and both acquired anomalous dimensions. These excitations were strongly coupled to each other by a "Yukawa" coupling of universal strength, and their correlators scaled with a common dynamic critical exponent, z. Explicit computations were performed in the context of a $1/N$ expansion, where the physical number of fermion flavors is generalized to N. Taking N large, one can formally reorganize Wick's theorem in powers of $1/N$ and then extrapolate results to the physical number of fermion flavors. For the hot-spot field theory at the onset of spin-density wave order, no such critical theory appeared at the two-loop level. Indeed, it was pointed out that at higher loops (Lee, 2009; Metlitski and Sachdev, 2010a,b) there is a breakdown of the $1/N$ expansion, and so it remained unclear whether the postulated fixed point existed.

Here we address the problem of Fermi surface reconstruction at the onset of spin-density wave order by an analysis based on a formally exact functional renormalization group (fRG) approach. (Berges et al., 2002; Metzner et al., 2012) This RG approach allows a computation of correlation function as a function of a continuous cutoff scale Λ; from the "UV" at energies of the order of the bandwidth down to "infrared" excitations at and in the vicinity of the Fermi surface. Nonuniversal quantities and crossover scales can be extracted from the same solution which also yields the critical exponents in the limit $\Lambda \to 0$. Combined with the potential to resolve the momentum (and frequency) dependence or correlators along the Fermi surface, the fRG offers much more than the field theoretic RG or conventional ϵ expansion which is typically used to extract the leading singularities only.

In this chapter, we solve a set of coupled flow equations which treats the electrons on equal footing to the collective, order-parameter fluctuations. We truncate the flow equations to a set of discrete points on the Fermi surface. When projecting our correlators onto the hot spot as a function of momenta, we establish the existence of a fixed point with the scaling structure postulated in Metlitski and Sachdev (2010b), describing the quantum phase transition between two Fermi liquids: from the metal with preserved SU(2) spin symmetry to the metallic antiferromagnet which spontaneously breaks spin symmetry. A significant feature of our truncation is that it ties the parameters controlling the order parameter fluctuations to those associated with the fermion excitations, and this is important for a proper description of the scaling structure. We present numerical estimates for the critical exponents of the boson and fermion spectral functions, and for the variation in the fermionic quasiparticle residue around the Fermi surface. During our computations, we keep the shape of the Fermi surface fixed. In principle, one would have to allow for a flowing Fermi surface and consequently a flowing hot spot. In such a truncation, the singular manifold becomes a "moving target" and this significantly complicates the analysis.

The rest of our results are presented in Chapter 5.5. In Chapter 5.2, we introduce the recently developed two-band spin-fermion model that has the additional appealing feature that it does not suffer from the sign problem in quantum Monte Carlo simulations. (Berg et al., 2012) In Chapter 5.3, we present the functional RG setup, the truncation, and the cutoff functions. In Chapter 5.6, we conclude and suggest interesting future directions resulting from this chapter.

5.2   Model

Our computation will be carried in the context of the "spin-fermion" model of antiferromagnetic fluctuations in a Fermi liquid. (Abanov et al., 2003) This involves a spin-density wave order parameter $\vec{\phi}$ at wave vector $\mathbf{K} = (\pi, \pi)$ coupled to fermions Ψ moving on a square lattice. The analytic analyses have focused on the vicinity of the "hot spots" on the Fermi surface: These are the eight points on the Fermi surface

which can generically be connected to each other by $\mathbf{K}$. The fermion dispersions were linearized and truncated around the hot spots. However a complete analysis requires that we avoid the spurious singularities associated with truncated Fermi surfaces and deal only with continuous Fermi surfaces. Here, we choose the Fermi surface configurations of a recent analysis (Berg et al., 2012) which allowed Monte Carlo studies without a sign problem. The present work may be seen as complementary to Berg et al. (2012): Here we especially focus on the universality class and critical properties. This paves the way for an eventual comparison of our renormalization group results with Monte Carlo. Our present method applies also to general Fermi surfaces and provides access to real-time spectral functions which are not easily obtainable from imaginary-time Monte Carlo.

The model of Berg et al. (2012) contains fermions in two bands, or two flavors, Ψ_α, $\alpha = 1, 2$ (although our present method can also be applied to single band models), coupled to $\vec{\phi}$ in the effective action

$$
\begin{aligned}
\Gamma^{\Lambda_{\mathrm{UV}}}\left[\bar{\psi}, \psi, \vec{\phi}\right] = &\int_k \sum_{\alpha=1,2} \overline{\Psi}_\alpha(k) \begin{pmatrix} -ik_0 + \xi_{\mathbf{k},\alpha} & 0 \\ 0 & -ik_0 + \xi_{\mathbf{k},\alpha} \end{pmatrix} \Psi_\alpha(k) \\
&+ \int_q \frac{1}{2} \vec{\phi}(-q) \left(\mathbf{q}^2 + r\right) \vec{\phi}(q) \\
&+ \int_{k,q} \lambda \vec{\phi}(q) \left(\overline{\Psi}_1(k+q)\vec{\sigma}\,\Psi_2(k) + \overline{\Psi}_2(k+q)\vec{\sigma}\Psi_1(k)\right),
\end{aligned}
\tag{5.1}
$$

where $\int_k$ represents integrals over spatial momenta $\mathbf{k} = (k_x, k_y)$ over the Brillouin zone, and frequencies k_0. The fermion spinors are defined by $\overline{\Psi}_\alpha(k) = \left(\bar{\psi}_{\alpha,\uparrow}(k)\ \bar{\psi}_{\alpha,\downarrow}(k)\right)$, $\alpha = 1, 2$. We already introduce here the cutoff Λ along which we later integrate our renormalization group flow toward $\Lambda \to 0$. With $\Lambda = \Lambda_{\mathrm{UV}}$ we have the bare lattice action. The boson quadratic term consists of the control parameter r and a spatial gradient squared to account for spatial variations of the order parameter field $\vec{\phi}$. The quantum dynamics of $\vec{\phi}$ will be generated in the RG flow; putting a q_0^2 term into Eq. (5.1) does not change our results. The fermion dispersions for nearest-neighbor hopping are

$$
\xi_{\mathbf{k},\alpha} = -2t_{\alpha,x}\cos k_x - 2t_{\alpha,y}\cos k_y - \mu_\alpha.
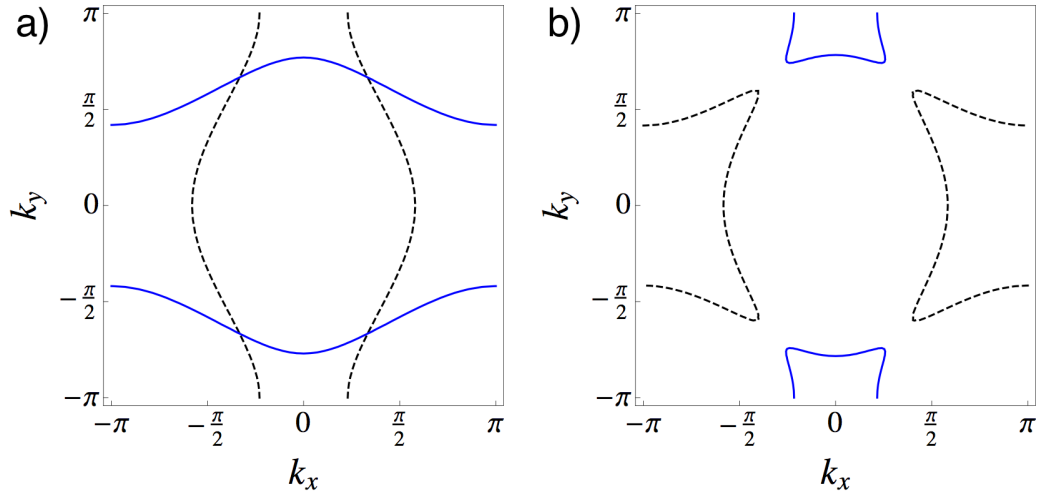\tag{5.2}
$$

Figure 5.1: Reconstructing Fermi surfaces ($\xi_{\mathbf{k},1} = 0$, black dashed line; $\xi_{\mathbf{k},2} = 0$, blue solid line for Eq. (5.2)) from the paramagnetic phase (a) to the zeros of the quasiparticle energies in the antiferromagnetic (SDW) phase (b). Gaps open at the "hot spots," that is, where the Fermi surfaces of the two flavors intersect. In this chapter, we focus on the SDW transition that is the singular point right when the Fermi surfaces reconstruct. The C_4 lattice symmetry of the original fermions is preserved.

A consistent mapping to "physical" fermions can be achieved with an anisotropic choice of hoppings, (Berg et al., 2012) $t_> = 1$, $t_< = 0.5$, $\mu_\alpha = -0.5$, and $t_{1,x} = t_>$, $t_{2,x} = -t_<$, $t_{1,y} = t_<$, $t_{2,y} = -t_>$ yielding the Fermi surfaces shown in Fig. 5.1. An important distinction of this chapter compared to the previous work (Altshuler et al. (1995); Abanov and Chubukov (2000, 2004); Abanov et al. (2003); Lee (2009); Metlitski and Sachdev (2010a,b)) is that we do not truncate the Fermi surface as patch models around hot spots.

A mean-field analysis of Eq. (5.1) predicts an antiferromagnetic spin-density wave (SDW) ground state at $r = 1.34$ which spontaneously breaks the spin SU(2) symmetry of Eq. (5.1). The Fermi surface topology "reconstructs" and gaps open at the hot spots, as shown in Fig. 5.1. On a mean-field level, the SDW transition at zero temperature of Eq. (5.1) is first order, as was also found in related single-band models for electronic antiferromagnets. (Altshuler et al., 1995; Reiss et al., 2007) At present, it is not clear which effects such as fluctuations or competing instabilities could potentially drive the transitions continuous or even change the ground state.

The same is true for the formation of SDWs with periods incommensurate with the underlying lattice. In the present chapter, we ignore these complications and focus our attention on continuous SDW transitions at zero temperature.

5.3 Functional Renormalization Group

Our RG analysis is based on the (formally exact) flow equation for the effective action $\Gamma_R^\Lambda \left[\bar\psi, \psi, \vec\phi \right]$, the generating functional for one-particle irreducible correlation functions in the form derived by Wetterich. (Berges et al., 2002; Metzner et al., 2012) The regulator R introduces a cutoff dependence into the effective action so that Γ_R^Λ smoothly interpolates between the bare action, Eq. (5.1), at the ultraviolet scale $\Gamma_R^{\Lambda = \Lambda_{\mathrm{UV}}} \left[\bar\psi, \psi, \vec\phi \right] = \Gamma^{\Lambda_{\mathrm{UV}}} \left[\bar\psi, \psi, \vec\phi \right]$ and the fully renormalized effective action in the limit of vanishing cutoff: $\lim_{\Lambda \to 0} \Gamma_R^\Lambda \left[\bar\psi, \psi, \vec\phi \right] = \Gamma \left[\bar\psi, \psi, \vec\phi \right]$. The Wetterich equation has a one-loop structure and in a vertex expansion the β functions for the n-point correlators are determined by (cutoff derivatives of) one-particle irreducible one-loop diagrams with fully dressed propagators and vertices. Upon self-consistent integration of the coupled set of β functions, contributions of arbitrary high loop order are generated. As we explain below, we truncate the effective action to the full fermion two-point function (including a fermion self-energy $\Sigma_f^\Lambda(k_0, \mathbf{k})$), the full bosonic two-point function (including a bosonic self-energy $\Sigma_b^\Lambda(q_0, \mathbf{q})$), and the Yukawa coupling λ^Λ.

Our results are obtained from the renormalization group flow of the action Eq. (5.1) at the quantum-critical point ($r = 0$) under the formally exact evolution equation (Metzner et al., 2012)

$$\frac{d}{d\Lambda} \Gamma_R^\Lambda \left[\chi, \bar\chi \right] = \frac{1}{2} \mathrm{Str} \left\{ \dot{R}^\Lambda \left[\Gamma_R^{(2)\Lambda} \left[\chi, \bar\chi \right] + R^\Lambda \right]^{-1} \right\} . \tag{5.3}$$

$\Gamma_R^{(2)\Lambda}$ is the second derivative with respect to the fields defined below. R^Λ is a matrix containing Λ-dependent cutoff functions that regularizes the infrared singularities of the fermion and boson propagators. The dot is shorthand notation for a scale derivative $\dot{R}^\Lambda = \partial_\Lambda R^\Lambda$. Both sides of this equation are projected onto a "super"-field

basis χ, $\bar{\chi}$ containing fermionic and bosonic entries:

$$\chi(k) = \begin{pmatrix} \phi_x(k) \\ \phi_y(k) \\ \phi_z(k) \\ \psi_{1,\uparrow}(k) \\ \psi_{1,\downarrow}(k) \\ \bar{\psi}_{1,\uparrow}(k) \\ \bar{\psi}_{1,\downarrow}(k) \\ \psi_{2,\uparrow}(k) \\ \psi_{2,\downarrow}(k) \\ \bar{\psi}_{2,\uparrow}(k) \\ \bar{\psi}_{2,\downarrow}(k) \end{pmatrix} \tag{5.4}$$

and its conjugate-transposed $\bar{\chi}(k)$. Str is a "super" trace over frequency, momenta, and internal indices and installs an additional factor of -1 for contributions from the purely fermionic sector of the trace of Grassmann-valued matrices. We solve Eq. (5.3) in a vertex expansion truncating any generated vertices beyond the Yukawa vertex. The flowing fermion self-energy $\Sigma_f^\Lambda(k_0, \mathbf{k})$ and the boson self-energy $\Sigma_b^\Lambda(q_0, \mathbf{q})$ are parametrized in a derivative expansion keeping the Fermi surfaces fixed.

The cutoff matrix in Eq. (5.3) is given by

$$R^\Lambda = \mathrm{diag}\Big(R_{b,x}^{\Lambda_b}, R_{b,y}^{\Lambda_b}, R_{b,z}^{\Lambda_b}, R_{f1,\uparrow}^{\Lambda_f}, R_{f1,\downarrow}^{\Lambda_f}, -R_{f1,\uparrow}^{\Lambda_f}, -R_{f1,\downarrow}^{\Lambda_f}, R_{f2,\uparrow}^{\Lambda_f}, R_{f2,\downarrow}^{\Lambda_f}, -R_{f2,\uparrow}^{\Lambda_f}, -R_{f2,\downarrow}^{\Lambda_f} \Big),$$
$$\tag{5.5}$$

where one is, in principle, free to choose the fermion and boson cutoff scales Λ_b and Λ_f and associated regulator functions $R_{b,f}$ independently. (Schütz et al., 2005; Drukier et al., 2012) The corresponding "flow trajectories" in cutoff space (in the plane of Fig. 5.2) from the bare action (red dot) to renormalized, effective action (green dot) will be different. We choose the trajectory along the arrows illustrated in Fig. 5.2; that is, we take $\Lambda_f \to 0$ and $R_f \to 0$ before integrating out order parameter fluctuations which are excluded for momenta smaller than Λ_b. The fermions are, however, not discarded as in the Hertz theory, (Hertz, 1976) but coupled self-consistently into the
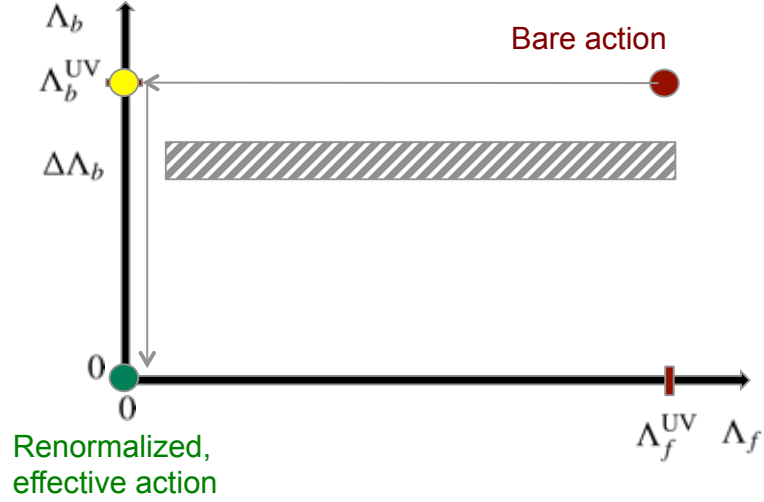
Figure 5.2: Illustrative flow trajectory in cutoff space. At each step $\Delta\Lambda_b$ of the integration over bosonic momenta along the vertical axis the entire range of fermionic momenta is swept over (gray-striped box).

flow for all $\Lambda \in \{\Lambda_b^{\mathrm{UV}}, 0\}$, thereby imposing important boundary conditions for the integration of order parameter fluctuations down the vertical axis in Fig. 5.2. This makes the flow nonlocal in the cutoff scale in that the purely fermionic contractions with Yukawa vertices are treated as a total scale derivative that also acts on the self-energy on the internal lines and the Yukawa vertices. This is similar in spirit to the Katanin scheme, where this can be shown to lead to the inclusion of higher n-point vertices in the flow. (Salmhofer et al., 2004)

For the bosons, we use a Litim cutoff for momenta,

$$R_{b,x}^{\Lambda_b} = R_{b,y}^{\Lambda_b} = R_{b,z}^{\Lambda_b} = R_b^\Lambda = A_b^\Lambda \left(-\mathbf{q}^2 + \Lambda^2\right) \theta \left(\Lambda^2 - \mathbf{q}^2\right) \ , \tag{5.6}$$

where A_b^Λ is bosonic momentum renormalization factor to be specified below. In the following, we set $\Lambda^b = \Lambda$. The fermionic entries in Eq. (5.5) are zero.

The fermionic matrix elements of the generalized matrix propagator $\left[\Gamma_R^{(2)\Lambda}\left[\chi, \bar{\chi}\right] + R^\Lambda\right]^{-1}$

occurring in Eq. (5.3) become

$$G^\Lambda_{f1,\sigma}(k) = -\langle \psi_{1,\sigma}(k) \bar{\psi}_{1,\sigma}(k) \rangle^R$$

$$= -\left[\frac{\overrightarrow{\delta}}{\delta \overline{\chi}(k_1)} \Gamma^\Lambda_R[\chi, \overline{\chi}] \frac{\overleftarrow{\delta}}{\delta \chi(k_2)} + R^\Lambda \right]^{-1}_{\substack{f1,\sigma \\ \overline{\chi}=\chi=0 \\ k_1=k_2=k}}$$

$$= \frac{-1}{-ik_0 + \xi_{\mathbf{k},1} + \Sigma^\Lambda_{f1}(k_0, \mathbf{k})} \, , \tag{5.7}$$

and analogously for the other flavor and spin components.

The explicitly cutoff-dependent boson spin fluctuation propagators are

$$D^R(q) \equiv D^R_x(q) = -\langle \phi_x(q) \phi_x(-q) \rangle^R$$

$$= -\left[\frac{\overrightarrow{\delta}}{\delta \overline{\chi}(q_1)} \Gamma^\Lambda_R[\chi, \overline{\chi}] \frac{\overleftarrow{\delta}}{\delta \chi(q_2)} + R^\Lambda \right]^{-1}_{\substack{b,x \\ \overline{\chi}=\chi=0 \\ q_1=q_2=q}}$$

$$= \frac{-1}{\mathbf{q}^2 + r + \Sigma^\Lambda_b(q_0, \mathbf{q}) + R^\Lambda_b}$$

$$= \begin{cases} \frac{-1}{\mathbf{q}^2 + r + \Sigma^\Lambda_b(q_0, \mathbf{q})} & |\mathbf{q}| > \Lambda \\ \frac{-1}{\Lambda^2 + r + \Sigma^\Lambda_b(q_0, \Lambda)} & |\mathbf{q}| < \Lambda \end{cases} \, , \tag{5.8}$$

and analogously for the other spin projections y, z. The functional derivatives are evaluated at zero fields here, as we approach the QCP from the paramagnetic phase.

The flow equation for the fermion self-energy (depicted diagrammatically in Fig. 5.3(a)) is

$$\partial_\Lambda \Sigma^\Lambda_{f1}[k_0, \mathbf{k}] = 3 \left(\lambda^\Lambda \right)^2 \int_{q,R} G^\Lambda_{f2}(k+q) D^R_b(q) \, , \tag{5.9}$$

and similarly for flavor 2 upon interchanging $1 \leftrightarrow 2$. We use a shorthand notation encapsulating frequency, momentum integrations, and a cutoff derivative with respect to the bosonic cutoff function: $\int_{q,R_b} = \int \frac{dq_0}{2\pi} \int \frac{d^2\mathbf{q}}{(2\pi)^2} \left[-\dot{R}^\Lambda_b \partial_{R^\Lambda_b} \right]$.

The prefactors and signs of the flow equations are computed by comparing coefficients between the left- and right-hand sides of Eq. (5.3) as outlined in Sec.II of Gies and Wetterich (2002). The 11×11 Grassmann-valued (super-) matrices are evaluated
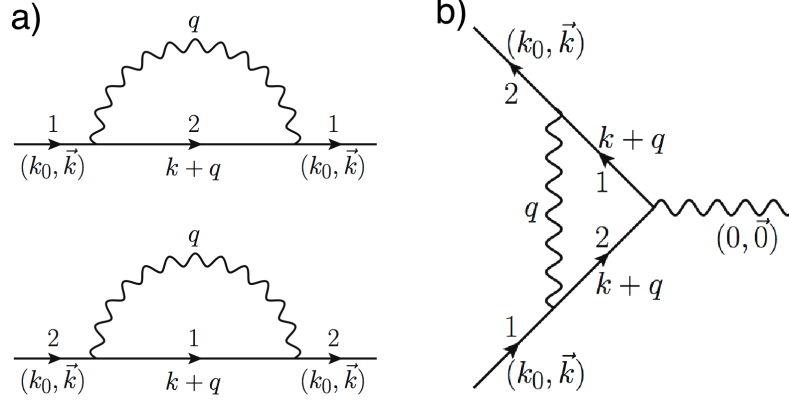
Figure 5.3: Diagrammatic representation of the flow equation for the fermion self-energy $\Sigma_f^\Lambda(k_0, \mathbf{k})$ (a) and the Yukawa coupling (b). Straight lines denote Fermi propagators of flavors 1 and 2; wiggly line boson propagators are endowed with a regulator R^Λ. Intersections of wiggly with straight lines represent the Yukawa coupling. The cutoff derivative with respect to R^Λ is implicit. All propagators and vertices are "dressed" self-consistently and are functions of Λ.

using the GrassmannOps.m package in Mathematica. How to take a supertrace can be found in Wegner (1998).

The boson self-energy is determined self-consistently from the particle-hole bubble (Fig. 5.4) at all stages of the flow:

$$\Sigma_b^\Lambda(q_0, \mathbf{q}) = -\left(\Pi^\Lambda(q_0, \mathbf{q}) - \Pi^\Lambda(0, \mathbf{0})\right) \tag{5.10}$$

$$= 2\left(\lambda^\Lambda\right)^2 \int_k \left[\left(G_{f1}^\Lambda(k+q) - G_{f1}^\Lambda(k)\right) G_{f2}^\Lambda(k)\right.$$
$$\left. + G_{f1}^\Lambda(k)\left(G_{f2}^\Lambda(k+q) - G_{f2}^\Lambda(k)\right)\right].$$

The following ansatz captures the leading frequency and momentum-dependence of the particle-hole bubble:

$$\Sigma_b^\Lambda(q_0, \mathbf{q}) = Z_b^\Lambda |q_0| + (A_b^\Lambda - 1)\mathbf{q}^2 . \tag{5.11}$$

At the yellow dot in Fig. 5.2, the Fermi propagators are still Fermi-liquid like ($\Sigma_{f\alpha}^{\Lambda_{UV}} = 0$) because we have not yet integrated out any order parameter fluctuations which, by Fig. 5.3(a), generate a finite fermion self-energy. At that point, the coefficients $Z_b^{\Lambda_{UV}}$, $A_b^{\Lambda_{UV}}$ take finite numerical values. At all stages of the flow, when integrating
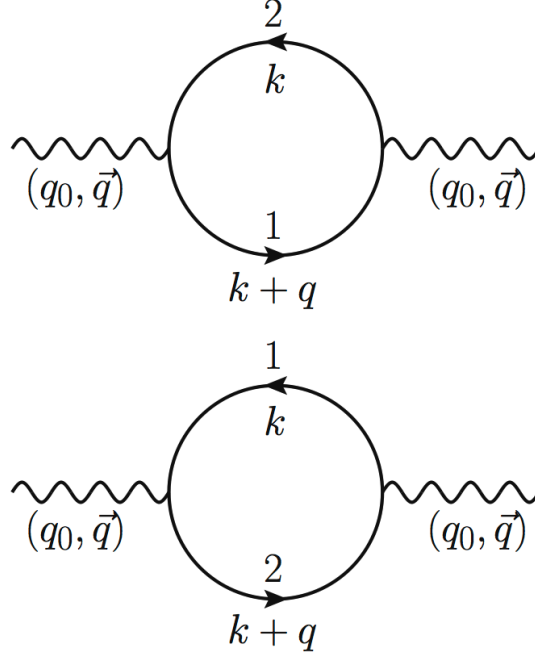
Figure 5.4: Particle-hole bubbles used for the flow of the boson self-energy in Eq. (5.11). All propagators and vertices are "dressed" self-consistently and depend on Λ.

the flow down the vertical axis of Fig. 5.2, the bosonic Z and A factor are determined self-consistently according to the prescription

$$Z_b^{\Lambda} = -\frac{\Pi^{\Lambda}(q_0, \mathbf{0}) - \Pi^{\Lambda}(0, \mathbf{0})}{q_0}\Bigg|_{q_0=\Lambda},$$

$$A_b^{\Lambda} = 1 - \frac{\Pi^{\Lambda}(0, \mathbf{q}) - \Pi^{\Lambda}(0, \mathbf{0})}{\mathbf{q}^2}\Bigg|_{q_x=\Lambda, q_y=0}. \tag{5.12}$$

This allows them to pick up potentially singular renormalizations during the flow. The boson momentum factor is isotropic in momentum space; interchanging $q_x \leftrightarrow q_y$ delivers the same value for A_b^{Λ}.

The flow equation as per Fig. 5.3(b) for the Yukawa coupling is

$$\partial_{\Lambda}\lambda^{\Lambda} = -\left(\lambda^{\Lambda}\right)^3 \int_{q,R} G_{f1}^{\Lambda}(k+q)G_{f2}^{\Lambda}(k+q)D_b^R(q)\Bigg|_{k_0=0, \mathbf{k}=\mathbf{k}_{\mathrm{HS}}}. \tag{5.13}$$

The explicit expressions of the flow equations and the numerical parameter used are given in the next chapter.

5.4 Explicit form of flow equations

We here give the explicit expressions of the flow equations (5.9), (5.10), (5.13). To that end, it is convenient to use the rescaled variables $\tilde{Z}_b^\Lambda = \frac{Z_b^\Lambda}{\Lambda}$, $\tilde{\xi}_{\mathbf{k},1} = \frac{\xi_{\mathbf{k},1}}{\Lambda}$ as well as rescaled momenta: $\tilde{k}_0 = \frac{k_0}{\Lambda}$, $\tilde{q}_0 = \frac{q_0}{\Lambda}$, $\tilde{q}_x = \frac{q_x}{\Lambda}$, and $\tilde{q}_y = \frac{q_y}{\Lambda}$.

For the the fermionic frequency exponent, there is

$$
\eta_{Z_{f1}} = 3\left(\tilde{\lambda}^\Lambda\right)^2 \sqrt{|v_{f1}^\Lambda|\,|v_{f2}^\Lambda|} \int_{-1}^{1} \frac{d\tilde{q}_y}{2\pi} \int_{-\sqrt{1-\tilde{q}_y^2}}^{+\sqrt{1-\tilde{q}_y^2}} \frac{d\tilde{q}_x}{2\pi} \int_{-\infty}^{\infty} \frac{d\tilde{q}_0}{2\pi}
$$

$$
\times \left[2A_b^\Lambda \frac{1}{\left(i\tilde{q}_0 - |v_{f2}^\Lambda|\tilde{\xi}_{\mathbf{k}_{\mathrm{HS}}+\tilde{\mathbf{q}},2}\right)^2} \frac{1}{\left(\tilde{Z}_b^\Lambda|\tilde{q}_0| + A_b^\Lambda\right)^2} \right], \tag{5.14}
$$

and similarly $(1 \leftrightarrow 2)$ for flavor 2. The frequency integral over $\tilde{q}_0$ can be performed analytically so that at each step of the flow, two-dimensional integrations over $\tilde{q}_x$ and $\tilde{q}_y$ have to be performed numerically. The Yukawa anomalous exponent contains fermion propagators of both flavors:

$$
\eta_{\mathrm{yuk}} = -\left(\tilde{\lambda}^\Lambda\right)^2 \sqrt{|v_{f1}^\Lambda|\,|v_{f2}^\Lambda|} \int_{-1}^{1} \frac{d\tilde{q}_y}{2\pi} \int_{-\sqrt{1-\tilde{q}_y^2}}^{+\sqrt{1-\tilde{q}_y^2}} \frac{d\tilde{q}_x}{2\pi} \int_{-\infty}^{\infty} \frac{d\tilde{q}_0}{2\pi}
$$

$$
\times \left[2A_b^\Lambda \frac{1}{i\tilde{q}_0 - |v_{f1}^\Lambda|\tilde{\xi}_{\mathbf{k}_{\mathrm{HS}}+\tilde{\mathbf{q}},1}} \frac{1}{i\tilde{q}_0 - |v_{f2}^\Lambda|\tilde{\xi}_{\mathbf{k}_{\mathrm{HS}}+\tilde{\mathbf{q}},2}} \frac{1}{\left(\tilde{Z}_b^\Lambda|\tilde{q}_0| + A_b^\Lambda\right)^2} \right]. \tag{5.15}
$$

For the flow of the fermionic momentum factors we use the projected k_x and k_y derivatives of Eq. (5.9),

$$
\partial_\Lambda A_{f1,x}^\Lambda = n_{k_x,1}\partial_{k_x}\partial_\Lambda \Sigma_{f1}^\Lambda[k_0,\mathbf{k}]\Big|_{k_0=0,\mathbf{k}=\mathbf{k}_{\mathrm{HS}}},
$$

$$
\partial_\Lambda A_{f1,y}^\Lambda = n_{k_y,1}\partial_{k_y}\partial_\Lambda \Sigma_{f1}^\Lambda[k_0,\mathbf{k}]\Big|_{k_0=0,\mathbf{k}=\mathbf{k}_{\mathrm{HS}}}, \tag{5.16}
$$

with the initial conditions $A_{f1,x}^{\Lambda^{\mathrm{UV}}} = A_{f1,y}^{\Lambda^{\mathrm{UV}}} = 1$. The Fermi surface normal projector is (similarly for flavor 2)

$$
n_{k_{x/y},1} = \frac{2t_{1,x/y}\mathrm{sin}k_{x/y}}{\sqrt{\left(2t_{1,x}\mathrm{sin}k_{x/y}\right)^2 + \left(2t_{1,y}\mathrm{sin}k_y\right)^2}}. \tag{5.17}
$$

The flow equations for the rescaled variables are $\tilde{A}^\Lambda_{f1,x} = \frac{A^\Lambda_{f1,x}}{Z^\Lambda_{f1}}$, $\tilde{A}^\Lambda_{f1,y} = \frac{A^\Lambda_{f1,y}}{Z^\Lambda_{f1}}$. With $\eta_{Z_{f1}}$ given in Eq. (5.14), these take the form

$$\Lambda\partial_\Lambda \tilde{A}^\Lambda_{f1,x} = \left(\eta_{Z_{f1}} - \eta_{A_{f1,x}}\right) \tilde{A}^\Lambda_{f1,x},$$
$$\Lambda\partial_\Lambda \tilde{A}^\Lambda_{f1,y} = \left(\eta_{Z_{f1}} - \eta_{A_{f1,y}}\right) \tilde{A}^\Lambda_{f1,y}, \tag{5.18}$$

with the exponents $\eta_{A_{f1,x}} = -\frac{d\ln A^\Lambda_{f1,x}}{d\ln\Lambda}$, $\eta_{A_{f1,y}} = -\frac{d\ln A^\Lambda_{f1,y}}{d\ln\Lambda}$. At every step of the flow, we compute then per Eq. (5.25)

$$|v^\Lambda_{f1}| = \frac{\sqrt{\left(\tilde{A}^\Lambda_{f1,x}\right)^2 + \left(\tilde{A}^\Lambda_{f1,y}\right)^2}}{|\nabla\xi_{1,\mathbf{k}}|_{\mathbf{k}=\mathbf{k}_{\mathrm{HS}}}}. \tag{5.19}$$

Expressions for the exponents:

$$\eta_{A_{f1,x}} = - n_{k_{\mathrm{HS,x}},1}\, 3\left(\tilde{\lambda}^\Lambda\right)^2 \sqrt{|v^\Lambda_{f1}||v^\Lambda_{f2}|}\frac{|v^\Lambda_{f2}|}{\tilde{A}_{f1,x}}$$
$$\times \int_{-1}^{1}\frac{d\tilde{q}_y}{2\pi}\int_{-\sqrt{1-\tilde{q}_y^2}}^{+\sqrt{1-\tilde{q}_y^2}}\frac{d\tilde{q}_x}{2\pi}\int_{-\infty}^{\infty}\frac{d\tilde{q}_0}{2\pi}2A^\Lambda_b\frac{2t_{2x}\sin\left(k_{\mathrm{HS,x}}+\tilde{q}_x\Lambda\right)}{\left(i\tilde{q}_0 - |v^\Lambda_{f2}||\tilde{\xi}_{\mathbf{k}_{\mathrm{HS}}+\tilde{\mathbf{q}},2}\right)^2}\frac{1}{\left(\tilde{Z}^\Lambda_b|\tilde{q}_0| + A^\Lambda_b\right)^2},$$

$$\eta_{A_{f1,y}} = - n_{k_{\mathrm{HS,y}},1}\, 3\left(\tilde{\lambda}^\Lambda\right)^2 \sqrt{|v^\Lambda_{f1}||v^\Lambda_{f2}|}\frac{|v^\Lambda_{f1}|}{\tilde{A}_{f1,y}}$$
$$\times \int_{-1}^{1}\frac{d\tilde{q}_y}{2\pi}\int_{-\sqrt{1-\tilde{q}_y^2}}^{+\sqrt{1-\tilde{q}_y^2}}\frac{d\tilde{q}_x}{2\pi}\int_{-\infty}^{\infty}\frac{d\tilde{q}_0}{2\pi}2A^\Lambda_b\frac{2t_{2y}\sin\left(k_{\mathrm{HS,y}}+\tilde{q}_y\Lambda\right)}{\left(i\tilde{q}_0 - |v^\Lambda_{f2}||\tilde{\xi}_{\mathbf{k}_{\mathrm{HS}}+\tilde{\mathbf{q}},2}\right)^2}\frac{1}{\left(\tilde{Z}^\Lambda_b|\tilde{q}_0| + A^\Lambda_b\right)^2}. \tag{5.20}$$

Finally, the (rescaled) boson frequency factor and momentum factor are self-consistently determined from

$$\tilde{Z}^\Lambda_b = 2\left(\tilde{\lambda}^\Lambda\right)^2 \sqrt{|v^\Lambda_{f1}||v^\Lambda_{f2}|}\int_{-\pi}^{\pi}\frac{dk_x}{2\pi}\int_{-\pi}^{\pi}\frac{dk_y}{2\pi}\frac{1}{\Lambda^2}$$
$$\times \int_{-\infty}^{\infty}\frac{d\tilde{k}_0}{2\pi}\left[\left(\frac{1}{i(\tilde{k}_0+1) - |v^\Lambda_{f1}|\xi_{\mathbf{k},1}} - \frac{1}{i\tilde{k}_0 - |v^\Lambda_{f1}|\xi_{\mathbf{k},1}}\right)\frac{1}{i\tilde{k}_0 - |v^\Lambda_{f2}|\xi_{\mathbf{k},2}} + (1\leftrightarrow 2)\right],$$
$$\tilde{A}^\Lambda_b = 2\left(\tilde{\lambda}^\Lambda\right)^2 \sqrt{|v^\Lambda_{f1}||v^\Lambda_{f2}|}\int_{-\pi}^{\pi}\frac{dk_x}{2\pi}\int_{-\pi}^{\pi}\frac{dk_y}{2\pi}\frac{1}{\Lambda^2}$$
$$\times \int_{-\infty}^{\infty}\frac{d\tilde{k}_0}{2\pi}\left[\left(\frac{1}{i\tilde{k}_0 - |v^\Lambda_{f1}|\xi_{\mathbf{k}+q_x,1}} - \frac{1}{i\tilde{k}_0 - |v^\Lambda_{f1}|\xi_{\mathbf{k},1}}\right)\frac{1}{i\tilde{k}_0 - |v^\Lambda_{f2}|\xi_{\mathbf{k},2}} + (1\leftrightarrow 2)\right]_{q_x=\Lambda}. \tag{5.21}$$

Equations (5.22), (5.14), (5.15), and (5.18)–(5.21) are solved numerically as a function of flow parameter $\Lambda = \Lambda^{\mathrm{UV}} e^{-s}$ so that $s = 0$ corresponds to the UV ($\Lambda^{\mathrm{UV}} = 1$). The hot spot coordinates are $k_{\mathrm{HS,x}} = 1.0472$, $k_{\mathrm{HS,y}} = 2.0944$. As initial conditions, we choose $\lambda^{\Lambda_{\mathrm{UV}}} = 0.25$, $Z_{f1}^{\Lambda_{\mathrm{UV}}} = Z_{f2}^{\Lambda_{\mathrm{UV}}} = 1$, and $A_{f1}^{\Lambda_{\mathrm{UV}}} = A_{f2}^{\Lambda_{\mathrm{UV}}} = 1$. The initial values for the boson propagator are $\tilde{Z}_b^{\Lambda_{\mathrm{UV}}} = 0.052$ and $\tilde{A}_b^{\Lambda_{\mathrm{UV}}} = 1.011$.

5.5   Results

We now describe the key results obtained from a solution of the flow equations. (i) We find an infrared strong-coupling fixed point for the Yukawa-coupling λ^Λ which governs the RG flow of the coupled Fermi-Bose action down to the lowest scales $\Lambda \to 0$. This induces scaling relations among the anomalous exponents for the Fermi velocity, the quasiparticle weight, and the Yukawa vertex. (ii) Both the quasiparticle weight and the Fermi velocity vanish as a power law when scaling the momenta toward the hot spot; the Fermi velocity slower than the quasiparticle weight. (iii) The (quantum) dynamical scaling of the electronic single-particle and collective spin fluctuations follows from an emergent dynamical exponent, attaining the same (fractional) value for both fermions and bosons.

The centerpiece of our analysis is the flow equation for the Yukawa coupling:

$$\Lambda \partial_\Lambda \tilde{\lambda}^\Lambda = \left(\frac{1}{4} \left(\eta_{Z_{f1}} + \eta_{Z_{f2}} + \eta_{A_{f1}} + \eta_{A_{f2}} \right) - \eta_{\mathrm{yuk}} - \frac{1}{2} \right) \tilde{\lambda}^\Lambda , \tag{5.22}$$

where $\left(\tilde{\lambda}^\Lambda \right)^2 = \left(\lambda^\Lambda \right)^2 / (\Lambda \sqrt{Z_{f1}^\Lambda Z_{f2}^\Lambda} \sqrt{A_{f1}^\Lambda A_{f2}^\Lambda})$ is rescaled by the frequency (Z_{f1}^Λ) and momentum (A_{f1}^Λ) derivatives of the fermion self-energy generated under the RG flow as per Fig. 5.3(a). The power-law divergences as well as all other nonuniversal contributions to the flow of the two fermion self-energy factors and the Yukawa coupling itself are absorbed into the anomalous exponents:

$$\eta_{Z_{f1}} = -\frac{d \ln Z_{f1}^\Lambda}{d \ln \Lambda} , \quad \eta_{A_{f1}} = -\frac{d \ln A_{f1}^\Lambda}{d \ln \Lambda} , \quad \eta_{\mathrm{yuk}} = -\frac{d \ln \lambda^\Lambda}{d \ln \Lambda} . \tag{5.23}$$

η_{yuk} is driven by the direct contribution to the flow of λ^Λ exhibited in Fig. 5.3(b). All couplings are projected to zero fermionic frequency, a discrete set of fermionic

momenta on the Fermi surfaces, and zero bosonic frequency and momenta. This is where the most singular renormalizations occur.

Specifically, the inverse quasi-particle weight is computed from the flowing self-energy by (Honerkamp and Salmhofer, 2003)

$$Z_{f1}^{\Lambda} = 1 - \frac{\partial}{\partial i k_0} \Sigma_{f1}^{\Lambda}(k_0, \mathbf{k})|_{k_0=0, \mathbf{k}=\mathbf{k}_F}, \qquad (5.24)$$

where $\mathbf{k}_F$ is a momentum on the Fermi surface and the initial condition is $Z_{f1}^{\Lambda^{UV}} = 1$. The momentum renormalization factor is obtained from a momentum gradient of the fermion self-energy,

$$A_{f1}^{\Lambda} = 1 + \frac{|\mathbf{n}_{\mathbf{k},1} \cdot \nabla \Sigma_{f1}^{\Lambda}(k_0, \mathbf{k})|}{|\nabla \xi_{\mathbf{k},1}|}\Bigg|_{k_0=0, \mathbf{k}=\mathbf{k}_F}, \qquad (5.25)$$

with the initial condition $A_{f1}^{\Lambda^{UV}} = 1$. Here, $\nabla = \left(\partial_{k_x}, \partial_{k_y}\right)$ and $\mathbf{n}_{\mathbf{k},1}$ is unit normal vector onto the Fermi surface of flavor 1. We see below that the momentum gradient scales differently than the frequency derivative at the quantum critical point. In a different context, for Fermi systems with van Hove singularities, this asymmetry was established to all orders in perturbation theory by Feldman and Salmhofer. (Feldman and Salmhofer, 2008) Necessary conditions to discover this are (i) the codimension of the Fermi surface manifold is greater than zero (it is zero in a one-dimensional Fermi systems) and (ii) one includes the additional, relevant transversal momentum direction parallel to the Fermi surface into the analysis.

With these definitions, the scale-dependent "dressed" fermion propagator which occurs self-consistently in all RG equations becomes

$$G_{f1}^{\Lambda}(k) = \frac{-1}{-ik_0 + \xi_{\mathbf{k},1} + \Sigma_{f1}^{\Lambda}(k_0, \mathbf{k})} = \frac{\mathcal{Z}_{f1}^{\Lambda}}{ik_0 - |v_{f1}^{\Lambda}|\xi_{\mathbf{k},1}}, \qquad (5.26)$$

with $\mathcal{Z}_{f1}^{\Lambda} = 1/Z_{f1}^{\Lambda}$ resembling the quasiparticle weight at low energies and the effective modulus of the Fermi velocity $|v_{f1}^{\Lambda}| = \frac{A_{f1}^{\Lambda}}{Z_{f1}^{\Lambda}}$.

A self-consistent numerical solution of the flow equations for the Yukawa vertex λ^{Λ}, the fermion self-energy $\Sigma_f^{\Lambda}(k_0, \mathbf{k})$, and the boson self-energy $\Sigma_b^{\Lambda}(q_0, \mathbf{q})$ is attracted toward an infrared strong-coupling fixed point. As can be read off from Fig. 5.5, the
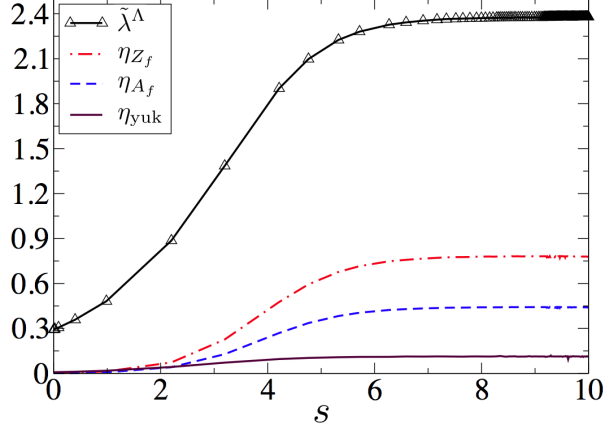
Figure 5.5: Quantum critical RG flows of the Yukawa coupling and the anomalous exponents at the hot spot $\mathbf{k}_{\text{HS}}$. The fixed-point values are $\tilde{\lambda}^{\Lambda} = 2.38$, $\eta_{Z_f} = 0.78$, $\eta_{A_f} = 0.44$, and $\eta_{\text{yuk}} = 0.11$. The scaling plateaus for $s \gtrsim 6$ depicted over ~ 4 orders of magnitude would be attained indefinitely but are limited by the numerics only. The infrared is to the right of the plot ($\Lambda = \Lambda_{\text{UV}} e^{-s}$).

β function for the Yukawa coupling, Eq. (5.22), vanishes for $s \gtrsim 6$, resulting in a scaling relation for the fermion and Yukawa anomalous exponents:

$$\frac{d \ln \tilde{\lambda}^{\Lambda}}{d \ln \Lambda} = 0 \quad \Leftrightarrow \quad \frac{1}{2}\left(\eta_{Z_f} + \eta_{A_f}\right) = \eta_{\text{yuk}} + \frac{1}{2} \; , \tag{5.27}$$

where we dropped the flavor index as they become degenerate at the hot spot. Similar strong-coupling fixed-point and scaling relations (without singular vertex corrections) have recently been obtained at the QCP of a Dirac cone toy model between a semimetal and a superfluid. (Strack et al., 2010; Obert et al., 2011)

The numerical values of the exponents (see Fig. 5.5) determine the scaling behavior of the fermion propagator, Eq. (5.26), and the associated dynamical exponent z_f. The Yukawa vertex diverges as a power law,

$$\lambda^{\Lambda \to 0} \sim \frac{1}{\Lambda^{\eta_{\text{yuk}}}} = \frac{1}{\Lambda^{0.11}} \; . \tag{5.28}$$

Λ can be associated with the momentum distance from the hot spot; at $\Lambda = 0$ the hot spots are resonantly connected by the ordering wave vector $\mathbf{K}$ of the incipient
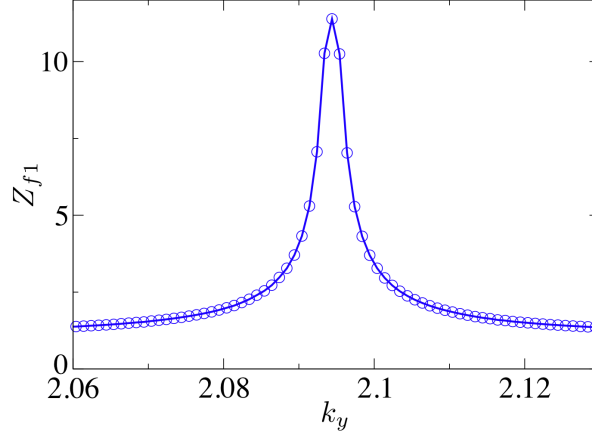
Figure 5.6: Infrared values of the momentum resolved inverse quasiparticle weights $Z_{f1}^{\Lambda \to 0}[k_0 = 0, k_x, k_y]$ non-self-consistently computed from Eq. (5.24) along the Fermi surface. Figure 5.7 exhibits flows of the corresponding exponents for the six data points closest to the maximum/hot spot on the right flank. Here the hot spot is located at $k_{\mathrm{HS},y} = 2.0944$ and $k_{\mathrm{HS},x} = 1.0472$.

SDW. At the hot spot, the fermionic quasiparticle weight vanishes as a power law,

$$\mathcal{Z}_f^{\Lambda \to 0} \sim \Lambda^{\eta_{Zf}} = \Lambda^{0.78}, \tag{5.29}$$

destroying the Fermi liquid character of fermionic quasiparticle excitations. In a non-self-consistent calculation we can also compute the fermion self-energy from Eq. (5.24) away from the hot spot by solving the flow equations evaluated at general fermionic momenta $\mathbf{k}$. The result for a momentum cut along the Fermi surface is exhibited in Fig. 5.6. The renormalization of the quasiparticle weight is strongly peaked around the intersection of the Fermi surfaces at the hotspot. Away from the hot spot, the suppression of the quasiparticle weight is less pronounced, leading to asymptotically vanishing anomalous exponents in the infrared $\Lambda \to 0$ (Fig. 5.7). Nevertheless, in the vicinity of the hot spot, magnetic fluctuations are still very strong, leading to sizable non-Fermi liquid scaling regimes at intermediate scales with the maximum progressively approaching the hot-spot value $\eta_{Z_{f1}}(k_0 = 0, k_x = k_{\mathrm{HS},x}, k_y = k_{\mathrm{HS},y}) = 0.78$ for momenta closer to it.
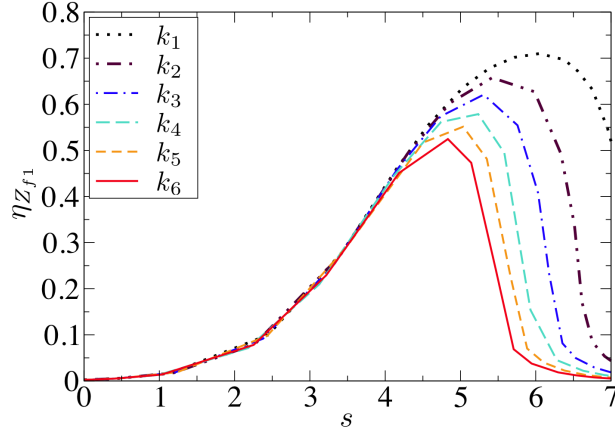
Figure 5.7: Non-Fermi liquid regimes at intermediate scales of the anomalous exponent for the quasiparticle weight $\eta_{Z_{f1}}(k_0 = 0, k_x, k_y)$ for six choices of momenta progressively approaching the hot spot (corresponding to the six data points closest to the maximum/hot spot on the right flank of Fig. 5.6). The momentum $\mathbf{k}_6$ is furthest from the hot spot and $\mathbf{k}_1$ is closest to it. The infrared is to the right of the plot $(\Lambda = \Lambda_{\mathrm{UV}}e^{-s})$.

In the numerics for Fig. 5.6, we stopped the flow at $s = 7$ (recall that $\Lambda = \Lambda_{\mathrm{UV}}e^{-s}$), leading to finite (but very large) values of Z_{f1} even at the hot spot. We used a momentum cut of 100 points producing for each grid point in Fig. 5.6 the scale-resolved flows shown in Fig. 5.7.

The Fermi velocity vanishes as well but with a smaller exponent,

$$|v_f^{\Lambda \to 0}| \sim \Lambda^{\eta_{Zf} - \eta_{Af}} = \Lambda^{z_f - 1} = \Lambda^{0.34} , \tag{5.30}$$

so that the dynamical exponent for the fermions is

$$z_f = 1 + \eta_{Z_f} - \eta_{A_f} = 1.34 . \tag{5.31}$$

An important ingredient to the scaling laws above is the self-consistently flowing boson propagator, Eqs. (5.8) and (5.11). The asymptotic static and dynamic scaling of the spin fluctuation propagator is given by

$$\lim_{\Lambda \to 0} \left[D^R(q_0, \mathbf{q}) \right]^{-1} \sim \Lambda^{\eta_{Z_b}} |q_0| + \mathbf{q}^2 \sim |q_0|^{1.66} + \mathbf{q}^2 , \tag{5.32}$$

92

with $\eta_{Z_b} = 0.66$. Remarkably, the boson dynamical exponent,

$$z_b = 2 - \eta_{Z_b} = 1.34 = z_f \ , \tag{5.33}$$

takes the same value as the fermion dynamical exponent. It is a distinguishing fea-
ture of this infrared fixed-point of electrons in metals at a SDW transition that the
dynamical exponent attains fractional value different from 1 (which is the exact value
for quantum-critical fermion systems with Lorentz-symmetry; see Janssen and Gies
(2012) and references therein) and different from 2 (which is the mean-field value of
the Hertz theory (Hertz, 1976)). Our fermion anomalous dimensions and z can be
mapped to those of Metlitski and Sachdev (2010b) for values of the Fermi velocity-
anisotropy in a range around $\alpha \approx 0.5$ and upon ignoring the marginal RG flow of α
(which is implicitly assumed in (5.25)); our boson anomalous dimension renormaliz-
ing the $\mathbf{q}^2$ term in the propagator is essentially zero, and we trace this to differences
in the RG scheme from Metlitski and Sachdev (2010b).

5.6   Conclusion

This chapter was dedicated to the critical behavior of compressible, electronic
quantum matter in two-dimensional lattices interacting with self-generated, singular
antiferromagnetic fluctuations. We generalized previous hot-spot theories to full "UV-
completed" Fermi surfaces free of spurious edge singularities in a model that can
also be analyzed with quantum Monte Carlo. This should enable a cross-fertilizing
comparison of results obtained with different methods for this problem. We provided
first quantitative estimates for the critical exponents of the single-particle and spin
fluctuations correlators which deviate strongly from the Hertz-Millis values. The
solution of our RG equations was attracted toward a stable, strong-coupling fixed
point, resulting in a common dynamic exponent for the fermions and the bosons.

It would be interesting to classify all relevant operators to our fixed point and
investigate the stability of our strong-coupling fixed point further. As a first simple
step in this direction, we have extended the truncation for the fermion dispersions to

allow for changes in the Fermi surface curvature (keeping the position of the hot spot fixed). A scale-dependent $\tilde{\alpha}^\Lambda$ that modifies the hoppings, $t_{1,x/y} \to t_{1,x/y} + \tilde{\alpha}^\Lambda$ and $t_{2,x/y} \to t_{2,x/y} - \tilde{\alpha}^\Lambda$, does the job. We found only relatively small, finite renormalizations of $\tilde{\alpha}^\Lambda$. However, a proper self-consistent investigation of a flowing Fermi surface with the full dispersion used in this paper requires an advanced truncation and likely also a self-consistent determination also of the position of the Fermi surfaces and the hot spots as a function of Λ. Potential tendencies toward magnetic ordering at incommensurate wave vectors might also be captured that way. Such a state-of-the-art truncation was recently presented for self-energy flows in the repulsive Hubbard model close to van Hove filling. (Giering and Salmhofer, 2012)

Other promising future directions are the inclusion of (d-wave) superconductivity, (Sedeki et al., 2012) an extension to the quantum-critical regime at finite temperatures, and the exploration of the antiferromagnetic phase with broken symmetry close to the quantum critical point. The latter can be achieved, for example, by generalizing Strack et al. (2008) from the superfluid $O(2)$ case to the staggered $O(3)$ case for the spin-fermion model.

Bibliography

Abanin, D. A., Parameswaran, S. A., and Sondhi, S. L., 2009. *Charge $2e$ Skyrmions in Bilayer Graphene*. Phys. Rev. Lett., 103:076802.

Abanov, A. and Chubukov, A., 2004. *Anomalous Scaling at the Quantum Critical Point in Itinerant Antiferromagnets*. Phys. Rev. Lett., 93:255702.

Abanov, A. and Chubukov, A. V., 2000. *Spin-Fermion Model near the Quantum Critical Point: One-Loop Renormalization Group Results*. Phys. Rev. Lett., 84:5608.

Abanov, A., Chubukov, A. V., and Schmalian, J., 2003. *Quantum-critical theory of the spin-fermion model and its application to cuprates: Normal state analysis*. Advances in Physics, 52(3):119.

Abanov, A. and Wiegmann, P., 2000. *Theta-terms in nonlinear sigma-models*. Nuclear Physics B, 570(3):685 .

Affleck, I. and Ludwig, A. W. W., 1991. *Universal noninteger "ground-state degeneracy" in critical quantum systems*. Phys. Rev. Lett., 67:161.

Albuquerque, A. F., Schwandt, D., Hetényi, B., et al., 2011. *Phase diagram of a frustrated quantum antiferromagnet on the honeycomb lattice: Magnetic order versus valence-bond crystal formation*. Phys. Rev. B, 84:024406.

Altshuler, B. L., Ioffe, L. B., and Millis, A. J., 1995. *Critical behavior of the $T = 0$ $2k_F$ density-wave phase transition in a two-dimensional Fermi liquid*. Phys. Rev. B, 52:5563.

Berg, E., Metlitski, M. A., and Sachdev, S., 2012. *Sign-Problem–Free Quantum Monte Carlo of the Onset of Antiferromagnetism in Metals*. Science, 338(6114):1606.

Berges, J., Tetradis, N., and Wetterich, C., 2002. *Non-perturbative renormalization flow in quantum field theory and statistical physics*. Physics Reports, 363(46):223 . Renormalization group theory in the new millennium. {IV}.

Block, M. S., Melko, R. G., and Kaul, R. K., 2013. *Fate of $\mathbb{CP}^{N-1}$ Fixed Points with q Monopoles*. Phys. Rev. Lett., 111:137202.

Bolotin, K. I., Ghahari, F., Shulman, M. D., et al., 2009. *Observation of the fractional quantum Hall effect in graphene.* Nature, 462(7270):196.

Calabrese, P., Campostrini, M., Essler, F., and Nienhuis, B., 2010. *Parity Effects in the Scaling of Block Entanglement in Gapless Spin Chains.* Phys. Rev. Lett., 104:095701.

Calabrese, P. and Cardy, J., 2004. *Entanglement entropy and quantum field theory.* Journal of Statistical Mechanics: Theory and Experiment, 2004(06):P06002.

Castro Neto, A. H., Guinea, F., Peres, N. M. R., et al., 2009. *The electronic properties of graphene.* Rev. Mod. Phys., 81:109.

Checkelsky, J. G., Li, L., and Ong, N. P., 2009. *Divergent resistance at the Dirac point in graphene: Evidence for a transition in a high magnetic field.* Phys. Rev. B, 79:115434.

Chubukov, A. V. and Morr, D. K., 1995. *Phase transition, longitudinal spin fluctuations, and scaling in a two-layer antiferromagnet.* Phys. Rev. B, 52:3521.

Chubukov, A. V., Sachdev, S., and Ye, J., 1994. *Theory of two-dimensional quantum Heisenberg antiferromagnets with a nearly critical ground state.* Phys. Rev. B, 49:11919.

Clark, B. K., Abanin, D. A., and Sondhi, S. L., 2011. *Nature of the Spin Liquid State of the Hubbard Model on a Honeycomb Lattice.* Phys. Rev. Lett., 107:087204.

Cohen-Tannoudji, C., Grynberg, G., and Dupont-Roc, J., 1992. *Atom-Photon Interactions: Basic Processes and Applications* (Wiley, New York).

Cvetkovic, V., Throckmorton, R. E., and Vafek, O., 2012. *Electronic multicriticality in bilayer graphene.* Phys. Rev. B, 86:075467.

Dhochak, K., Shimshoni, E., and Berg, E., 2015. *Spontaneous layer polarization and conducting domain walls in the quantum Hall regime of bilayer graphene.* Phys. Rev. B, 91:165107.

Doiron-Leyraud, N. and Taillefer, L., 2012. *Quantum critical point for stripe order: An organizing principle of cuprate superconductivity.* Physica C: Superconductivity, 481:161 .

Drukier, C., Bartosch, L., Isidori, A., and Kopietz, P., 2012. *Functional renormalization group approach to the Ising-nematic quantum critical point of two-dimensional metals.* Phys. Rev. B, 85:245120.

Eisenstein, J., 2014. *Exciton Condensation in Bilayer Quantum Hall Systems.* Annual Review of Condensed Matter Physics, 5(1):159.

Eisert, J., Cramer, M., and Plenio, M. B., 2010. *Colloquium : Area laws for the entanglement entropy.* Rev. Mod. Phys., 82:277.

Feldman, B. E., Krauss, B., Smet, J. H., and Yacoby, A., 2012. *Unconventional Sequence of Fractional Quantum Hall States in Suspended Graphene.* Science, 337(6099):1196.

Feldman, J. and Salmhofer, M., 2008. *Singular Fermi Surfaces II: The Two-Dimensional Case.* Reviews in Mathematical Physics, 20(03):275.

Fradkin, E. and Kivelson, S. A., 1990. *Short range resonating valence bond theories and superconductivity.* Mod. Phys. Lett. B, 04(03):225.

Freitag, F., Trbovic, J., Weiss, M., and Schönenberger, C., 2012. *Spontaneously Gapped Ground State in Suspended Bilayer Graphene.* Phys. Rev. Lett., 108:076602.

Freitag, F., Weiss, M., Maurand, R., et al., 2013. *Spin symmetry of the bilayer graphene ground state.* Phys. Rev. B, 87:161402.

Fu, L., Sachdev, S., and Xu, C., 2011. *Geometric phases and competing orders in two dimensions.* Phys. Rev. B, 83:165123.

Ganesh, R., van den Brink, J., and Nishimoto, S., 2013. *Deconfined Criticality in the Frustrated Heisenberg Honeycomb Antiferromagnet.* Phys. Rev. Lett., 110:127203.

Geim, A. K. and Grigorieva, I. V., 2013. *Van der Waals heterostructures.* Nature, 499(7459):419.

Geim, A. K. and Novoselov, K. S., 2007. *The rise of graphene.* Nature Materials, 6(3):183.

Giamarchi, T., 2004. *Quantum physics in one dimension* (Clarendon Press).

Giering, K.-U. and Salmhofer, M., 2012. *Self-energy flows in the two-dimensional repulsive Hubbard model.* Phys. Rev. B, 86:245122.

Gies, H. and Wetterich, C., 2002. *Renormalization flow of bound states.* Phys. Rev. D, 65:065001.

Gong, S.-S., Sheng, D. N., Motrunich, O. I., and Fisher, M. P. A., 2013. *Phase diagram of the spin-$\frac{1}{2}$ J_1-J_2 Heisenberg model on a honeycomb lattice.* Phys. Rev. B, 88:165138.

Grover, T. and Senthil, T., 2007. *Quantum Spin Nematics, Dimerization, and Deconfined Criticality in Quasi-1D Spin-One Magnets.* Phys. Rev. Lett., 98:247202.

Grover, T. and Senthil, T., 2008. *Topological Spin Hall States, Charged Skyrmions, and Superconductivity in Two Dimensions.* Phys. Rev. Lett., 100:156804.

Halboth, C. J. and Metzner, W., 2000. *Renormalization-group analysis of the two-dimensional Hubbard model.* Phys. Rev. B, 61:7364.

Helm, T., Kartsovnik, M. V., Sheikin, I., et al., 2010. *Magnetic Breakdown in the Electron-Doped Cuprate Superconductor* $\mathrm{Nd}_{2-x}\mathrm{Ce}_x\mathrm{CuO}_4$*: The Reconstructed Fermi Surface Survives in the Strongly Overdoped Regime.* Phys. Rev. Lett., 105:247002.

Herbut, I. F., 2007. *SO(3) symmetry between Néel and ferromagnetic order parameters for graphene in a magnetic field.* Phys. Rev. B, 76:085432.

Herbut, I. F., Lu, C.-K., and Roy, B., 2012. *Conserved charges of order-parameter textures in Dirac systems.* Phys. Rev. B, 86:075101.

Hertz, J. A., 1976. *Quantum critical phenomena.* Phys. Rev. B, 14:1165.

Hida, K., 1990. *Low Temperature Properties of the Double Layer Quantum Heisenberg Antiferromagnet -Modified Spin Wave Method-.* Journal of the Physical Society of Japan, 59(6):2230.

Honerkamp, C. and Salmhofer, M., 2001. *Temperature-flow renormalization group and the competition between superconductivity and ferromagnetism.* Phys. Rev. B, 64:184516.

Honerkamp, C. and Salmhofer, M., 2003. *Flow of the quasiparticle weight in the N -patch renormalization group scheme.* Phys. Rev. B, 67:174504.

Hou, C.-Y., Chamon, C., and Mudry, C., 2007. *Electron Fractionalization in Two-Dimensional Graphenelike Structures.* Phys. Rev. Lett., 98:186809.

Hou, C.-Y., Chamon, C., and Mudry, C., 2010. *Deconfined fractional electric charges in graphene at high magnetic fields.* Phys. Rev. B, 81:075427.

Jackiw, R. and Rossi, P., 1981. *Zero modes of the vortex-fermion system.* Nuclear Physics B, 190(4):681 .

Janssen, L. and Gies, H., 2012. *Critical behavior of the (2 + 1)-dimensional Thirring model.* Phys. Rev. D, 86:105007.

Jiang, H.-C., Wang, Z., and Balents, L., 2012. *Identifying topological order by entanglement entropy.* Nature Physics, 8(12):902.

Jung, J. and MacDonald, A. H., 2009. *Theory of the magnetic-field-induced insulator in neutral graphene sheets.* Phys. Rev. B, 80:235417.

Kharitonov, M., 2012a. *Phase diagram for the $\nu = 0$ quantum Hall state in monolayer graphene.* Phys. Rev. B, 85:155439.

Kharitonov, M., 2012b. *Canted Antiferromagnetic Phase of the $\nu=0$ Quantum Hall State in Bilayer Graphene.* Phys. Rev. Lett., 109:046803.

Kharitonov, M., 2012c. *Edge excitations of the canted antiferromagnetic phase of the $\nu = 0$ quantum Hall state in graphene: A simplified analysis.* Phys. Rev. B, 86:075450.

Kharitonov, M., 2012d. *Antiferromagnetic state in bilayer graphene.* Phys. Rev. B, 86:195435.

Kopietz, P., Bartosch, L., and Schütz, F., 2010. *Introduction to the functional renormalization group*, volume 798 (Springer).

Kotov, V. N., Uchoa, B., Pereira, V. M., et al., 2012. *Electron-Electron Interactions in Graphene: Current Status and Perspectives.* Rev. Mod. Phys., 84:1067.

Laflorencie, N., Sørensen, E. S., Chang, M.-S., and Affleck, I., 2006. *Boundary Effects in the Critical Scaling of Entanglement Entropy in 1D Systems.* Phys. Rev. Lett., 96:100603.

Landau, L. D., Lifshitz, E. M., and Pitaevskii, L. P., 1980. *Statistical Physics* (Butterworth-Heinemann).

Lang, T. C., Meng, Z. Y., Muramatsu, A., et al., 2013. *Dimerized Solids and Resonating Plaquette Order in* SU(N)-*Dirac Fermions.* Phys. Rev. Lett., 111:066401.

Lang, T. C., Meng, Z. Y., Scherer, M. M., et al., 2012. *Antiferromagnetism in the Hubbard Model on the Bernal-Stacked Honeycomb Bilayer.* Phys. Rev. Lett., 109:126402.

Lee, D.-H. and Kane, C. L., 1990. *Boson-vortex-Skyrmion duality, spin-singlet fractional quantum Hall effect, and spin-1/2 anyon superconductivity.* Phys. Rev. Lett., 64:1313.

Lee, J. and Sachdev, S., 2014. *Deconfined criticality in bilayer graphene.* Phys. Rev. B, 90:195427.

Lee, P. A. and Nagaosa, N., 1992. *Gauge theory of the normal state of high-T_c superconductors.* Phys. Rev. B, 46:5621.

Lee, S.-S., 2009. *Low-energy effective theory of Fermi surface coupled with U(1) gauge field in 2 + 1 dimensions.* Phys. Rev. B, 80:165102.

Levin, M. and Senthil, T., 2004. *Deconfined quantum criticality and Néel order via dimer disorder.* Phys. Rev. B, 70:220403.

Lu, C.-K. and Herbut, I. F., 2012. *Zero Modes and Charged Skyrmions in Graphene Bilayer.* Phys. Rev. Lett., 108:266402.

MacDonald, A. H., Girvin, S. M., and Yoshioka, D., 1988. *$\frac{t}{U}$ expansion for the Hubbard model.* Phys. Rev. B, 37:9753.

Maher, P., Dean, C. R., Young, A. F., et al., 2013. *Evidence for a spin phase transition at charge neutrality in bilayer graphene.* Nature Physics, 9(3):154.

McCann, E. and Fal'ko, V. I., 2006. *Landau-Level Degeneracy and Quantum Hall Effect in a Graphite Bilayer.* Phys. Rev. Lett., 96:086805.

Metlitski, M. A. and Sachdev, S., 2010a. *Quantum phase transitions of metals in two spatial dimensions. I. Ising-nematic order.* Phys. Rev. B, 82:075127.

Metlitski, M. A. and Sachdev, S., 2010b. *Quantum phase transitions of metals in two spatial dimensions. II. Spin density wave order.* Phys. Rev. B, 82:075128.

Metzner, W., Salmhofer, M., Honerkamp, C., et al., 2012. *Functional renormalization group approach to correlated fermion systems.* Rev. Mod. Phys., 84:299.

Millis, A. J., 1993. *Effect of a nonzero temperature on quantum critical points in itinerant fermion systems.* Phys. Rev. B, 48:7183.

Millis, A. J. and Monien, H., 1996. *Bilayer coupling in the yttrium-barium family of high-temperature superconductors.* Phys. Rev. B, 54:16172.

Moon, E.-G., 2012. *Skyrmions with quadratic band touching fermions: A way to achieve charge 4e superconductivity.* Phys. Rev. B, 85:245123.

Moon, K., Mori, H., Yang, K., et al., 1995. *Spontaneous interlayer coherence in double-layer quantum Hall systems: Charged vortices and Kosterlitz-Thouless phase transitions.* Phys. Rev. B, 51:5138.

Moriya, T., 2012. *Spin fluctuations in itinerant electron magnetism*, volume 56 (Springer Science & Business Media).

Motruk, J., Zaletel, M. P., Mong, R. S. K., and Pollmann, F., 2016. *Density matrix renormalization group on a cylinder in mixed real and momentum space.* Phys. Rev. B, 93:155139.

Nakai, Y., Iye, T., Kitagawa, S., et al., 2010. *Unconventional Superconductivity and Antiferromagnetic Quantum Critical Behavior in the Isovalent-Doped* $BaFe_2(As_{1-x}\mathbf{P}_x)_2$. Phys. Rev. Lett., 105:107003.

Nandkishore, R. and Levitov, L., 2010. *Electron interactions in bilayer graphene: Marginal Fermi liquid and zero-bias anomaly.* Phys. Rev. B, 82:115431.

Nomura, K. and MacDonald, A. H., 2006. *Quantum Hall Ferromagnetism in Graphene.* Phys. Rev. Lett., 96:256602.

Novoselov, K. S., Geim, A. K., Morozov, S. V., et al., 2004. *Electric Field Effect in Atomically Thin Carbon Films.* Science, 306(5696):666.

Novoselov, K. S., McCann, E., Morozov, S. V., et al., 2006. *Unconventional quantum Hall effect and Berry's phase of* 2π *in bilayer graphene.* Nature Physics, 2(3):177.

Obert, B., Takei, S., and Metzner, W., 2011. *Anomalous criticality near semimetal-to-superfluid quantum phase transition in a two-dimensional Dirac cone model.* Annalen der Physik, 523(8-9):621.

Overhauser, A. W., 1962. *Spin Density Waves in an Electron Gas.* Phys. Rev., 128:1437.

Paramekanti, A. and Vishwanath, A., 2004. *Extending Luttinger's theorem to* $\mathbb{Z}_2$ *fractionalized phases of matter.* Phys. Rev. B, 70(24):245118.

Patel, A. A., Chowdhury, D., Allais, A., and Sachdev, S., 2016. *Confinement transition to density wave order in metallic doped spin liquids.* Phys. Rev. B, 93:165139.

Platé, M., Mottershead, J. D., Elfimov, I. S., et al., 2005. *Fermi Surface and Quasi-particle Excitations of Overdoped* $Tl_2Ba_2CuO_{6+\delta}$. Phys. Rev. Lett., 95(7):077001.

Pujari, S., Damle, K., and Alet, F., 2013. *Néel-State to Valence-Bond-Solid Transition on the Honeycomb Lattice: Evidence for Deconfined Criticality.* Phys. Rev. Lett., 111:087203.

Punk, M., Allais, A., and Sachdev, S., 2015. *Quantum dimer model for the pseudogap metal.* Proceedings of the National Academy of Sciences, 112(31):9552.

Read, N. and Sachdev, S., 1990. *Spin-Peierls, valence-bond solid, and Néel ground states of low-dimensional quantum antiferromagnets.* Phys. Rev. B, 42:4568.

Reiss, J., Rohe, D., and Metzner, W., 2007. *Renormalized mean-field analysis of antiferromagnetism and d-wave superconductivity in the two-dimensional Hubbard model.* Phys. Rev. B, 75:075110.

Rodney, M., Song, H. F., Lee, S.-S., et al., 2013. *Scaling of entanglement entropy across Lifshitz transitions.* Physical Review B, 87(11):115132.

Rokhsar, D. S. and Kivelson, S. A., 1988. *Superconductivity and the Quantum Hard-Core Dimer Gas.* Phys. Rev. Lett., 61:2376.

Roy, B., 2013. *Classification of massive and gapless phases in bilayer graphene.* Phys. Rev. B, 88:075415.

Roy, B., 2014. *Theory of integer quantum Hall effect in insulating bilayer graphene.* Phys. Rev. B, 89:201401.

Roy, B., Kennett, M. P., and Das Sarma, S., 2014. *Chiral symmetry breaking and the quantum Hall effect in monolayer graphene.* Phys. Rev. B, 90:201409.

Sachdev, S., 1992. *Kagomé- and triangular-lattice Heisenberg antiferromagnets: Ordering from quantum fluctuations and quantum-disordered ground states with unconfined bosonic spinons.* Phys. Rev. B, 45:12377.

Sachdev, S., 2011. *Quantum phase transitions* (Cambridge University Press).

Sachdev, S. and Chowdhury, D., 2016. *The novel metallic states of the cuprates: topological Fermi liquids and strange metals.* arXiv preprint arXiv:1605.03579.

Sachdev, S., Chubukov, A. V., and Sokol, A., 1995. *Crossover and scaling in a nearly antiferromagnetic Fermi liquid in two dimensions.* Phys. Rev. B, 51:14874.

Sachdev, S. and Keimer, B., 2011. *Quantum criticality.* Physics Today, 64:29.

Salmhofer, M., Honerkamp, C., Metzner, W., and Lauscher, O., 2004. *Renormalization Group Flows into Phases with Broken Symmetry.* Progress of Theoretical Physics, 112(6):943.

Sandvik, A. W., 2007. *Evidence for Deconfined Quantum Criticality in a Two-Dimensional Heisenberg Model with Four-Spin Interactions.* Phys. Rev. Lett., 98:227202.

Sandvik, A. W., Chubukov, A. V., and Sachdev, S., 1995. *Quantum critical behavior in a two-layer antiferromagnet.* Phys. Rev. B, 51:16483.

Schollwöck, U., 2005. *The density-matrix renormalization group.* Reviews of modern physics, 77(1):259.

Schollwöck, U., 2011. *The density-matrix renormalization group in the age of matrix product states.* Annals of Physics, 326(1):96 . January 2011 Special Issue.

Schütz, F., Bartosch, L., and Kopietz, P., 2005. *Collective fields in the functional renormalization group for fermions, Ward identities, and the exact solution of the Tomonaga-Luttinger model.* Phys. Rev. B, 72:035107.

Sedeki, A., Bergeron, D., and Bourbonnais, C., 2012. *Extended quantum criticality of low-dimensional superconductors near a spin-density-wave instability.* Phys. Rev. B, 85:165129.

Senthil, T., Balents, L., Sachdev, S., et al., 2004b. *Quantum criticality beyond the Landau-Ginzburg-Wilson paradigm.* Phys. Rev. B, 70:144407.

Senthil, T. and Fisher, M. P. A., 2006. *Competing orders, nonlinear sigma models, and topological terms in quantum magnets.* Phys. Rev. B, 74:064405.

Senthil, T., Sachdev, S., and Vojta, M., 2003. *Fractionalized Fermi Liquids.* Phys. Rev. Lett., 90:216403.

Senthil, T., Vishwanath, A., Balents, L., et al., 2004a. *Deconfined Quantum Critical Points.* Science, 303(5663):1490.

Senthil, T., Vojta, M., and Sachdev, S., 2004. *Weak magnetism and non-Fermi liquids near heavy-fermion critical points.* Phys. Rev. B, 69:035111.

Sondhi, S. L., Karlhede, A., Kivelson, S. A., and Rezayi, E. H., 1993. *Skyrmions and the crossover from the integer to fractional quantum Hall effect at small Zeeman energies.* Phys. Rev. B, 47:16419.

Strack, P., Gersch, R., and Metzner, W., 2008. *Renormalization group flow for fermionic superfluids at zero temperature.* Phys. Rev. B, 78:014522.

Strack, P., Takei, S., and Metzner, W., 2010. *Anomalous scaling of fermions and order parameter fluctuations at quantum criticality.* Phys. Rev. B, 81:125103.

Taillefer, L., 2010. *Scattering and Pairing in Cuprate Superconductors.* Annual Review of Condensed Matter Physics, 1(1):51.

Takahashi, M., 1977. *Half-filled Hubbard model at low temperature.* Journal of Physics C: Solid State Physics, 10(8):1289.

Tanaka, A. and Hu, X., 2005. *Many-Body Spin Berry Phases Emerging from the π-Flux State: Competition between Antiferromagnetism and the Valence-Bond-Solid State.* Phys. Rev. Lett., 95:036402.

Velasco, J., Jr, Jing, L., Bao, W., et al., 2012. *Transport spectroscopy of symmetry-broken insulating states in bilayer graphene.* Nature Nanotechnology, 7(3):156.

Wang, L., Beach, K. S. D., and Sandvik, A. W., 2006. *High-precision finite-size scaling analysis of the quantum-critical point of S = 12 Heisenberg antiferromagnetic bilayers.* Phys. Rev. B, 73:014431.

Wegner, F., 1998. *Grassmann-Variable.* Lecture Notes (Universitt Heidelberg, Heidelberg).

Weitz, R. T., Allen, M. T., Feldman, B. E., et al., 2010. *Broken-Symmetry States in Doubly Gated Suspended Bilayer Graphene.* Science, 330(6005):812.

Wess, J. and Zumino, B., 1971. *Consequences of anomalous ward identities.* Physics Letters B, 37(1):95 .

White, S. R., 1992. *Density matrix formulation for quantum renormalization groups.* Phys. Rev. Lett., 69:2863.

White, S. R. and Huse, D. A., 1993. *Numerical renormalization-group study of low-lying eigenstates of the antiferromagnetic S= 1 Heisenberg chain.* Physical Review B, 48(6):3844.

Wilson, K. G. and Kogut, J., 1974. *The renormalization group and the ϵ expansion.* Physics Reports, 12(2):75.

Witten, E., 1983. *Global aspects of current algebra.* Nuclear Physics B, 223(2):422 .

Wu, F., Sodemann, I., Araki, Y., et al., 2014. *SO(5) symmetry in the quantum Hall effect in graphene.* Phys. Rev. B, 90:235432.

Yao, H. and Lee, D.-H., 2010. *Topological insulators and topological nonlinear σ models.* Phys. Rev. B, 82:245117.

Young, A. F., Dean, C. R., Wang, L., et al., 2012. *Spin and valley quantum Hall ferromagnetism in graphene.* Nature Physics, 8(7):550.

Young, A. F., Sanchez-Yamagishi, J. D., Hunt, B., et al., 2014. *Tunable symmetry breaking and helical edge transport in a graphene quantum spin Hall state.* Nature, 505(7484):528.

Zanchi, D. and Schulz, H. J., 2000. *Weakly correlated electrons on a square lattice: Renormalization-group theory.* Phys. Rev. B, 61:13609.

Zhang, F., Min, H., and MacDonald, A. H., 2012. *Competing ordered states in bilayer graphene.* Phys. Rev. B, 86:155128.

Zhang, L. M., Li, Z. Q., Basov, D. N., et al., 2008. *Determination of the electronic structure of bilayer graphene from infrared spectroscopy.* Phys. Rev. B, 78:235408.

Zhang, Y., Tan, Y.-W., Stormer, H. L., and Kim, P., 2005. *Experimental observation of the quantum Hall effect and Berry's phase in graphene.* Nature, 438(7065):201.

Zhu, Z., Huse, D. A., and White, S. R., 2013. *Weak Plaquette Valence Bond Order in the S=1/2 Honeycomb J_1-J_2 Heisenberg Model.* Phys. Rev. Lett., 110:127205.